

# ULTRA LOW LOSS SILICON NITRIDE PLATFORM FABRICATION AND APPLICATION

A Dissertation

Presented to the Faculty of the Graduate School

of Cornell University

in Partial Fulfillment of the Requirements for the Degree of

Doctor of Philosophy

by

Xingchen Ji

December 2018

© 2018 Xingchen Ji  
ALL RIGHTS RESERVED

# ULTRA LOW LOSS SILICON NITRIDE PLATFORM FABRICATION AND APPLICATION

Xingchen Ji, Ph.D.

Cornell University 2018

Photonics is the physical science of light (photon) generation, detection and manipulation. Silicon photonics, in particular, has gained a lot of interest in the last few decades due to its ability to control light at chip-scale. Although the field has its roots in the telecommunications industry, it has expanded to many new applications such as sensing, spectroscopy, nonlinear optics, quantum optics, opto-mechanics, and even neuroscience. Nonlinear optics has been greatly benefited from the chip-scale devices. Because light can be tightly confined inside these devices, nonlinear effects can be strongly enhanced. In recent years, there has been progress in development of microresonator-based Kerr frequency comb, these frequency combs have triggered a large number of applications, including in atomic clocks, optical communications, dual-comb spectroscopy, frequency synthesizers and sensing. However, simultaneously achieving ultra low-loss and high confinement which is critical for nonlinear optics remains a challenge.

In this dissertation, we set out to address this challenge in order to enable new applications. We choose silicon nitride as our material platform here. We begin by introducing the background of loss mechanisms, nonlinear optics and application requirements before detailing our approach to realizing a compact and scalable alternative to the existing state-of-the-art.

The first part of this dissertation investigates the current microfabrication

processes and loss origins. Detailed explanations of critical process steps including deposition, lithography and etching are discussed. We further discussed about loss measurements and methods to reduce loss. We developed processes which allows us to achieve ultra low-loss in high-confinement resonators by reducing roughness from waveguide interfaces. Moreover, we demonstrate optical parametric oscillation in an on-chip microresonator with sub-milliwatt pump powers. We extract the fundamental loss limit in our devices. Our work provides an on-chip platform for devices with performance that could be comparable to the performance achieved in discrete large devices and these processes can be also applied to other material platforms.

In the second part of this dissertation, we look into two applications of using our ultra low-loss silicon nitride platform: Optical coherence tomography (OCT) and on-chip tunable photonic delay lines. First, we present a comb with a smooth envelope and high conversion efficiency enabled by our platform. We demonstrate frequency combs for biomedical application (OCT) for the first time. To demonstrate the efficacy of our system, tissue depth scans are compared on an identical OCT system for both the novel integrated frequency comb source and a traditional superluminescent diode. Second, we demonstrate on-chip tunable photonic delay lines within a small footprint enabled by the same platform. A novel adiabatic taper design is proposed to overcome the stitching loss which limiting the achievable waveguide length. We replace the reference arm in an OCT system to illustrate the capability of the photonic delay line. We further show that the tunable photonic delay lines can extend the imaging range of the OCT for a variety of applications such as blade detection, wound detection under the gauze and structure detection of aorta. Finally, we discuss future avenues of research building on the work presented here.

## BIOGRAPHICAL SKETCH

Xingchen Ji was born in Hubei, China in 1990. Xingchen developed a passion for science. During middle school and high school, he won several regional competitions as well as national competitions in several fields including physics, chemistry and mathematics. Xingchen graduated with a B. S. in Optical Information Science and Technology from Beijing Jiaotong University in 2013 and honored with "Outstanding Graduates". As an undergraduate, he worked on quantum cascade laser, tandem polymer solar cells and other optical devices' designs and simulations in key laboratory of Luminescence and Optical Information, Beijing, China. In 2011, he was applied and chosen to be one of the exchange students to Taiwan. These experiences made him decide to continue in the field of optics for his graduate study. He attended Cornell University in 2013 to pursue his graduate study and received M.Eng degree in Electrical and Computer Engineering in 2014. Under the guidance of Prof. Michal Lipson, he became interested in integrated photonics and decided to join the group as a Ph.D. student. During his Ph.D, his research has focused on ultra low-loss microresonator fabrication and microresonator frequency combs. In 2015, Xingchen moved along with the entire Lipson Nanophotonics Group (formerly Cornell Nanophotonics Group) from Ithaca to Columbia University in the City of New York. At Columbia University, Xingchen has continued his research in integrated photonics and developing microresonator frequency combs for real-world applications.

Dedicated to my family for their trust, love and support.

## ACKNOWLEDGEMENTS

This dissertation would not be complete without expressing gratitude to my advisor, my committee members, my colleagues, my friends and family.

My deepest gratitude goes first and foremost to my advisor, Professor Michal Lipson. Her creativity and insights in science, enthusiasm for research, constant encouragement, and positive energy have deeply influenced me. She is the motivation for me to continue my graduate study as Ph.D students. She is not only a great advisor, but also an incredible role model for me. When an experiment did not work, her understanding and encouragement have inspired me to go further. I still remember the words she said to me when my wafer with weeks of hard working was destroyed due to a machine issue. It made me have the courage and confidence to keep going. Her positive energy and enthusiasm for research have motivated me. I am amazed by Michal's ability to respond emails so quickly and work at all hours, she is like a superhuman, even when she is traveling, she is always available to hold meetings in person or Skype when you need her. Michal has been pioneers and world's leader in her field for more than a decade, and there is no sign of slowing down. After moving to Columbia University, her endless energy has inspired and motivated us to work in so many new and exciting directions. It has been a great pleasure and privilege to work with her. And I thank her being such a great advisor and mentor in both professional and personal spheres.

I would like to express my heartfelt gratitude to the other committee members, Professor Alexander Gaeta and Professor Clifford Pollock. I learnt and became interested in nonlinear optics because of Alex's course. He is an amazing physicist and teacher. I thank him for the helpful discussions and inspirations. The work related to nonlinear optics wouldn't have been possible without the

guidance of him and his group. I learnt the knowledge of lasers from Clifford's course. It was one of the first classes I took at Cornell and I really enjoyed learning from his course. I enjoyed all the discussions we had and he was the other motivation for me to decide to pursue the Ph.D degree. He is inspiring and full of enthusiasm. It is my pleasure to learn from them and have both of them in my committee. I have had the privilege of collaborating with Dr. Xinwen Yao and Dr. Yu Gan from the research group of Professor Christine Hendon, and Natalie Janosik from the research group of Professor Keren Bergman at Columbia University, Dr. Aline Mayer and Dominik Waldburger from the research group of Professor Ursula Keller at ETH Zurich. Professor Reuven Ophirs discussions with us on cosmology has been very interesting.

I would like to thank the funding sources that have contributed to this work, including the National Science Foundation, the Defense Advanced Research Projects Agency (DARPA), the Air Force Office of Scientific Research (AFOSR), and the China Scholarship Council Fellowship.

I would also like to thank the members of the Gaeta Group for their close collaboration. In particular, Dr. Yoshitomo Okawachi, Dr. Alexander Klenner, Dr. Jae Jang and Chaitanya Joshi for the fruitful discussions and helpful advices for experiments.

I am very grateful to the amazing members of the Lipson Group. Thank you to Dr. Shreyas Shah, Dr. Mian Zhang, Dr. Raphael St. Gelais, Dr. Yoon Ho Daniel Lee and Dr. Austin Griffith for being my inspirations and role models. To Dr. Kevin Luke and Dr. Carl Poitras, thank you for helping me ramp up and taught me so much about fabrication. To Dr. Steven Miller and Dr. Chris Phare, thank you for insightful discussions and wish you all the best for your startup company. To Dr. Avik Dutt, you've always been helpful and given good

advices on experiments, your ideas are inspiring and exciting. To Dr. Aseema Mohanty, you've taught me so much about simulations and designs, I can always count on you for helpful suggestions. To Dr. Mohammad Amin Tadayon, your thoughts are always creative and your problem solving ability is amazing, I have always enjoyed discussions with you. Special thanks goes to Dr. Felipe Barbosa, your rigor and insight are very inspiring, and it was a pleasure learning from you. Special thanks goes to Dr. Jaime Cardenas, his valuable knowledge about fabrication and photonics have greatly impacted me, the creativity and intuition have influenced me throughout my entire graduate school. Discussions with Jaime have always been interesting and thought provoking. Special thanks also goes to Dr. Samantha Roberts, you has always been someone I can count on, I can call you anytime for discussions and advice when I am doing fabrication or making plans. Your thoughts and inputs have made the experiments more concrete. I would also like to thank all other lab mates, Brian Stern, Brian Lee, Moshe Zadka, Gaurang Bhatt, Ipshita Datta, Oscar Jimenez, Euijae Shin, Min Shin, Mateus Zanarella, Dr. You-chia Chang, Dr. Tong Lin, Dr. Ut-sav Dave. I feel really lucky to have had the privilege of working, learning and growing with you guys. I would also like to thank our administrative Krystal Paulino, she has helped me with so many urgent orders and ensured I got the parts for experiments on time.

Last but not the least, my gratitude also extends to my beloved family and friends for their loving considerations and great confidence in me all through these years. To my friends now all over the world, Garima Garg, Brandon Diggs, Wenbo Yin, Jing Ge, Chengyu Liu, Karissa Diggs, Goran Kovacevic, Nataliya Safronova, Dr. Ved Gund and Dr. Suren Jayasuriya, thank you for all the fun times and help me balance my work and life. To my parents, Chong Ji and Qin

Mei, thank you for your unconditional love, support, and encouragement. Your love is always the source of my strength. To my girlfriend, Sisi Cheng, thank you for being with me, for supporting me and always trust me whether things are good or bad. Thank you for your consistent love and care, you have made me a better person. I would like to thank everyone I have acknowledged here and many others I am falling to acknowledge properly in this manuscript, I would not have had my achievements today without the support from yours.

## TABLE OF CONTENTS

Biographical Sketch . . . . .	iii
Dedication . . . . .	iv
Acknowledgements . . . . .	v
Table of Contents . . . . .	ix
List of Tables . . . . .	xi
List of Figures . . . . .	xii
List of Publications . . . . .	1
<b>1 Introduction</b>	<b>3</b>
1.1 Integrated Photonics . . . . .	3
1.2 Nonlinear Optics . . . . .	4
1.3 Outline of the Dissertation . . . . .	5
<b>2 Basic Theory</b>	<b>8</b>
2.1 Waveguide . . . . .	8
2.2 Ring Resonator . . . . .	10
2.3 Four Wave Mixing . . . . .	13
2.4 Dispersion Engineering . . . . .	15
<b>3 Microfabrication Process</b>	<b>18</b>
3.1 Introduction . . . . .	18
3.2 Deposition . . . . .	19
3.3 Lithography . . . . .	20
3.4 Etching . . . . .	22
3.5 Cladding . . . . .	23
3.6 Chip Processing . . . . .	23
<b>4 Silicon Nitride Platform: Loss Origin, Measurement and Reduction</b>	<b>25</b>
4.1 Introduction . . . . .	25
4.2 Silicon Nitride Platform . . . . .	26
4.3 Loss Origin . . . . .	27
4.4 Loss Reduction . . . . .	29
4.4.1 Sidewall Roughness Reduction . . . . .	29
4.4.2 Top Surface Roughness Reduction . . . . .	33
4.4.3 Lithography-Induced Roughness Reduction . . . . .	39
4.5 Loss Measurement . . . . .	40
4.6 Fundamental Loss Limit Extraction . . . . .	44
4.7 Sub-Milliwatt Optical Parametric Oscillation . . . . .	50
4.8 Summary . . . . .	53

<b>5</b>	<b>Chip-Based Frequency Comb Sources For Optical Coherence Tomography</b>	<b>54</b>
5.1	Introduction . . . . .	54
5.1.1	Frequency Combs . . . . .	54
5.1.2	Optical Coherence Tomography Principle . . . . .	57
5.2	OCT Light Source Limitation . . . . .	59
5.3	Chip-Based Frequency Comb Sources . . . . .	60
5.3.1	Device Design and Comb Generation . . . . .	60
5.3.2	Experimental Setup . . . . .	63
5.3.3	OCT Images Acquisition . . . . .	65
5.4	Summary and Discussion . . . . .	71
<b>6</b>	<b>On-chip Tunable Delay Line</b>	<b>72</b>
6.1	Introduction . . . . .	72
6.2	Device Design . . . . .	72
6.3	Experimental Setup . . . . .	76
6.4	Experimental Results . . . . .	79
6.5	Summary . . . . .	83
<b>7</b>	<b>Future Work</b>	<b>84</b>
7.1	Higher Q . . . . .	84
7.2	Visible Comb and Mid-IR Combs . . . . .	85
7.3	Ultra High Resolution OCT . . . . .	85
7.4	Fully Integrated Systems . . . . .	88
	<b>Bibliography</b>	<b>90</b>

## LIST OF TABLES

1.1	Parametric oscillation threshold power for different planar non-linear platforms. . . . .	5
-----	---	---

## LIST OF FIGURES

2.1	<b>Schematic of waveguide.</b> a) Cross-section of a high index contrast waveguide core surrounded by a low index cladding material. b) Light experience total internal reflection at the core-cladding boundary when the angle of incidence exceeds the critical angle. . . . .	8
2.2	<b>Electric field distribution of optical modes calculated for a silicon nitride waveguide.</b> a) TE <sub>00</sub> mode. b) TM <sub>00</sub> mode. Note this waveguide has a height of 730 nm and width of 1500 nm, so it can support modes that polarized in both the x and y direction. . . . .	9
2.3	<b>Schematic of ring resonator and transmission.</b> a) Cross-section of a high index contrast waveguide core surrounded by a low index cladding material. b) Transmission spectrum of microring resonator, showing linewidth, resonance frequency, and free spectral range (FSR). . . . .	12
2.4	<b>Energy level diagram for four-wave mixing (FWM).</b> a) non-degenerate case. b) degenerate case. . . . .	14
2.5	<b>Representative plot of the dispersion parameter.</b> Group velocity dispersion vs. wavelength with a fixed height of 730 nm and different waveguide widths for the fundamental transverse-electric mode. Note that 2500 nm width provides us anomalous dispersion. . . . .	17
3.1	<b>Basic fabrication process flow.</b> Overview of the basic process used to create most nanophotonic structures. Each image is a schematic of the film stacks after performing the processing listed in each step. . . . .	18
4.1	<b>Mode simulation.</b> Mode simulation of 730 nm tall and 2500 nm wide waveguide showing that the mode is highly confined in the geometry we have chosen. Note that even with highly confined geometry light still interact with all surfaces of the waveguide. . . . .	28
4.2	<b>Fabricated devices.</b> a) Top view optical microscope image of a 115 $\mu\text{m}$ radius ring resonator. b) Scanning electron microscopy image of a fabricated waveguide shows smooth sidewalls using improved etching recipes. . . . .	31
4.3	<b>Schematic of waveguide (WG) and Si-Fin fabrication and measurement</b> a) Linear WG on a Si substrate 25-100 $\mu\text{m}$ long. b) Photoresist is patterned over the WG protecting the sidewalls. c) Si-Fin is etched to be 100 m tall with WG at its top. d) The Si-Fin with WG is pushed onto its side so the AFM tip can now access the WG sidewall. . . . .	32

4.4	<b>3D AFM measurement of the sidewall roughness.</b> a) Topography of waveguide sidewall using the Standard Etch, showing 3.9 nm roughness. b) Topography of waveguide sidewall using the new etch, with 2.1 nm roughness. . . . .	33
4.5	<b>Functional principle of chemical mechanical polishing.</b> The wafer that is being polished is mounted upside-down in a carrier/spindle and a slurry introduction mechanism deposits the slurry on the pad. Both the plate and the carrier are then rotated and the carrier is kept oscillating to remove the material which creates a smooth surface. . . . .	34
4.6	<b>The atomic force microscopy (AFM) scans of the top surface of Si<sub>3</sub>N<sub>4</sub> before and after the polishing step.</b> a) 3D AFM scan of the top surface of Si <sub>3</sub> N <sub>4</sub> before polishing with RMS roughness of 0.38 nm and correlation length of 29 nm. b) 3D image of the top surface of Si <sub>3</sub> N <sub>4</sub> after polishing with RMS roughness of 0.08 nm and correlation length of 8.76 nm. . . . .	35
4.7	<b>The atomic force microscopy (AFM) scans of the top surface of Si<sub>3</sub>N<sub>4</sub> before and after the polishing step.</b> a) 2D image of the top surface of Si <sub>3</sub> N <sub>4</sub> before polishing and scaled to -1.4 to 1.4 nm with RMS roughness of 0.38 nm and correlation length of 29 nm. b) 2D image of the top surface of Si <sub>3</sub> N <sub>4</sub> after polishing and scaled to -1.4 to 1.4 nm with RMS roughness of 0.08 nm and correlation length of 8.76 nm. . . . .	36
4.8	<b>The atomic force microscopy (AFM) scans of the top surface of Si<sub>3</sub>N<sub>4</sub> using a different pad.</b> a) 3D AFM scan of Si <sub>3</sub> N <sub>4</sub> top surface after CMP using a different polishing pad with RMS roughness of 0.32 nm. b) 2D image of Si <sub>3</sub> N <sub>4</sub> top surface before CMP and scaled to -1.4 to 1.4 nm with RMS roughness of 0.32 nm. . . . .	37
4.9	<b>The atomic force microscopy (AFM) scans of the top surface of Si<sub>3</sub>N<sub>4</sub> using a different slurry.</b> a) 3D image of Si <sub>3</sub> N <sub>4</sub> top surface after CMP using a different slurry with RMS roughness of 0.11 nm. b) 2D image of Si <sub>3</sub> N <sub>4</sub> top surface after CMP and scaled to -1.4 to 1.4 nm with RMS roughness of 0.11 nm. . . . .	38
4.10	<b>Schematic of multipass.</b> The same pattern is exposing multiple times at a lower current to reduce line edge roughness by averaging statistical errors. . . . .	39
4.11	<b>Normalized transmission spectrum of device using standard process.</b> Normalized transmission spectrum of ring resonators fabricated using the standard process reported in Ref. 44 with a measured full width half maximum (FWHM) of 47 MHz. . . . .	42

4.12	<b>Normalized transmission spectrum of device using only optimized etch process.</b> Normalized transmission spectrum of ring resonators fabricated using optimized etch process but without our new surface smoothing technique and multipass lithography with a measured FWHM of 12.8 MHz. . . . .	43
4.13	<b>Normalized transmission spectrum of device using both the optimized etch recipe and surface smoothing techniques.</b> Normalized transmission spectrum of ring resonators fabricated using both the optimized etch recipe and surface smoothing techniques but without multipass lithography with a measured FWHM of 7.6 MHz. . . . .	43
4.14	<b>Normalized transmission spectrum of device using all the techniques.</b> Normalized transmission spectrum of ring resonators fabricated using all the techniques including the optimized etch recipe, surface smoothing technique and multipass lithography with a measured FWHM of 5.6 MHz. . . . .	44
4.15	<b>Mode simulation for ring resonators with different interaction strength with the sidewalls.</b> a) TE Mode profile of waveguides that are 2.5 $\mu\text{m}$ and 10 $\mu\text{m}$ wide and 730 nm height. b) Same as a) but for TM. . . . .	45
4.16	<b>Normalized transmission spectra for ring resonators with different interaction strength with the sidewalls.</b> a) Measured normalized TE transmission spectra for the ring resonator composed of the 2.5 $\mu\text{m}$ wide waveguide (left) with a measured full width half maximum (FWHM) of 6.2 MHz and the measured spectra for the ring resonator composed of the 10 $\mu\text{m}$ wide waveguide (right) with a measured FWHM of 3.3 MHz in TE polarization using the optimized fabrication process. b) TM transmission spectra for the rings with narrower (left) and wider (right) waveguide with FWHM of 6.8 MHz and 5.8 MHz, respectively. . . . .	46
4.17	<b>Cavity ring-down measurement on TM mode.</b> The measured lifetime is extracted from the exponential fit to be $25.6 \pm 1.3$ ns. . . . .	47
4.18	<b>Overview of Q vs confinement factor in the past decade using <math>\text{Si}_3\text{N}_4</math> platform.</b> The red star shows that we are able to simultaneously achieve high Q and high confinement in this work. We have achieved Q of $67 \pm 7$ million with confinement factor more than 90%. . . . .	50

4.19	<b>Oscillation threshold decrease with decrease of losses.</b> a) The output power in the first generated mode as a function of the pump power. In this device, parametric oscillation occurs for a pump power of $330 \pm 70 \mu\text{W}$ (indicated by the solid green vertical line). Note that the first band appears more than one free spectral range away from the pumped resonance. b) Measured threshold power for micro-resonators with different fabrication processes as a function of the loaded quality factor ( $Q_L$ ). Threshold powers approximately follow the theoretically predicted trend of being inversely proportional to $Q_L^2$ . . . . .	52
5.1	<b>General spectrum of a frequency comb.</b> Comb lines are separated by precise spacing $f_{rep}$ and carrier envelope offset $f_{CEO}$ . . .	54
5.2	<b>Example of different frequency comb states.</b> Example of generated frequency comb spectra for different cavity resonance detunings produced by terminating the heater current scan at different values. a) the initial cascaded FWM. b) the mini-comb formation. c) chaotic-like states. d) single soliton state with a hyperbolic secant squared envelope (blue dashed curve). Details can be found in [1]. . . . .	56
5.3	<b>SD-OCT configuration.</b> The light from the source is sent into a beam splitter, then split for the two OCT interferometer arms(reference arm and sample arm). In the sample arm, the beam reflects off a fast scanning mirror and is sent to the sample for imaging. The back-scattered light is collected and sent to the OCT spectrometer for image generation. . . . .	58
5.4	<b>Artist view of a fully integrated OCT systems with frequency combs light source.</b> The frequency combs light source is formed by a reflective semiconductor optical amplifier chip fully integrated with an ultra low-loss $\text{Si}_3\text{N}_4$ microresonator (Inset). The interferometer, including beam splitter, reference arm, sampling arm and spectrometer is integrated on the same chip. A microlens and MEMS based scanning mirror can be attached to emit and collect and backscattered light from the sample. . . . .	62
5.5	<b>Device image and measured spectrum.</b> a) Microscopy image of the silicon nitride on-chip microresonator. A platinum heater is fabricated over a large portion of the cavity and allows electric contact via the pads. b) Measured frequency comb spectrum generated using the silicon nitride microresonators. Inset shows line spacing of 0.21 nm. . . . .	63

5.6	<b>Experimental setup for comb generation and pump filtering.</b> A DFB laser is amplified and coupled to the Si <sub>3</sub> N <sub>4</sub> micro-chip. On-chip heater allows thermal control of the cavity to ensure comb generation with low coherence. A grating is used to filter out the pump laser before the comb is sent to the OCT system. . . . .	64
5.7	<b>Schematic of the comb-based OCT setup.</b> The fiber coupled light source is sent into a circulator, from which the beam is first collimated in free space and then split for the two OCT interferometer arms. The reference arm includes glass prisms to control dispersion. In the sample arm the beam reflects off a fast scanning mirror and is sent to the sample for imaging. The back-scattered light is collected and sent to the OCT spectrometer for image generation. . . . .	65
5.8	<b>OCT images comparison.</b> OCT C-scans of human breast tissue taken with a) the frequency comb source, b) a single SLD source, and OCT B-scans of the same tissue taken with c) the frequency comb source (marked by the blue arrow) and d) a single SLD source (marked by the yellow arrow), respectively. Different features and tissue types, such as stromal tissue, adipose tissue and milk duct, are delineated in both B-scans. . . . .	66
5.9	<b>Measured SLD spectrum.</b> Superluminescent diode spectrum measured with optical spectrum analyzer. . . . .	67
5.10	<b>The Hematoxylin and Eosin (H&amp;E) stained histology of the human breast tissue.</b> . . . . .	67
5.11	<b>Frequency-comb-based OCT image of human coronary artery.</b> a) Stitched frequency-comb-based OCT B-scans of human coronary artery with corresponding b) H&E histology of coronary artery. Note that critical features are observed, including delineation of the fibrous cap, calcium, and layered structure of intima and media are depicted within OCT images. . . . .	68
5.12	<b>Frequency-comb-based OCT image of human aorta.</b> a) Stitched frequency-comb-based OCT B-scans of human aorta with corresponding b) H&E histology of aorta. Note that the visualization of large calcification region, the deposit of calcium. . . . .	69
5.13	<b>Interferogram and noise measurement</b> a) A typical interferogram of the comb source obtained after background subtraction and spectral shaping. b) A-line profiles of a mirror surface measured with comb source. Single A lines are shown in gray and A lines obtained by 10× averaging (corresponding to a total of 357 μs acquisition time in current setting) are shown in blue. . . . .	70

6.1	<b>Schematic of devices and simulation</b> a) Heat dissipation profile simulation for the integrated microheater. b) Schematic of on-chip photonic delay line crossing different field boundaries (shown as a dashed red line). Inset shows the mode simulation in the high confinement waveguide. One can see that the optical mode remains unaffected by the heater. . . . .	73
6.2	<b>Transmission efficiency simulation.</b> Simulation results of transmission efficiency with different taper widths, inset shows the schematic of adiabatically tapering at the field boundaries to reduce the propagation loss caused by misalignment. . . . .	74
6.3	<b>Propagation loss measurements.</b> Propagation loss of waveguides which across different fields still maintain linear fit (Note that in our case each field is 5 cm long. With a total distance of 40 cm, we cross 8 field boundaries.). It proves there is no additional loss due to misalignment in the field boundaries. . . . .	75
6.4	<b>Fabricated device with a microheater integrated on top.</b> A fabricated 0.4 m long high confinement Si <sub>3</sub> N <sub>4</sub> waveguide. These waveguides can be made tens of centimeters long with losses as low as 0.17 ± 0.01 dB/cm with an integrated platinum heater on top of the waveguide. . . . .	77
6.5	<b>Schematic of the experimental setup.</b> Schematic of the experimental setup for testing the tunable photonic delay line. C: circulator, PC: polarization controller, ODL: optical delay line, Col: collimation lens, WG: waveguide. . . . .	78
6.6	<b>OCT images comparison.</b> a) OCT B-scans of onion sample taken with fiber only without our chip. b) OCT B-scans of onion skin sample taken with our chip. . . . .	79
6.7	<b>Photonic delay line tunability test.</b> The microheater is used to tune the effective length of the reference arm of 280 μm. . . . .	80
6.8	<b>High-topology, high-SNR OCT imaging of right ventricle sample from the endocardium side.</b> Two images a) and b), taken before and after turning on the heaters. Insets show the surface area is brought up to the high SNR region from low SNR region. . . . .	81
6.9	<b>Demonstrations of 3D high-topology, high-SNR imaging.</b> a) A metal razor blade is covered by the lens tissue. Inset: A camera image of the experimental arrangement. b) A skin sample is covered by the gauze. c) A human aorta sample with high surface elevation. Note that the final 3D OCT volumes are all reconstructed from stitching two volumes taken before and after tuning the delay line. . . . .	82

7.1	<b>Measured frequency comb spectrum with broader bandwidth achieved by engineering the waveguide dispersion.</b> Measured frequency comb spectrum generated using a designed Si <sub>3</sub> N <sub>4</sub> microresonator with FWHM of 92 nm. This FWHM corresponds to a predicted axial resolution of 7.9 μm (in air) which is comparable with the achievable resolution using a single state of art SLD. . . . .	86
7.2	<b>Simulated comb spectrum with different waveguide widths.</b> a) Simulated comb spectrum generated from silicon nitride microresonators based on waveguide with a fixed height (710 nm) and varying widths between 2000 nm and 2200 nm. These simulations assume a pump laser wavelength of 1258 nm. b) Simulated ultra-broad flat spectrum generated from a microresonator based on a 2200 nm waveguide width. . . . .	87
7.3	<b>Measured frequency comb spectrum with different wavelengths achieved by engineering the waveguide dispersion.</b> Measured frequency comb spectrum generated using same Si <sub>3</sub> N <sub>4</sub> platform centered around 1600 nm with FWHM of 154 nm (corresponding to resolution of 7.3 μm in air). . . . .	88

## List of Publications

1. X. Ji, F. A. S. Barbosa, S. P. Roberts, A. Dutt, J. Cardenas, Y. Okawachi, A. Bryant, A. L. Gaeta, and M. Lipson, "Ultra-low-loss on-chip resonators with sub-milliwatt parametric oscillation threshold," **Optica** 4, 619-624 (2017).
2. X. Ji, A. Klenner, X. Yao, Y. Gan, A. L. Gaeta, C. P. Hendon, and M. Lipson, "Chip-based frequency combs sources for optical coherence tomography," **submitted**.
3. X. Ji, X. Yao, Y. Gan, A. Mohanty, M. Tadayon, C. P. Hendon, and M. Lipson, "On-chip tunable photonic delay line," **submitted**.
4. B. Stern, X. Ji, Y. Okawachi, A. L. Gaeta, and M. Lipson, "Battery-operated integrated frequency comb generator," **Nature**, (2018).
5. J. K. Jang, A. klenner, X. Ji, Y. Okawachi, M. Lipson, and A. L. Gaeta, "Synchronization of coupled optical microresonators," **Nature Photonics**, (2018).
6. A. Dutt, C. Joshi, X. Ji, J. Cardenas, Y. Okawachi, K. Luke, A. L. Gaeta, and M. Lipson, "On-chip dual-comb source for spectroscopy," **Science Advances** 4 (3), e1701858 (2018).
7. M. Yu, Y. Okawachi, C. Joshi, X. Ji, M. Lipson, and A. L. Gaeta, "Gas-Phase Microresonator-Based Comb Spectroscopy without an External Pump Laser," **ACS Photonics** 5 (7), 27802785 (2018).
8. C. Joshi, A. Klenner, Y. Okawachi, M. Yu, K. Luke, X. Ji, M. Lipson, A. L. Gaeta, "Counter-rotating cavity solitons in a silicon nitride microresonator," **Optics Letters** 43 (3), 547-550 (2018).

9. Y. Okawachi, M. Yu, J. Cardenas, X. Ji, A. Klenner, M. Lipson, and A. L. Gaeta, "Carrier envelope offset detection via simultaneous supercontinuum and second-harmonic generation in a silicon nitride waveguide," **Optics Letters** 43, 46274630 (2018).
10. B. Stern, X. Ji, A. Dutt, M. Lipson, "Compact narrow-linewidth integrated laser based on a low-loss silicon nitride ring resonator," **Optics Letters** 42 (21), 4541-4544 (2017).
11. S. A. Miller, M. Yu, X. Ji, A. G. Griffith, J. Cardenas, A. L. Gaeta, and M. Lipson, "Low-loss silicon platform for broadband mid-infrared photonics," **Optica** 4, 707-712 (2017).
12. M. Yu, J.K. Jang, Y. Okawachi, A.G. Griffith, K. Luke, S.A. Miller, X. Ji, M. Lipson, and A. L. Gaeta, "Breather soliton dynamics in microresonators," **Nature Communications** 8, 14569 (2017).
13. Y. Okawachi, M. Yu, J. Cardenas, X. Ji, M. Lipson, A. L. Gaeta, "Coherent, directional supercontinuum generation," **Optics Letters** 42 (21), 4466-4469 (2017).
14. J. K. Jang, Y. Okawachi, M. Yu, K. Luke, X. Ji, M. Lipson, and A. L. Gaeta, "Dynamics of mode-coupling-induced microresonator frequency combs in normal dispersion," **Optics Express** 24, 28794-28803 (2016).
15. C. Joshi, J. K. Jang, K. Luke, X. Ji, S. A. Miller, A. Klenner, Y. Okawachi, M. Lipson, and A. L. Gaeta, "Thermally controlled comb generation and soliton modelocking in microresonators," **Optics Letters** 41, 2565-2568 (2016).

# CHAPTER 1

## INTRODUCTION

### 1.1 Integrated Photonics

We have seen a tremendous growth in the field of integrated photonics in the past decade. Photonics uses light rather than electrons to perform a wide variety of applications such as sensing, communication, and data processing. Photonics technology includes sources of light such as lasers, waveguides to guide light such as fiber optics, and a variety of opto-electronic devices, such as optical modulators and receivers. Silicon photonics, in particular, is gaining significant attention. It allows massive fabrication of optical devices at low cost by utilizing standard fabrication techniques and CMOS (complementary metal-oxide semiconductor) compatible materials. As a result, silicon photonics is now widely accepted as a key technology in next-generation communications systems and data interconnects.

In the past decade, advancements in silicon photonics for communications and data interconnects have led to an expansion into a plethora of fields, including chemical sensing, biomedical imaging, astronomy, spectroscopy, LIDAR, optical ranging, nonlinear optics, quantum optics, opto-mechanics and optogenetics. Silicon photonics have shown great potential to serve as a set of key building blocks for these applications. The field has progressed beyond laboratory towards real industry applications. In telecom and data industries, it took nearly a decade or more before photonics products were ready or near-ready. So we are now at a time in which integrated photonics in other application fields will continue to mature and hopefully in the near future we can see photon-

ics technologies being applied in our daily lives such as medical clinics, health monitoring, quantum computing, self-driving cars, augmented reality devices, and wearable smart devices.

## 1.2 Nonlinear Optics

Nonlinear optics is the study of nonlinear phenomena that modifies optical properties of a material system with the presence of light. Typically, the optical properties modification only happens when the light is sufficiently intense and the response of a material system is in a nonlinear manner. The beginning of the field of nonlinear optics is often taken to be the discovery of second-harmonic generation by Franken et al [2], shortly after the demonstration of the first working laser by Mianman in 1960 [3]. Nonlinear interactions depend on the intensity. The effects become stronger at high intensities, which corresponds to either high powers or very tightly confined geometries. Interaction length is another important factor in determining the strength of nonlinear effects. In traditional cases, there is a trade-off between achievable intensity and interaction length, this is due to the diffraction limit of the focused beam. By using an optical waveguide, we can increase the interaction length beyond the diffraction limit. These waveguides can confine light to the micrometer scale, leading to high intensities. In the past decade, many materials have been proposed as nonlinear platforms for a variety of applications. We have shown the most widely used integrated platforms in Table 1.1. Here we focus on the nonlinear effect around telecom wavelength (1550 nm). However, silicon suffers from two-photon absorption near this wavelength, which induces optical loss. As a result, we do not include silicon in the table. In this dissertation, we will focus on using sili-

con nitride as our platform. This is because of improved fabrication techniques allow us to achieve ultra low-loss and consequently propagate light for long distances in silicon nitride platform. And the combination of high intensities with long propagation lengths enables efficient nonlinear optics studies in this platform. We are able to observe nonlinear processes with record-low power. The main nonlinear process we will discuss in this dissertation is microresonator optical frequency combs. This research area has enabled a way of generating new frequencies using a relatively low power continuous wave laser source and a silicon nitride micro-chip. Frequency combs have great potential for applications in metrology, optical clocks, spectroscopy, sensing, astronomical calibration, as well as telecommunications.

Platform	$n$	$\chi^3$ ( $\text{m}^2/\text{V}^2$ )	$n$ ( $\text{m}^2/\text{W}$ )	$dn/dT$ ( $\text{K}^{-1}$ )	Q	P (mW)
Hydex	1.7	$1.2 \times 10^{-21}$	$1.2 \times 10^{-19}$	-	$1 \times 10^6$	50
AlN	2.1	$3.3 \times 10^{-21}$	$2.3 \times 10^{-19}$	$2.32 \times 10^{-5}$	$8 \times 10^5$	200
Diamond	2.4	$3.3 \times 10^{-21}$	$8.2 \times 10^{-20}$	$7.68 \times 10^{-6}$	$1 \times 10^6$	20
$\text{Al}_{0.17}\text{Ga}_{0.83}\text{As}$	3.3	$1.0 \times 10^{-18}$	$2.6 \times 10^{-17}$	-	$1 \times 10^5$	3
SiC	2.0	$1.4 \times 10^{-20}$	$2.5 \times 10^{-19}$	$9 \times 10^{-3}$	$1.7 \times 10^7$	-
$\text{Si}_3\text{N}_4$	2.0	$3.4 \times 10^{-21}$	$2.5 \times 10^{-19}$	$2.45 \times 10^{-5}$	$3.6 \times 10^7$	$0.33 \pm 0.07$

Table 1.1: Parametric oscillation threshold power for different planar nonlinear platforms.

### 1.3 Outline of the Dissertation

Chapter 2 briefly introduce the basic theory related with our study of integrated photonics and nonlinear optics. We start with a basic introduction to waveguides, ring resonators, four-wave mixing and dispersion engineering.

Chapter 3 explains the microfabrication processes in details. We start with

a overview of the process applicable to fabrication of most photonic devices. A more detailed explanation of critical process steps including deposition, lithography and etching are presented. These critical steps are directly relevant with the major processing improvements discussed in the following chapter. In addition, cladding and chip processing steps are also discussed in this chapter.

In Chapter 4, we focus on the loss. We talked about the advantages of using  $\text{Si}_3\text{N}_4$  as our material platform. We further discuss about the loss origin, loss measurement and loss reduction. We directly measure sidewall roughness We developed processes which allows us to achieve ultra low-loss in high-confinement resonators. Moreover, we demonstrate sub-milliwatt threshold for nonlinear process and extract the absorption-limited Q of the ring resonator to be at least 170 million. Finally, we have identified scattering loss is the main source of propagation loss which prevents achieving high Q.

In Chapter 5, we demonstrate frequency combs used in biomedical applications (OCT) for the first time. We present a comb with a smooth envelope and high conversion efficiency which is ideal for OCT. To demonstrate the efficacy of our system, tissue depth scans are compared on an identical OCT system for both the novel integrated frequency comb source and a traditional superluminescent diode. Finally, the potential of platform is further discussed.

In Chapter 6, we demonstrate on-chip tunable photonic delay lines within a small footprint using ultra low-loss high confinement waveguides with integrated microheater. A novel adiabatic taper design is proposed to overcome the stitching loss which limiting the achievable waveguide length. In order to illustrate the capability of the photonic delay line, we replace the reference arm in an OCT system with the tunable photonic delay line. We further demonstrate

its ability to compensate the path length difference in the measurement system. Finally, we show that the tunable photonic delay lines can extend the imaging range of the OCT for a variety of applications such as blade detection, wound detection under the gauze and structure detection of aorta.

Chapter 7 concludes with a discussion of the many possible research avenues one could take to build upon work presented in this dissertation.

CHAPTER 2  
BASIC THEORY

## 2.1 Waveguide

Waveguide is one of the basic components in photonics. As in Figure 2.1a, a high refractive index core material is surrounded by a low refractive index cladding material. Similar to optical fiber, when light travels from a high index medium to a low index medium at an angle ( $\theta$ ) is greater than the critical angle ( $\theta_{cr} = \arcsin(n_{cladding}/n_{core})$ ), light is entirely reflected and propagated inside the structure (Figure 2.1b). Total internal reflection is the basic principle and these structures are used as waveguide in photonics field.

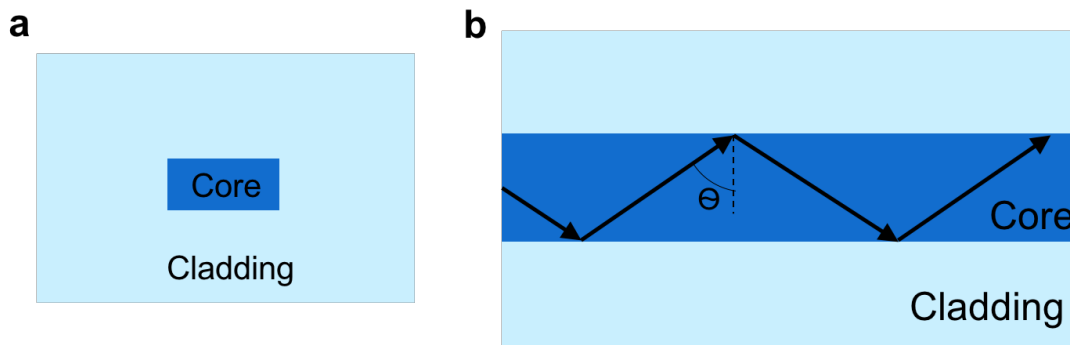


Figure 2.1: **Schematic of waveguide.** a) Cross-section of a high index contrast waveguide core surrounded by a low index cladding material. b) Light experience total internal reflection at the core-cladding boundary when the angle of incidence exceeds the critical angle.

Waveguide supports a finite number of modes. These modes are certain spatial eigensolutions of the Maxwell's equations with boundary conditions set by the waveguide properties. The spatial distributions of the electromagnetic

field,  $E(x, y)$  are used to represent these eigenmodes. From Maxwell's equations we know that electric field and magnetic field can be derived from each other. So typically the electric field is solved to find the optical mode. There are analytical methods to approximate the optical modes. Here, we used a finite element solver (FEM) performed by COMSOL Multiphysics to calculate the optical modes in our waveguides. By using FEM solvers, realistic waveguide shapes with a more complex refractive index distribution can be calculated. As an example, we choose our waveguide with height of 730 nm, width of 1500 nm and wavelength at 1550 nm. This waveguide can support modes that polarized in both the  $x$  and  $y$  direction. Modes mainly polarized in the  $x$ -direction are called TE modes and modes mainly polarized in the  $y$ -direction are called TM modes. Figure 2.2 shows an example of the calculated electric field distribution of both TE and TM modes. The effective refractive index ( $n_{neff}$ ) of each mode can be calculated using the FEM solver.

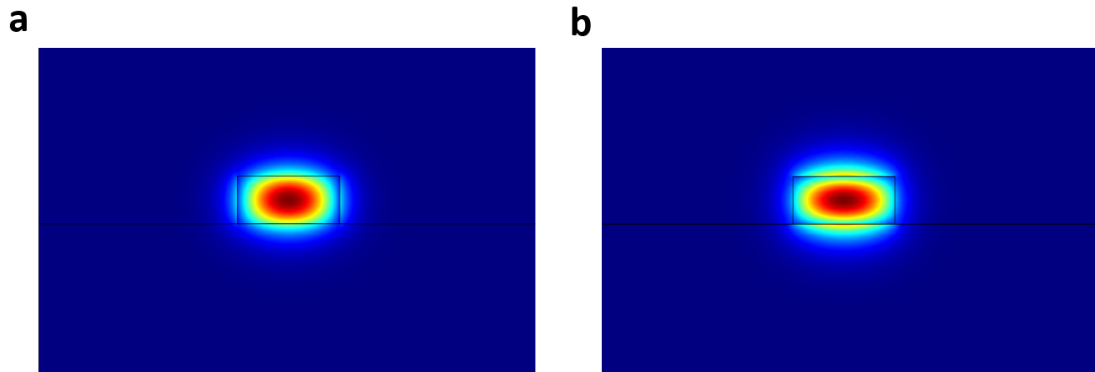


Figure 2.2: **Electric field distribution of optical modes calculated for a silicon nitride waveguide.** a)  $TE_{00}$  mode. b)  $TM_{00}$  mode. Note this waveguide has a height of 730 nm and width of 1500 nm, so it can support modes that polarized in both the  $x$  and  $y$  direction.

Unlike optical fibers, waveguides used in photonics field normally have high

index contrast. This allows light to be more confined inside the waveguide which means the size of the waveguide can be dramatically decreased while still maintaining light confinement. The confinement factor can be written as [4]:

$$\Gamma = \frac{n_g \iint_A \varepsilon |\mathbf{E}|^2 dx dy}{n_A \iint_{\infty} \varepsilon |\mathbf{E}|^2 dx dy} \quad (2.1)$$

The effective mode area,  $A_{eff}$ , can be also used to describe the degree of confinement:

$$A_{eff} = \frac{(\iint_{-\infty}^{+\infty} |\mathbf{E}|^2 dx dy)^2}{\iint_{-\infty}^{+\infty} |\mathbf{E}|^4 dx dy} \quad (2.2)$$

Compared with optical fibers, small waveguide size and high confinement allow for higher light intensity in the waveguide which is important for nonlinear applications. Besides, high index contrast waveguide can exhibit a strong change in refractive index across different wavelengths which enabling dispersion engineering by changing the waveguide geometry which will be discussed in section 2.4.

## 2.2 Ring Resonator

Ring resonator is a fundamental component widely used in integrated photonics. A ring resonator consists of a closed loop cavity formed by a waveguide wrapped around itself and a bus waveguide coupled to it (Figure 2.3a). Light circulates inside the closed loop cavity multiple times. Each single pass through the cavity is called a roundtrip. The bus waveguide is positioned close enough to the ring resonator such that light can couple into and out of the cavity using evanescent field. Constructive interference occurs when the phase of the light accumulated in one roundtrip around the length of the cavity is an integral mul-

multiple of  $2\pi$ , mathematically, it can be written as:

$$\beta \times L = 2\pi m \quad (2.3)$$

where  $m$  is an integer,  $L$  is the length of the cavity,  $\beta$  is the propagation constant, and  $\beta = kn_{eff} = 2\pi n_{eff} / \lambda$ ,  $n_{eff}$  is the effective index,  $\lambda$  is the wavelength. When the cavity is "on resonance", the input light from the bus waveguide destructively interferes with the resonant light leaking through the coupling region out of the cavity. As a result, the light transmitted through the bus waveguide shows a dip. A typical transmission spectrum with a dip is shown in Figure 2.3b, it forms a characteristic Lorentzian function in the frequency/wavelength domain.  $\omega_0$  is the resonance frequency and  $\Delta\omega$  is the full-width at half maximum (FWHM) resonance linewidth.

The spacing between adjacent resonance frequencies belonging to longitudinal modes can be derived from this expression to be,

$$FSR = \frac{c}{n_g(\lambda)L} = \frac{2\pi c}{n_g L} \quad (2.4)$$

and is called the free-spectral range (FSR) of the resonator.  $n_g$  is the group index,  $n_g = n_{eff} - \lambda dn_{eff} / d\lambda$ . The group index is related to the first order dispersion which we will discuss later in section 2.4. The width of the Lorentzian lineshape ( $\Delta\omega$ ) is inversely proportional to the cavity lifetime ( $\tau$ ) which indicates the cavity decay rate. A resonator's quality factor ( $Q$ ) is defined as the ratio of the energy stored in it to the energy lost per cycle, it indicates how much energy is stored in the resonator which is given by:

$$Q = \frac{\omega_0}{\Delta\omega} = \omega\tau \quad (2.5)$$

The cavity  $Q$  is directly proportional to the cavity lifetime. The quality factor defined above and measured in experiments is called the loaded  $Q$  ( $Q_L$ ). It includes

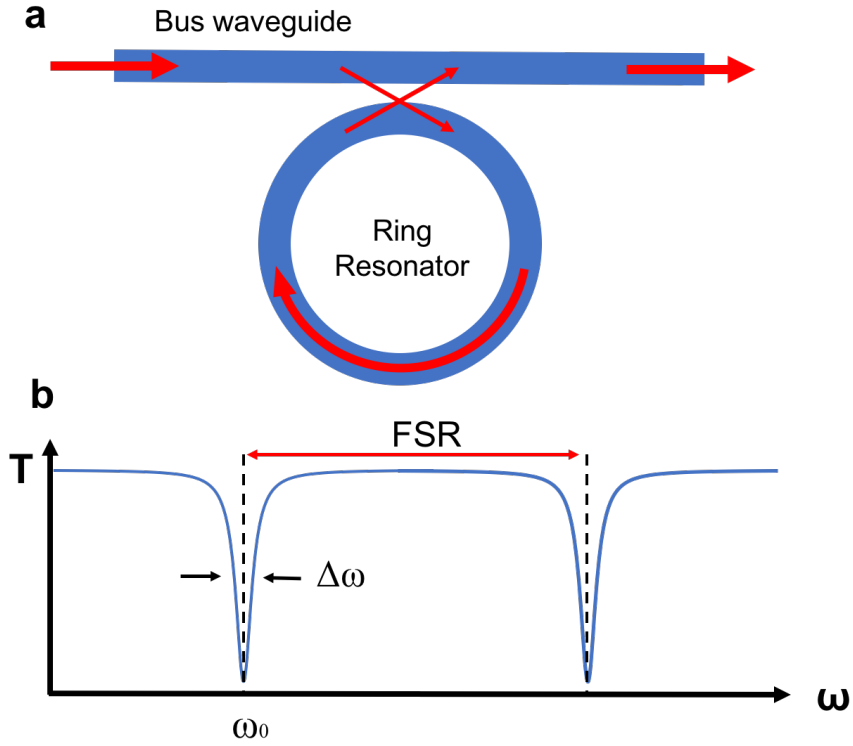


Figure 2.3: **Schematic of ring resonator and transmission.** a) Cross-section of a high index contrast waveguide core surrounded by a low index cladding material. b) Transmission spectrum of microring resonator, showing linewidth, resonance frequency, and free spectral range (FSR).

all loss mechanisms and is determined by the measured FWHM linewidth.  $Q_i$  is the intrinsic quality factor of the cavity which is directly related to propagation losses. The relation of  $Q_i$  and  $Q_L$  can be written as [5,6],

$$\frac{1}{Q_L} = \frac{1}{Q_i} = \frac{1}{Q_c} \quad (2.6)$$

$Q_i$  is the intrinsic quality factor which can be extracted from the load quality factor  $Q_L$  and the coupled quality factor  $Q_c$ .  $Q_c$  is related with coupling condition between the resonator and the bus waveguide. If the coupling loss is higher than the intrinsic losses, the resonator is said to be overcoupled, and the on-resonance normalized transmission minimum ( $T_{min}$ ) is between 0 and 1,  $Q_c$

can be calculated by,

$$Q_c = \frac{2Q_L}{1 + \sqrt{T_{min}}} \quad (2.7)$$

If the coupling loss is lower than the intrinsic losses, the resonator is said to be undercoupled, and the on-resonance normalized transmission minimum ( $T_{min}$ ) is between 0 and 1,  $Q_c$  can be calculated by,

$$Q_c = \frac{2Q_L}{1 - \sqrt{T_{min}}} \quad (2.8)$$

If the coupling loss is exactly the same as the intrinsic losses, the resonator is said to be critical coupling, and we can get a perfect extinction of the transmitted light on resonance ( $T_{min}=0$ ), then

$$Q_c = 2Q_L \quad (2.9)$$

Finesse ( $F$ ) is another important figure-of-merit, measuring the number of round trips light takes inside the cavity, and is given by the ratio of the FSR to the linewidth:

$$F = \frac{FSR}{\Delta\omega} \quad (2.10)$$

## 2.3 Four Wave Mixing

Four-wave mixing (FWM) is a third-order parametric nonlinear process, whereby light interactions between two or three frequencies (or wavelengths) produce one or two new wavelengths. It relies on the third-order nonlinearity. Unlike second-order nonlinearity which is found only in noncentrosymmetric crystals, third-order nonlinearity is ubiquitous. It is found in all materials, even vacuum is nonlinear above Schwinger limit ( $E > 10^{18}$  V/m). FWM is a phase-sensitive process, in that the efficiency of the process is strongly affected by

phase matching conditions. So in order to have an efficient FWM, there are two fundamental requirements: 1. The light fields should have a high intensity, this is due to weak optical nonlinearities in dielectric materials. 2. The fields should be phase-matched (momentum conservation). There are several common forms of FWM, but here we will focus on FWM involving two pump photons ( $\omega_1, \omega_2$ ), a signal photon ( $\omega_3$ ), and a fourth generated photon ( $\omega_4$ ) commonly known as the idler photon. These optical fields satisfy energy conservation ( $\omega_4 = \omega_1 + \omega_2 - \omega_3$ ) and momentum conservation ( $k_4 = k_1 + k_2 - k_3$ ). If two of the wavelengths are identical, the process is termed as degenerate FWM (Figure 2.4).

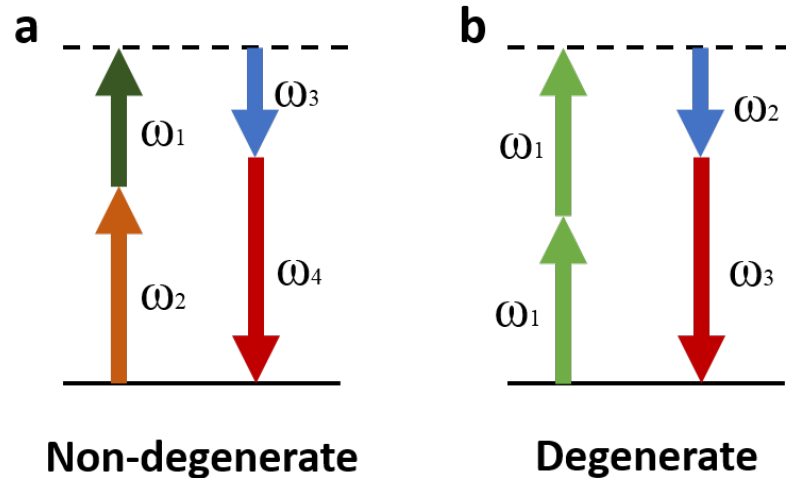


Figure 2.4: **Energy level diagram for four-wave mixing (FWM).** a) non-degenerate case. b) degenerate case.

Typically, a weak signal beam ( $\omega_2$ ) will interact with one or two strong pump beams ( $\omega_1$ ) to produce light at the idler wavelength ( $\omega_3$ ). In this case, the signal and idler frequencies are symmetric with respect to the pump. In addition to generation of an idler photon, the signal and idler photons experience nonlinear, or parametric, gain as a result of energy transferred from the two pump photons. Another common FWM process is third-harmonic generation,

in which three photons mix to produce a photon at triple their frequency:  $\omega_4 = \omega_1 + \omega_2 + \omega_3$ . In particular, we will focus on the case of degenerate FWM in our dissertation.

## 2.4 Dispersion Engineering

Dispersion is one of the most important properties that controls the physical behavior of waveguides in both the linear and nonlinear regimes. Its design is key to achieving high performance in applications such as parametric amplification [7], wavelength conversion [8], and supercontinuum generation [9]. Light traveling through a waveguide is affected not only by the material dispersion of the core and cladding media, but also displays a high sensitivity to changes in the waveguide geometry. This is because light at different wavelengths experiences a different effective waveguide mode index. Most materials are dispersive, such that the refractive index changes across wavelength. And the waveguide dispersion is a result of interplay among many factors which determine the waveguide geometry, for instance, waveguide width, waveguide height, refractive index contrast, sidewall angle and bending radius.

The total dispersion of a waveguide is a combination of both material and waveguide dispersion characteristics. Waveguide dispersion can dominate the overall dispersion characteristics and can be used as a powerful tool to engineer the dispersion. By designing the waveguide geometry, it is possible to engineer the resulting dispersion of the waveguide to match particular applications. When engineer the dispersion, different propagation effects are affected by different orders of dispersion. In most cases, the first two orders of dispersion,  $\beta_1$

and  $\beta_2$ , are of importance.  $\beta_1$  is related to the group velocity ( $v_g$ ) and the group index ( $n_g$ ) by:

$$\beta_1 = \frac{1}{v_g} = \frac{n_g}{c} = \frac{1}{c} \left( n + \omega \frac{dn}{d\omega} \right) \quad (2.11)$$

$\beta_2$  is called group velocity dispersion (GVD) and used most often to determine how the medium will affect the duration of an optical pulse traveling through it. From the GVD, the dispersion parameter,  $D$ , can be calculated:

$$\beta_2 = \frac{1}{c} \left( 2 \frac{dn}{d\omega} + \omega \frac{d^2n}{d\omega^2} \right) \quad (2.12)$$

$$D = \frac{d\beta_1}{d\lambda} = -\frac{2\pi c}{\lambda^2} \beta_2 = -\frac{\lambda}{c} \frac{d^2n}{d\lambda^2} \quad (2.13)$$

When  $\beta_2 > 0$  ( $D < 0$ ), the dispersion is called normal GVD, because most materials exhibit  $\beta_2 > 0$  over most of their transparency range. If  $\beta_2 < 0$  ( $D > 0$ ), the dispersion is called anomalous GVD. The wavelengths where  $\beta_2$  is zero and the light does not experiences any second-order dispersion are called zero dispersion wavelengths. The requirement for anomalous GVD is among the most important requirements for efficient FWM gain and parametric oscillation, and serves as a guiding principle when designing the dimensions of the waveguides.

A representative plot of the dispersion parameter with different waveguide geometry is shown in Figure 2.5. The Sellmeier equation we used to calculate material dispersion effects is:

$$n_{Si_3N_4}^2 = 1 + \frac{3.0249\lambda^2}{\lambda^2 - 135.3406^2} + \frac{40341\lambda^2}{\lambda^2 - 1239842^2} \quad (2.14)$$

We see that the dispersion can be anomalous, despite the fact that the bulk dispersion of  $Si_3N_4$  is strongly normal at these wavelengths. High index contrast in provides strong light confinement and enables a high degree of control

for dispersion engineering. Dispersion control of high index contrast waveguides has led to significant developments in integrated nonlinear optics, including Kerr frequency comb generation.

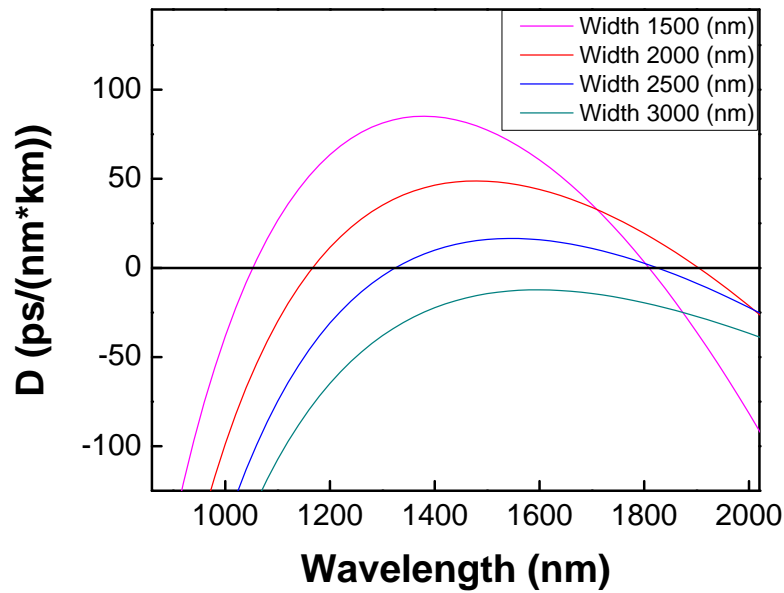


Figure 2.5: **Representative plot of the dispersion parameter.** Group velocity dispersion vs. wavelength with a fixed height of 730 nm and different waveguide widths for the fundamental transverse-electric mode. Note that 2500 nm width provides us anomalous dispersion.

CHAPTER 3  
MICROFABRICATION PROCESS

### 3.1 Introduction

Microfabrication is a collection of technologies which are utilized in making microdevices. Integrated circuits, microresonators, microfluidics, microsensors, solar cells and countless others rely on microfabrication. Microfabrication is one of the key factors which determines the device performance. In this chapter we discuss about basic fabrication process and present an overview of device fabrication to help understanding the overall process (The basic flow is shown in Figure 3.1). Variations of the basic fabrication process have been widely used in both electronics and photonics fields.

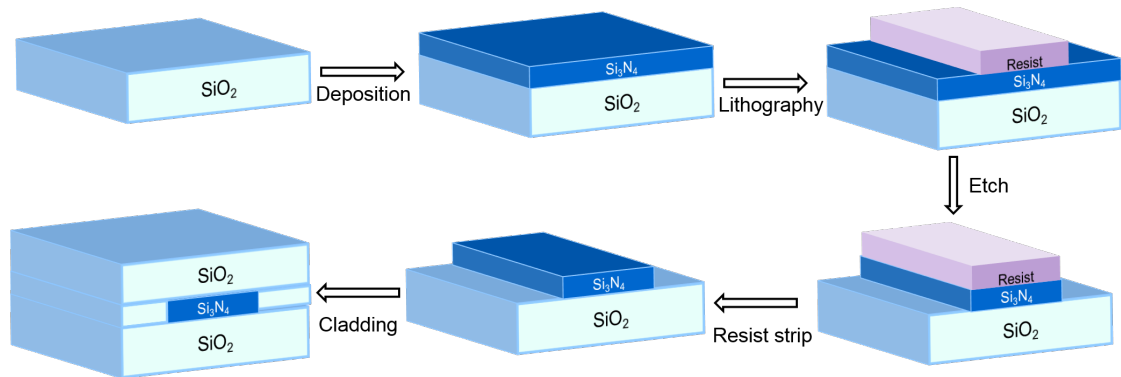


Figure 3.1: **Basic fabrication process flow.** Overview of the basic process used to create most nanophotonic structures. Each image is a schematic of the film stacks after performing the processing listed in each step.

## 3.2 Deposition

The fabrication process normally start with the handle wafer. The most commonly used handle wafers are silicon. Our optical devices are fabricated on silicon wafers with 4 inch diameter. This is because of compatibility with other equipments in the clean room facility. However, wafers with other materials such as fused silica and wafers with other sizes are also available.

Films are then created on the handle wafers. Depending on the material properties and applications, different core layers and bottom cladding layers are chosen. In our case, we choose  $\text{Si}_3\text{N}_4$  as our core layer and  $\text{SiO}_2$  as our bottom cladding material. Start with 4 inch silicon wafers, we grow a thermal oxide layer using a combination of dry and wet oxidation process at  $1200^\circ\text{C}$ . Dry oxidation is done with  $\text{O}_2$  only to provide a smooth interface between  $\text{SiO}_2$  bottom cladding layer and the core layer. Then wet oxidation is done using  $\text{H}_2\text{O}$  to provide a faster growth rate (As an example, dry oxidation of  $4\ \mu\text{m}$  oxide at  $1200^\circ\text{C}$  will take about 342 hours and wet oxidation of  $4\ \mu\text{m}$  oxide at  $1200^\circ\text{C}$  will take about 20 hours). The combination of dry and wet oxidation provides  $\text{SiO}_2$  bottom cladding layer with  $4\text{-}5\ \mu\text{m}$  thickness in a reasonable time and the thickness is sufficient to optically isolate the waveguide from the silicon beneath.

Low pressure chemical vapor deposition (LPCVD) and plasma-enhanced chemical vapor deposition (PECVD) are the common ways to deposit materials. In chemical vapor deposition (CVD), the process depends on both chemical reactions and flow dynamics. The source materials are brought into the chamber in the gas phase, they diffuse to the wafer surface and then react there to

deposit films. Byproducts are created during the process, and pumped away by the gas flow. In LPCVD process, pressure, temperature, flow rate and gas ratio are the main variables. In PECVD process, in addition to all the main variables, RF power can also be varied. LPCVD is normally done at high temperatures (for example 800°C), and PECVD is done at much lower temperatures, typically around 300 or 400°C. Lower temperatures enabling deposition on most materials. However, lower temperatures result in less dense films. For our process, we choose to use LPCVD to form our Si<sub>3</sub>N<sub>4</sub> core layer. This is because LPCVD gives better quality film with lower optical loss compared with PECVD. However, cracking in Si<sub>3</sub>N<sub>4</sub> film with thickness more than 400 nm still remains a problem. In order to avoid film cracking, we have adopted two different methods. On one hand, we define trenches in the wafer prior to Si<sub>3</sub>N<sub>4</sub> deposition to prevent cracks propagating from the edge to the interior of the wafer. On the other hand, in order to achieve final desired film thickness (typically around 730 nm) without cracking, we deposit our Si<sub>3</sub>N<sub>4</sub> films in two steps [10]. We start the deposition with 350 nm of Si<sub>3</sub>N<sub>4</sub> using LPCVD at 800 °C. This process uses ammonia, NH<sub>3</sub>, and dichlorosilane (DCS), SiH<sub>2</sub>Cl<sub>2</sub> as reacting gases to form Si<sub>3</sub>N<sub>4</sub>, H<sub>2</sub>, and HCl. We anneal the films at 1200°C in argon atmosphere to increase the optical quality of the film by driving out defects. After annealing, another Si<sub>3</sub>N<sub>4</sub> deposition is repeated using the same deposition process to achieve the final desired film thickness.

### 3.3 Lithography

Lithography is a process used in microfabrication to transfer a designed pattern to a chemical "resist" layer. Photolithography and electron beam lithography

(E-beam or EBL) are the two main lithography methods used in microfabrication. Photolithography requires a photomask which contains the designed pattern, it uses light to transfer the pattern from the photomask to the resist. E-beam is a maskless process, it scans a focused beam of electrons to directly draw the designed pattern on the resist. The advantage of using photolithography is the fast pattern transferring speed and the ability to massive production at low cost. However, as drawbacks, it sacrifices the achievable minimum feature size and the flexibility of changing patterns due to the mask limitation. E-beam offers a great flexibility of customizing patterns with resolution down to sub-10 nm because of the direct-write capabilities. However, the writing time for E-beam heavily depends on the pattern and writing condition (such as dose and current) which can lead to high cost and low throughput. These properties limit the usage of E-beam to photomask fabrication, low-volume semiconductor devices production, and research. For the research purposes pursued in this dissertation, we choose to use E-beam in our fabrication.

We use the JEOL JBX-9500 Electron Beam Lithography System which uses accelerating voltage of 100 kV. The beam current can be adjusted to a maximum of 100 nA. Larger currents lead to bigger spot size for the tool and worse resolution. The dose delivered to the resist depends on the resist type and is defined in terms of  $\mu\text{C}$ . The dose and current will determine the maximum clock speed. In JEOL 9500, the maximum clock speed is 100 MHz. The field size of JEOL 9500 is 1 mm which determines how much area the tool writes before it moves the beam to another location. For most of the devices, they take area less than one field size and this will ensure devices have the highest quality. Some of the devices may require field size more than 1 mm which will result in higher loss due to stitching errors. In order to overcome the high loss problem, we have pro-

posed a novel taper design in this dissertation which is robust to field stitching errors. We will discuss the design in details in Chapter 6.

### 3.4 Etching

Once lithography is completed, the designed pattern is already for transferring. Etching is the subsequent process to transfer the pattern from resist to the underlying material. Resist protects the areas where the material needs to remain, and open areas are etched. Etching is often divided into two classes, wet etching and dry etching. Wet etching utilizes liquid chemicals or etchants to remove materials. Dry etching utilizes a bombardment of ions (usually a plasma of reactive gases) to remove materials. For etching to happen, there are several processes involved: Transport of etchants to surface, surface reaction and removal of product species. These steps are the same for both wet etching and dry etching. Wet etching can be either isotropic or anisotropic. Isotropic wet etching is sometimes useful as we can neglect directions. Anisotropic wet etching is achieved by crystal plane anisotropy, because different crystal planes have different etch rates. Dry etching typically etches fast and anisotropically. This is because of the diffusion speed in the gas phase is faster than in the liquid phase, and the accelerated ions are directional and can easily provide extra energy. Dry etching is particularly useful for materials which are chemically resistant such as silicon carbide.

### 3.5 Cladding

A cladding layer is deposited on top of the device to protect the structure from the environment. There are many techniques used to deposit the cladding layer, such as atomic layer deposition (ALD), PECVD, LPCVD, and even sputtering. All these methods have its own advantages and disadvantages. For example, ALD can provide best uniformity, however, the deposition speed is very slow. So only very thin films are deposited using ALD. PECVD and LPCVD are commonly used to deposit cladding layer in photonics. Compared with LPCVD, PECVD provides faster deposition rate at lower temperature, but as the trade-off, it results in less dense films and potential impurities inside the films. Therefore, we choose to cladding our devices with thinner high quality cladding materials with LPCVD first, and then a thick, lower quality cladding material second.

### 3.6 Chip Processing

Following cladding step, the devices are fully protected and generally no further processing is required. In order to test the devices or conduct packaging, we need to cut the wafer into individual chip. Dicing machines with silicon blades are used to carefully cut through the wafer. The dicing step can be critical to insertion losses of the device. After dicing, devices can be cleaned and tested directly. But in order to reduce insertion losses, each individual chip is generally cleaned and polished to have a very smooth facet which ideally has very low insertion loss. However, polishing is a manual technique that has to be performed on individual chips and it requires use of diamond pads. The

process is expensive and time consuming. Besides, in our experiment, a typical chip has size of  $1\text{ cm} \times 1\text{ mm}$ . For a 4 inch wafer, hundreds of chips can be fabricated at once. So polishing is less practical and no longer scalable. In our process, we adapt an etched facet process. It uses photolithography to define the facets. Follows by etching process and then dice in the etched region to provide individual chips. Etch facet roughness is relied on the etching process which is much smoother than direct dicing. This process can be done in wafer scale and potential used in mass fabrication.

CHAPTER 4  
SILICON NITRIDE PLATFORM: LOSS ORIGIN, MEASUREMENT AND  
REDUCTION

## 4.1 Introduction

Low propagation loss is critical for a variety of photonic applications such as low threshold frequency combs, optical clocks and high precision sensing. High confinement is critical for tailoring the waveguide dispersion to achieve phase matching in nonlinear processes as well as for tighter bends in large-scale photonic systems. A microresonator's quality factor ( $Q$ ) is extremely sensitive to losses. To date, ultra-high  $Q$ 's have been demonstrated only in discrete resonators based on platforms such as polished calcium fluoride ( $\text{CaF}_2$ ), magnesium fluoride ( $\text{MgF}_2$ ) or silica microtoroids with typical cross sectional mode field diameters much larger than the wavelength [11–15]. Spencer et al [16] have recently demonstrated ring resonators with a high  $Q$  of up to 80 million using extremely thin (40 nm)  $\text{Si}_3\text{N}_4$  films, which can be useful for narrowband filtering or building reference cavities for laser stabilization. However, they suffer from highly delocalized optical modes and millimeter-scale bending radii, making it challenging to use these thin film ring resonators for compact photonic routing or nonlinear applications requiring dispersion engineering. High confinement combined with low propagation loss is the key for efficient nonlinear optical processes.

## 4.2 Silicon Nitride Platform

We choose silicon nitride ( $\text{Si}_3\text{N}_4$ ) as our material platform here for several reasons. First, it has a moderately high refractive index (around 2 at wavelength of 1550 nm) which makes it a better light guiding material than silica. For example, the effective area of modes propagating in a  $\text{Si}_3\text{N}_4$  waveguide is normally 1-2 orders of magnitude smaller than the area in an optical fiber. Besides, although  $\text{Si}_3\text{N}_4$ 's index is lower when compared with semiconductors such as silicon, gallium arsenide or other III-V materials, both its linear and nonlinear losses are orders of magnitude smaller than losses in those materials. Furthermore, for nonlinear processes,  $\text{Si}_3\text{N}_4$  has a high nonlinear index ( $n_2 = 2.4 \times 10^{-19} \text{m}^2/\text{W}$ ) which is ten times higher than silica. And with the capability of tailoring the dispersion by engineering the geometry of the waveguide, nonlinear processes can great benefit from using  $\text{Si}_3\text{N}_4$  platform.

Second,  $\text{Si}_3\text{N}_4$  has a wide transparency window from visible to mid-IR ( $\sim 400 \text{ nm}$  to  $3 \mu\text{m}$ ). In addition,  $\text{Si}_3\text{N}_4$  has not been reported to show Raman or Brillouin scattering, unlike silica and silicon. These processes leading to deleterious effects on quantum noise measurements. So these properties of  $\text{Si}_3\text{N}_4$  make it excellent for broadband comb generation, spectroscopy, biological and quantum applications.

Third, and very importantly,  $\text{Si}_3\text{N}_4$  is a material compatible with CMOS technology. It has been already used as a diffusion barrier in CMOS fabrication lines and as a passivation layer for microchips. This compatibility leverages the already existing infrastructure of silicon-based microelectronics and enables massively parallel fabrication of photonic devices at low cost.

All these reasons has proven  $\text{Si}_3\text{N}_4$  to be the ideal material platform for non-linear processes. It combines the beneficial properties of a wide transparency window from visible to mid-IR, the high nonlinear refractive index that enables nonlinear nanophotonics and its CMOS compatibility leverages the cost of fabrication. However, the highest repeatable intrinsic Q in high confinement  $\text{Si}_3\text{N}_4$  ring resonators reported to date is 7 million [10]. So achieving high confinement combined with low propagation loss (high Q) is still challenging. In this chapter, we will discuss the primary sources of optical loss, describe methods to reduce optical loss, measure the losses for a number of devices using different methods and extract the fundamental limit of achievable loss in silicon nitride waveguides.

### 4.3 Loss Origin

Loss from scattering, absorption, and radiation are the three fundamental types of losses for an optical waveguide. Scattering loss occurs at the interface between the core and cladding, when the interface is not perfectly smooth light will scatter. Mode simulations show that light propagating in the waveguide significantly interacts and scatters from both the patterned sidewalls and the top and bottom surfaces (shown in Figure 4.1).

Absorption loss occurs due to the material, when impurities incorporated into the waveguide material light will be absorbed. In our platform, absorption loss is mainly due to O-H bonds in  $\text{SiO}_2$ , and N-H and Si-H bonds [17]. Radiation loss occurs due to waveguide bending when waveguide bend light radiate out. The sharper the bend and the looser the confinement, the larger

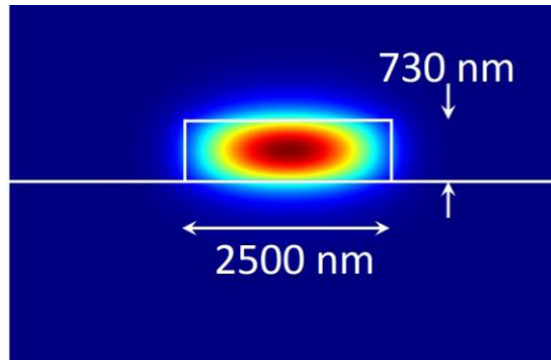


Figure 4.1: **Mode simulation.** Mode simulation of 730 nm tall and 2500 nm wide waveguide showing that the mode is highly confined in the geometry we have chosen. Note that even with highly confined geometry light still interact with all surfaces of the waveguide.

the radiation loss. The radiation loss becomes a major concern when the bend is too small and the light is not well confined in the waveguide. But in general, radiation loss is not the fundamental limiting factor and it can be minimized simply by waveguide design. In our experiment, we use highly confined waveguide which allows us to have negligible radiation loss. Several groups have been working on reducing losses by improving the bulk material properties to achieve high Q. However, to date it has not been clear whether scattering with interfaces or material absorption is the main source of the high loss in the integrated platform. In the dissertation, we show that surface roughness, rather than absorption from the bulk material, plays a major role in the loss limitations of  $\text{Si}_3\text{N}_4$  therefore enabling a path for achieving ultra low-loss devices by addressing the surface quality. We will discuss details in section 4.6.

## 4.4 Loss Reduction

### 4.4.1 Sidewall Roughness Reduction

In order to reduce surface scattering from the sidewalls, we minimize the roughness introduced during the pattern transfer step of the processing by eliminating in-situ polymer formation typical in dry etching processes. Standard waveguide fabrication methods consist of patterning a masking layer, typically photoresist or electron-beam resist, and transferring this pattern into the photonic waveguide device layer using some form of plasma etching. Polymer formation is a common by-product of plasma etching [18,19]. In-situ polymer deposition passivates the sidewalls and enables anisotropic etching with vertical sidewalls desirable for rectangular waveguide fabrication [20]. It also enables pattern transfer to thick waveguide device layers by enhancing selectivity between the mask layer and the films. The polymer formed during this process, while critical for surface passivation and anisotropic etching, often leaves residue on the sidewalls, which introduces sidewall roughness. This roughness adds to the one introduced by the lithography itself [21]. Since the roughness is generally on the order of nanometers, it usually introduces negligible loss; however, it becomes significant in the high Q regimes that we are aiming for here [17,22]. Trifluoromethane ( $\text{CHF}_3$ ) and oxygen ( $\text{O}_2$ ) gases are widely used as standard etchants in  $\text{Si}_3\text{N}_4$  fabrication and this etching chemistry is always accompanied by polymer residue left on the sidewalls [23,24]. In order to reduce this polymer residue on sidewalls, we used a higher oxygen flow to remove in-situ polymer formation, since oxygen reacts with polymer residue to form carbon monoxide ( $\text{CO}$ ) and carbon dioxide ( $\text{CO}_2$ ). Oxygen also reacts with the photoresist which

is generally used in standard etching as the mask to transfer patterns. As a result, higher oxygen flow decreases the etching selectivity, degrading the ability to transfer patterns. To compensate for this effect, we use a silicon dioxide hard mask instead of photoresist to maintain the ability to transfer waveguide patterns while eliminating in-situ polymer formation on the sidewalls using higher oxygen flow. Nitrogen is also added to increase the nitride selectivity over oxide [25,26].

For our standard processing we choose to use MaN-2403 E-beam resist. Before applying the resist, we clean the wafer using either a MOS clean or piranha clean ( $\text{H}_2\text{SO}_4$  and  $\text{H}_2\text{O}_2$ ). We then spin Surpass 3000, an adhesion promoter, on the wafer to ensure the resist will not peel off. We coat the wafer with MaN-2403, spinning at 1000 rpm for 30 s to achieve a resist thickness of approximately 700 nm. The thickness is necessary to survive the etch process, but also limits the smallest feature size because at high aspect ratios the resist can collapse. We then pre-bake the resist for 1 min at 95 °C. In an attempt to mitigate charging at field boundaries, we spin a chemical e-spacer on the wafer at 2000 rpm for 30 s prior to exposure. To expose the resist, we use a dose between 900 and 1000  $\mu\text{C}$ . The resist is developed using a Hamatech spin developer with MiF-726 for 90 s. We also do a hard bake of the resist at 135°C for 5 minutes. The hard bake serves to increase the selectivity of the resist during the etch process. Baking at a higher temperature can cause the resist to reflow. Although this process has been shown to reduce waveguide losses [27,28], it can cause mask erosion during etching which limits the control over waveguide dimensions and leads to trapezoidal waveguide cross-sections. For the improved process, we use silicon dioxide hard mask combine with E-beam resist. We coat the wafer with MaN-2403, spinning at 2000 rpm for 60 s to achieve a resist thickness of approx-

imately 450 nm. We then pre-bake the resist for 1 min at 90°C. To expose the resist, we use a dose between 600 and 700  $\mu\text{C}$ . The resist is developed using a Hamatech spin developer with MiF-726 for 60 s. Then we use reactive-ion etching with improved recipes to transfer the patterns. The fabricated devices are shown in Figure 4.2. The scanning electron microscopy (SEM) shows the fabricated waveguides have smooth sidewall and no observable polymer residue when using the improved etching recipes.

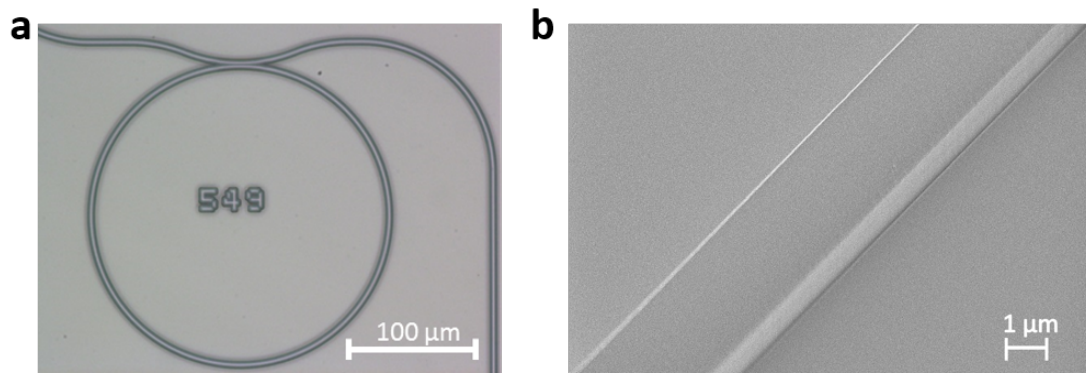


Figure 4.2: **Fabricated devices.** a) Top view optical microscope image of a 115  $\mu\text{m}$  radius ring resonator. b) Scanning electron microscopy image of a fabricated waveguide shows smooth sidewalls using improved etching recipes.

We have also developed a new technique to directly measure waveguide sidewall roughness with conventional atomic force microscopy (AFM). The process is shown in Figure 4.3 (Figure from [29]). We start by protecting straight waveguide segments using 4  $\mu\text{m}$  thick photoresist, with 1.5  $\mu\text{m}$  of resist overlapping each side of the waveguide to protect the sidewalls. Then we etch away 100  $\mu\text{m}$  of the silicon substrate surrounding the waveguide to make a Si-Fin. Oxygens plasma is used to strip the resist, and then we topple over the tall and skinny Si-Fin so that it lies flat on the substrate. Once on its side, the waveguide sidewall can be easily accessed by an AFM equipped with a tip that protrudes

from the AFM cantilever as illustrated in Figure 4.3d.

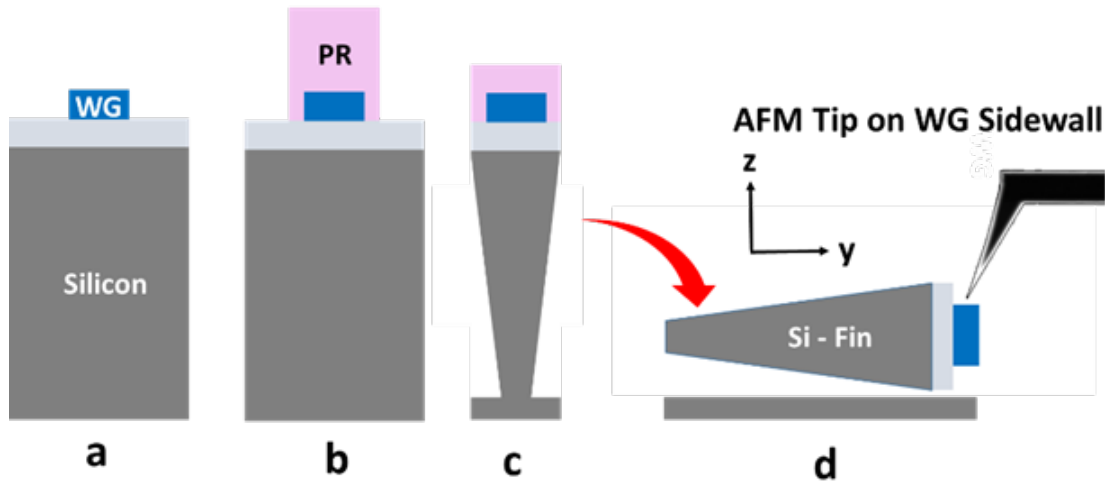


Figure 4.3: **Schematic of waveguide (WG) and Si-Fin fabrication and measurement** a) Linear WG on a Si substrate 25-100  $\mu\text{m}$  long. b) Photoresist is patterned over the WG protecting the sidewalls. c) Si-Fin is etched to be 100 nm tall with WG at its top. d) The Si-Fin with WG is pushed onto its side so the AFM tip can now access the WG sidewall.

With the new AFM measurement method we measure the sidewall roughness of  $\text{Si}_3\text{N}_4$  waveguides patterned using the standard etch recipe and also compared this with the improved etch recipe we mentioned above. The measurements are shown in Figure 4.4. We can see that the improved etch recipe provides us smoother sidewalls. AFM images are taken with the tip moving along the length of the waveguide, acquiring scans several microns long by 500 nm high. Note that in order to compare the etch recipes, we choose to fabricate these devices using the same lithography with a mask written in a mask writer. Lithography-induced roughness can be reduced with E-beam lithography or state of art deep ultraviolet lithography machine.

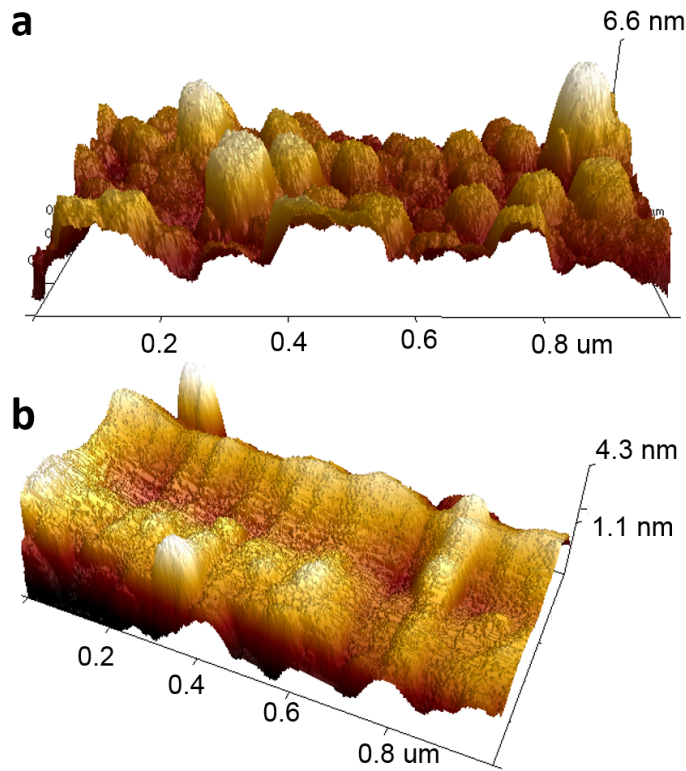


Figure 4.4: **3D AFM measurement of the sidewall roughness.** a) Topography of waveguide sidewall using the Standard Etch, showing 3.9 nm roughness. b) Topography of waveguide sidewall using the new etch, with 2.1 nm roughness.

#### 4.4.2 Top Surface Roughness Reduction

In contrast to standard silicon-based waveguides with losses on the order of 1 dB/cm [30–32] where the sidewall roughness plays the main role in inducing scattering loss, in ultra low-loss  $\text{Si}_3\text{N}_4$  the top surface roughness also plays a major role. Typically, roughness on the top and/or bottom surfaces has not attracted much attention due to the facts that the sidewall roughness was quite significant and many of the previous studies have relied on polished wafers or oxidized wafers from silicon photonics. Here we focus on reducing scattering

loss from the top surface since the  $\text{Si}_3\text{N}_4$  films are deposited using low-pressure chemical vapor deposition (LPCVD), which are not as inherently smooth as polished single-crystal wafers or oxidized wafers. The bottom surface roughness is not addressed here since its roughness, governed by thermal oxidation, is lower than the one governed by the  $\text{Si}_3\text{N}_4$  deposition.

In order to reduce scattering from the top surfaces, we reduce the roughness by chemical mechanical polishing (CMP) the  $\text{Si}_3\text{N}_4$  after the deposition. CMP is a process of smoothing surfaces with the combination of chemical and mechanical forces. Typical CMP tools consist of a rotating and extremely flat plate which is covered by a pad shown in Figure 4.5.

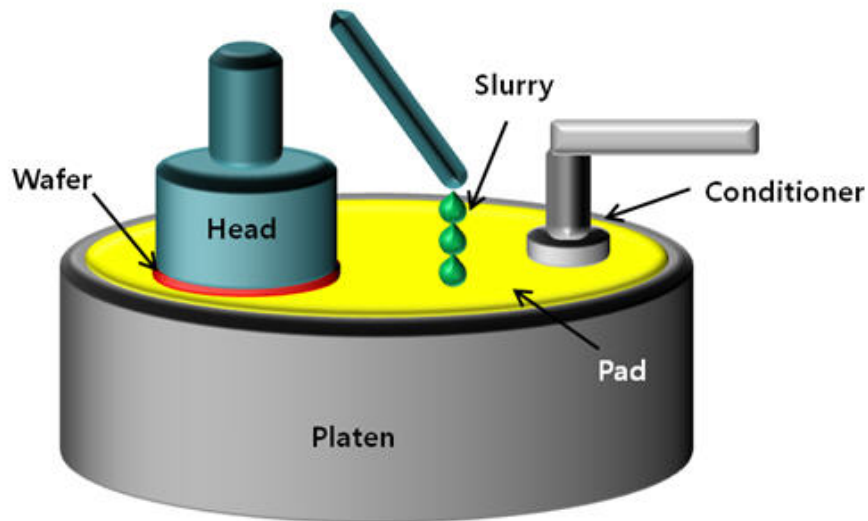


Figure 4.5: **Functional principle of chemical mechanical polishing.** The wafer that is being polished is mounted upside-down in a carrier/spindle and a slurry introduction mechanism deposits the slurry on the pad. Both the plate and the carrier are then rotated and the carrier is kept oscillating to remove the material which creates a smooth surface.

The atomic force microscopy (AFM) scans before and after the optimized

polishing step are shown in Figure 4.6 and Figure 4.7. The root mean squared (RMS) roughness is decreased from 0.38 nm to 0.08 nm. Two most important factors affecting the RMS roughness are: CMP pad and slurry. We have shown AFM measurements of  $\text{Si}_3\text{N}_4$  surface roughness using different CMP pads and slurries in Figure 4.8 and Figure 4.9.

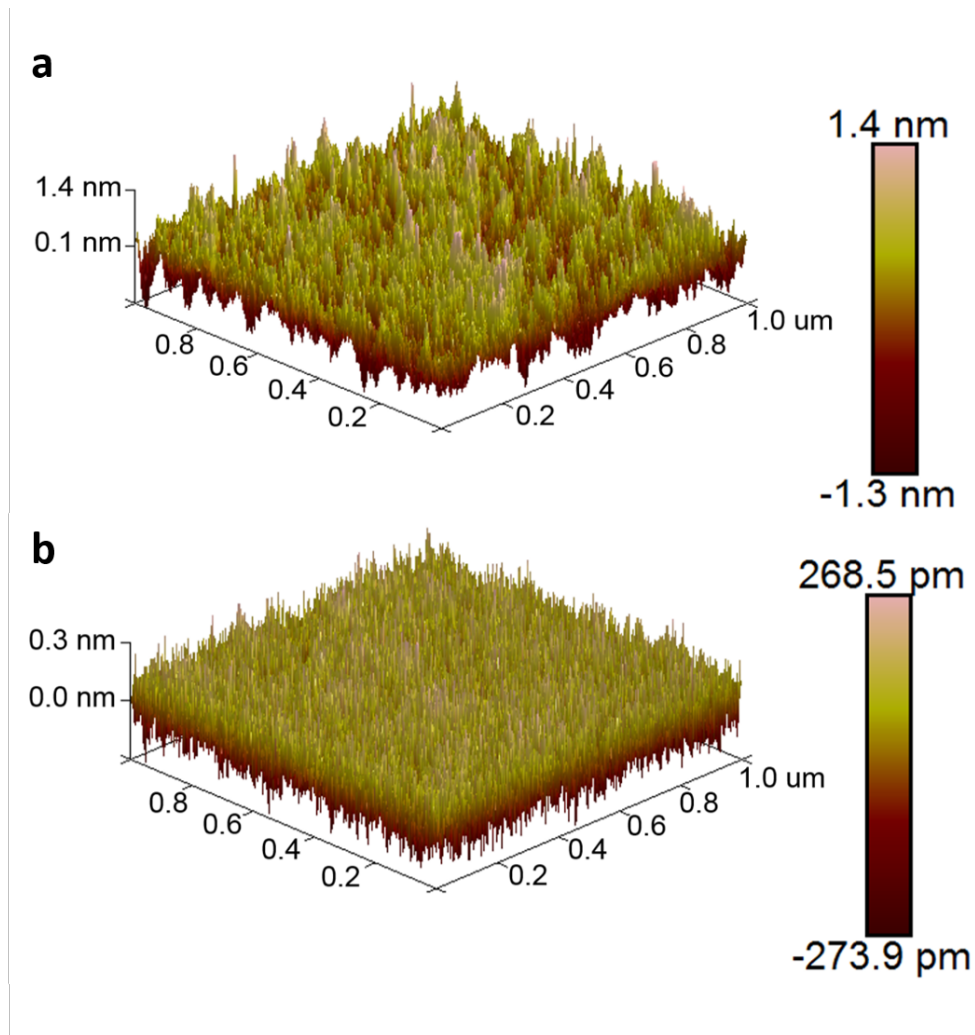


Figure 4.6: **The atomic force microscopy (AFM) scans of the top surface of  $\text{Si}_3\text{N}_4$  before and after the polishing step.** a) 3D AFM scan of the top surface of  $\text{Si}_3\text{N}_4$  before polishing with RMS roughness of 0.38 nm and correlation length of 29 nm. b) 3D image of the top surface of  $\text{Si}_3\text{N}_4$  after polishing with RMS roughness of 0.08 nm and correlation length of 8.76 nm.

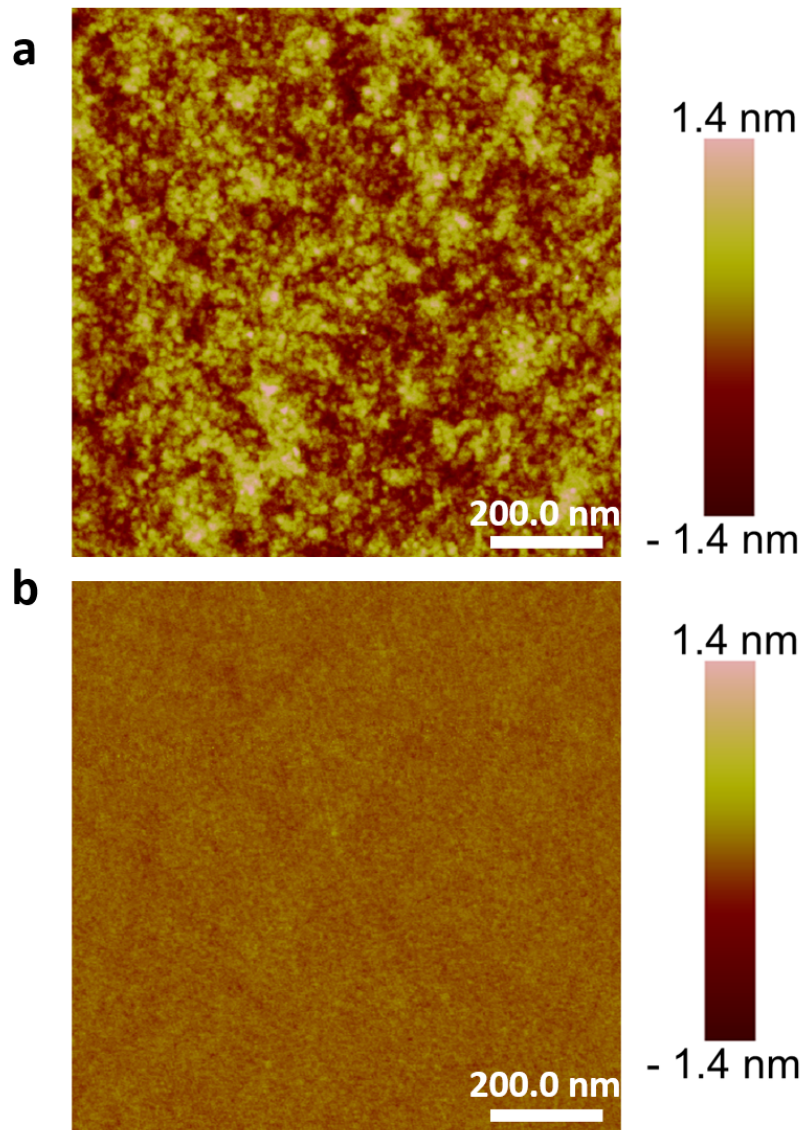


Figure 4.7: **The atomic force microscopy (AFM) scans of the top surface of  $\text{Si}_3\text{N}_4$  before and after the polishing step.** a) 2D image of the top surface of  $\text{Si}_3\text{N}_4$  before polishing and scaled to -1.4 to 1.4 nm with RMS roughness of 0.38 nm and correlation length of 29 nm. b) 2D image of the top surface of  $\text{Si}_3\text{N}_4$  after polishing and scaled to -1.4 to 1.4 nm with RMS roughness of 0.08 nm and correlation length of 8.76 nm.

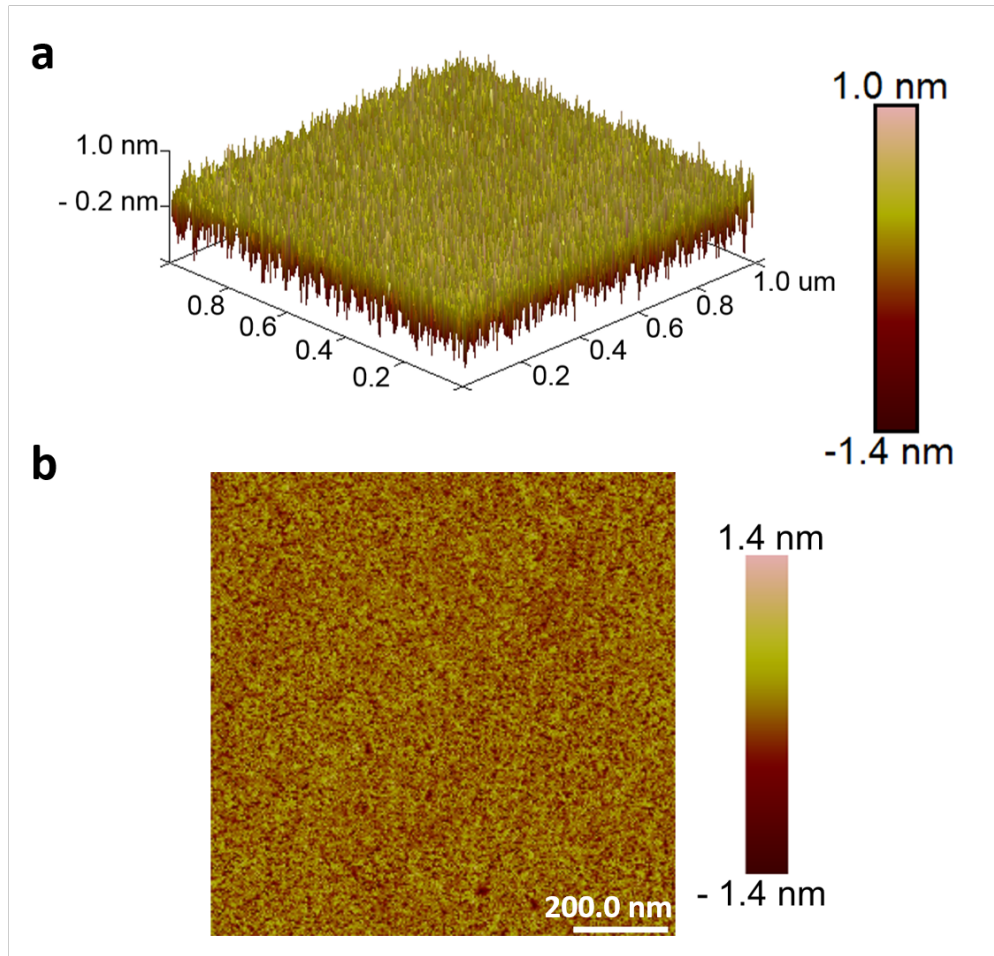


Figure 4.8: **The atomic force microscopy (AFM) scans of the top surface of  $\text{Si}_3\text{N}_4$  using a different pad.** a) 3D AFM scan of  $\text{Si}_3\text{N}_4$  top surface after CMP using a different polishing pad with RMS roughness of 0.32 nm. b) 2D image of  $\text{Si}_3\text{N}_4$  top surface before CMP and scaled to -1.4 to 1.4 nm with RMS roughness of 0.32 nm.

Our AFM measurements indicate that different polishing conditions can affect strongly the RMS roughness. By comparing Figure 4.8 with Figure 4.6b, one can see that the pad selection has a significant effect on reducing  $\text{Si}_3\text{N}_4$  top surface RMS roughness. Comparing Figure 4.9 with Figure 4.7b, one can see that the slurry selection has a significant effect on RMS roughness uniformity. While the RMS roughness is reduced, it has more randomness.

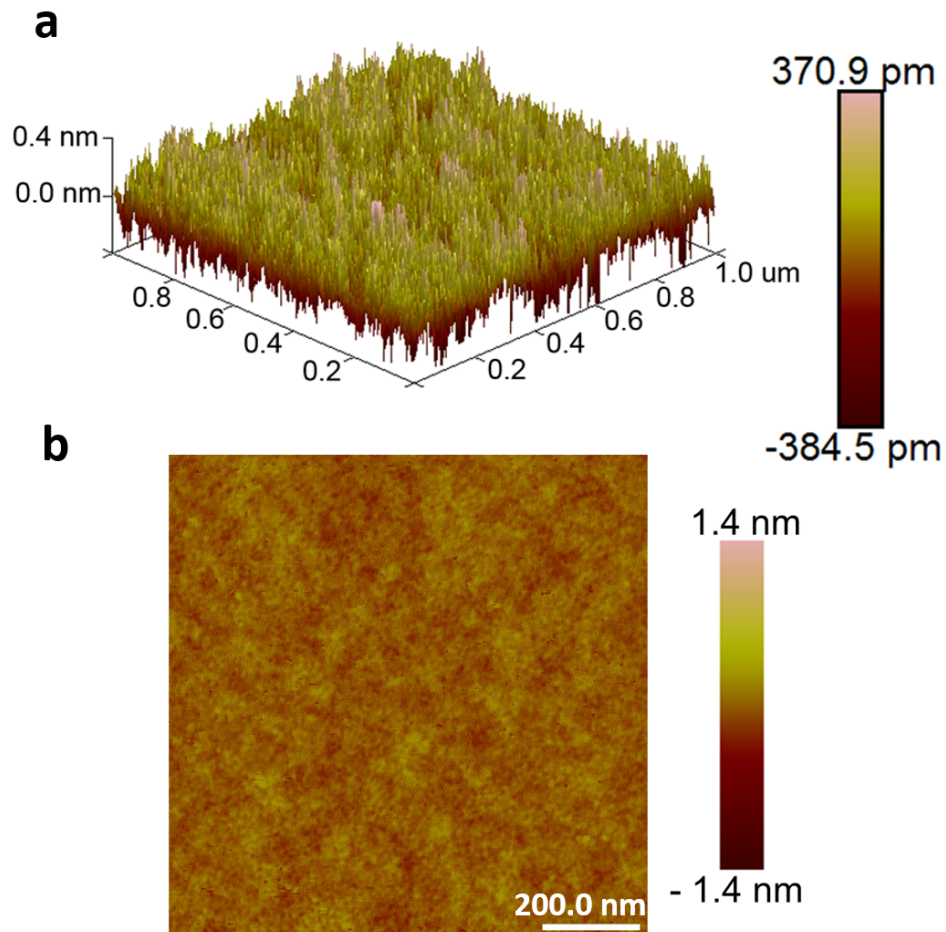


Figure 4.9: **The atomic force microscopy (AFM) scans of the top surface of  $\text{Si}_3\text{N}_4$  using a different slurry.** a) 3D image of  $\text{Si}_3\text{N}_4$  top surface after CMP using a different slurry with RMS roughness of 0.11 nm. b) 2D image of  $\text{Si}_3\text{N}_4$  top surface after CMP and scaled to -1.4 to 1.4 nm with RMS roughness of 0.11 nm.

### 4.4.3 Lithography-Induced Roughness Reduction

Line edge roughness from patterning the resist contribute to scattering loss [33–35], so in order to further decrease the loss, we apply multipass lithography to reduce line edge roughness. Electron beam (E-beam) lithography, extensively used for patterning optical waveguides, creates a line edge roughness which introduces extra roughness to the sidewalls. During E-beam lithography, any instability, such as beam current fluctuations, beam jitter, beam drift, stage position errors and mechanical vibrations, can generate statistical errors which result in extra line edge roughness in the patterns which will add roughness to the sidewalls. The principle of multipass lithography (Figure 4.10) [34, 35] consists of exposing the same pattern multiple times at a lower current to reduce line edge roughness by averaging statistical errors.

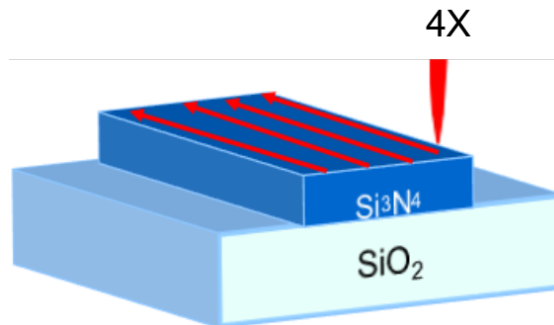


Figure 4.10: **Schematic of multipass.** The same pattern is exposing multiple times at a lower current to reduce line edge roughness by averaging statistical errors.

## 4.5 Loss Measurement

There are a few well known methods to measure the loss of optical waveguides. The first method is the cut-back method which is originally developed in the fiber industry. The loss is continuously measured while the fiber is cut-back. In this way, the loss can be measured per length very accurately. However, it is not easy to directly implement this method in integrated structures. The structures are designed and fabricated beforehand, it is not possible to actively reduce the length of the structures. And this method will also require long waveguide and more than a single device to avoid any random defects which may influence the loss. The second method is the measurement of the Q, as we have discussed previously, a microresonator's Q is extremely sensitive to losses. By measuring the Q, we can get a value for the loss. The final method for calculating losses is the Fabry-Perot method. In this method, the chip facets act as mirrors and the Fabry-Perot maximum and minimum are measured to derive the losses in the waveguide. In our experiments, we have used the first two methods, we use cut-back for measuring waveguide structures loss and Q measurement for resonator structures loss. In this section, we focus on the Q measurement to determine the loss.

The intrinsic Q of resonator provides us a very sensitive method of estimating propagation loss, the loss can be written as [36]:

$$\alpha = \frac{2\pi n_g}{Q_i \lambda_0} = \frac{\lambda_0}{Q \cdot R \cdot FSR} \quad (4.1)$$

where  $\alpha$  is the per unit propagation loss,  $n_g$  is the group index,  $\lambda_0$  is the resonant wavelength,  $R$  is the radius of the ring resonator, and  $FSR$  is the free spectral range. As we have discussed in section 2.2, the quality factor measured in the experiment is called the loaded Q or  $Q_L$ , it includes all the loss mechanisms,

and is determined by the measured full-width-half-maximum linewidth of the resonator.

In order to measure  $Q_L$  in the experiment, a laser scanning technique is used to measure the transmission spectra and the linewidth of the resonator (FWHM). We launch light from a tunable laser source which is then transmitted through a fiber polarization controller and coupled into our device via an inverse nanotaper using a lensed fiber. We collect the output of the resonator through another inverse nanotaper and an objective lens. We monitor the output on a high-speed InGaAs photodetector. The frequency of the laser is measured using a wavemeter with a precision of 0.1 pm and the laser detuning is calibrated by monitoring the fringes of a reference fiber based Mach-Zehnder interferometer with a known free spectral range. From the  $Q_L$  measurement, the propagation loss of the resonator can be calculated.

We have fabricated four sets of ring resonators according to different processes discussed in section 4.4. All the rings have a radius of  $115\ \mu\text{m}$ , a height of 730 nm and a width of 2500 nm, and are coupled to a waveguide of the same dimensions. We measure the Q and calculate the propagation loss using the techniques described above. We measured the ring resonators in the undercoupled regime so that the measured Q is close to their intrinsic Q. The transmission spectrum of ring resonators using standard process we reported in Ref [10] is shown in Figure 4.11. The measured intrinsic Q is  $5.6 \pm 0.7$  million corresponding to propagation loss of  $5.2 \pm 0.6$  dB/m.

The transmission spectrum of ring resonators using our optimized etch process but without CMP and without multipass lithography is shown in Figure 4.12. The measured intrinsic Q is  $16.2 \pm 2.9$  million corresponding to propaga-

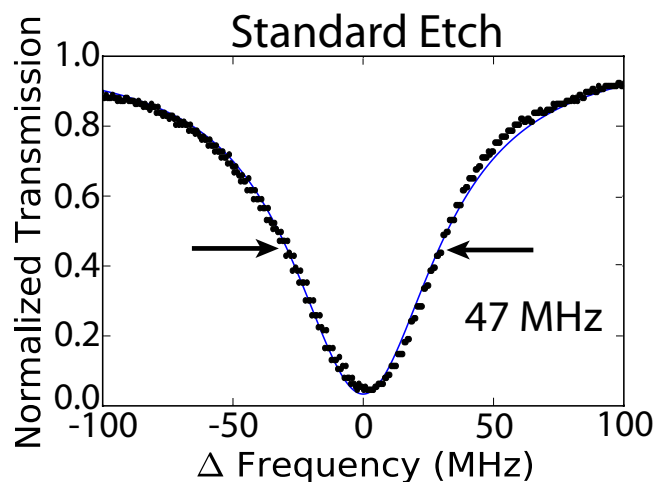


Figure 4.11: **Normalized transmission spectrum of device using standard process.** Normalized transmission spectrum of ring resonators fabricated using the standard process reported in Ref. 44 with a measured full width half maximum (FWHM) of 47 MHz.

tion loss of  $1.8 \pm 0.3$  dB/m.

The transmission spectrum of ring resonators using both the optimized etch recipe and CMP but without multipass lithography is shown in Figure 4.13. The measured intrinsic Q is  $28 \pm 4.7$  million corresponding to propagation loss of  $1.1 \pm 0.2$  dB/m.

The transmission spectrum of ring resonators using all the techniques including the optimized etch recipe, surface smoothing technique and multipass lithography is shown in Figure 4.14. The measured intrinsic Q is  $37 \pm 6$  million corresponding to propagation loss of  $0.8 \pm 0.1$  dB/m. Note that these estimated propagation losses are upper bounds on the losses in straight waveguides since in a ring the optical mode interacts more strongly with the sidewalls due to bending. Mode splitting, commonly observed in ultra-high Q system such as whispering-gallery-mode microresonators [37–39], is induced due to

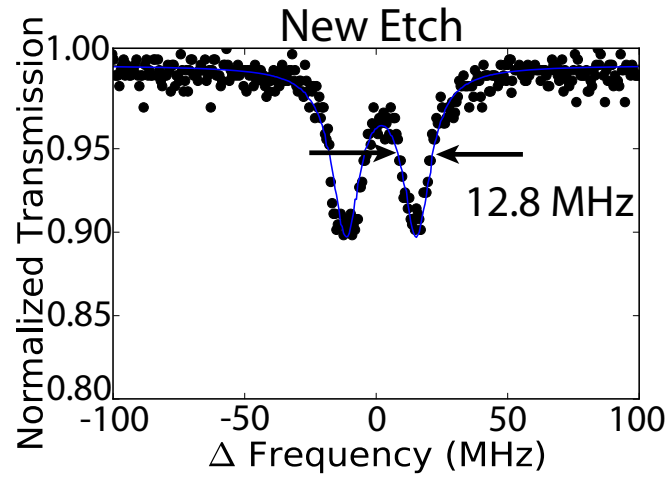


Figure 4.12: **Normalized transmission spectrum of device using only optimized etch process.** Normalized transmission spectrum of ring resonators fabricated using optimized etch process but without our new surface smoothing technique and multipass lithography with a measured FWHM of 12.8 MHz.

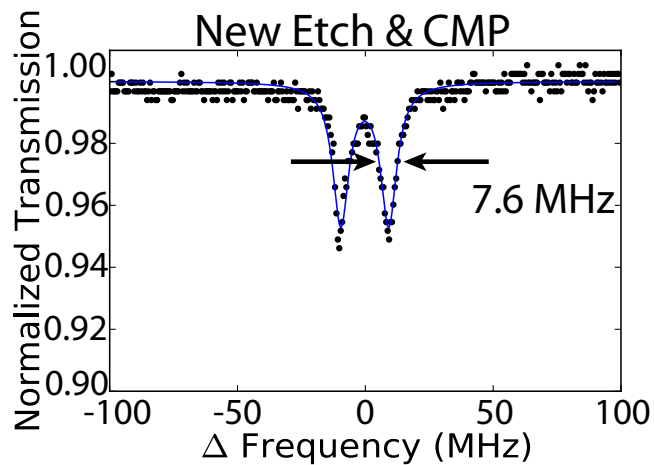


Figure 4.13: **Normalized transmission spectrum of device using both the optimized etch recipe and surface smoothing techniques.** Normalized transmission spectrum of ring resonators fabricated using both the optimized etch recipe and surface smoothing techniques but without multipass lithography with a measured FWHM of 7.6 MHz.

light backscattering from fabrication imperfections or surface roughness. When the Q is high and the mode is highly confined, extremely small defects or roughness can induce a visible splitting.

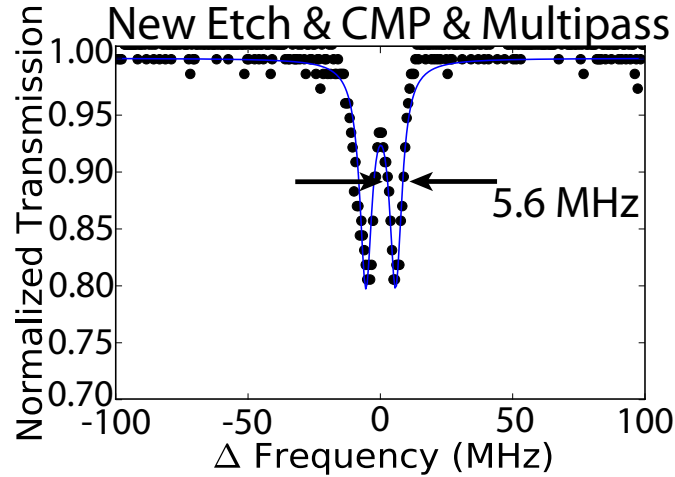


Figure 4.14: **Normalized transmission spectrum of device using all the techniques.** Normalized transmission spectrum of ring resonators fabricated using all the techniques including the optimized etch recipe, surface smoothing technique and multipass lithography with a measured FWHM of 5.6 MHz.

## 4.6 Fundamental Loss Limit Extraction

In order to extract the fundamental limit of achievable loss in silicon nitride waveguides, we compare the losses of two different structures that have different mode interactions with the sidewalls. We fabricated two devices with waveguide widths of 2.5 microns and 10 microns on the same wafer to ensure that the fabrication processes are identical. Both rings have the same height of 730 nm and both of them are coupled to a waveguide of the same dimensions (730 nm  $\times$  2500 nm). The mode simulation with different interaction strength with sidewalls is shown in Figure 4.15.

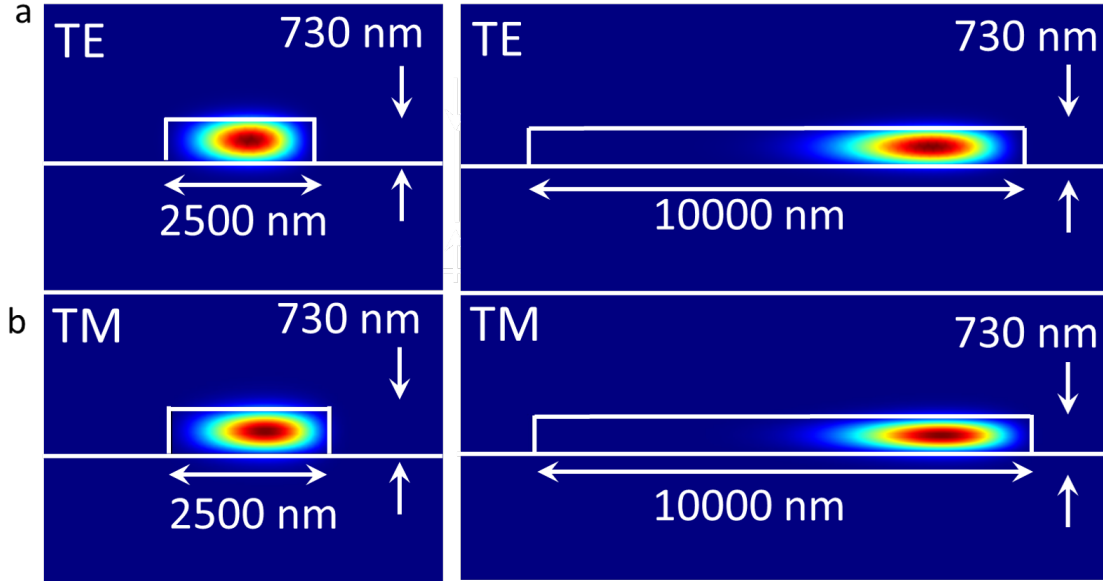


Figure 4.15: **Mode simulation for ring resonators with different interaction strength with the sidewalls.** a) TE Mode profile of waveguides that are  $2.5 \mu\text{m}$  and  $10 \mu\text{m}$  wide and  $730 \text{ nm}$  height. b) Same as a) but for TM.

As we have discussed in section 4.5, we used the Q measurement method to determine the loss. The measured transmission spectra for the rings with  $2.5 \mu\text{m}$  width and  $10 \mu\text{m}$  width in TE and TM polarization are shown in Figure 4.16.

The measured intrinsic Q is  $67 \pm 7$  million for the TE mode and  $59 \pm 12$  million for the TM mode. At these ultra-high Qs, one is operating near the limits of Q that can be reliably estimated by scanning a laser across a resonance. Hence, we corroborate these Q measurements by performing a cavity ring-down experiment for the TM mode [40–42]. As shown in Figure 4.17, the measured lifetime is  $25.6 \pm 1.3 \text{ ns}$ , which corresponds to an intrinsic Q of  $63 \pm 3$  million, consistent with our measurement of the Q, using a laser scanning technique.

We estimate the fundamental loss limit given by the bulk absorption of  $\text{Si}_3\text{N}_4$  in our films ( $\alpha_{totalabsorption}$ ) by comparing the losses for the two structures

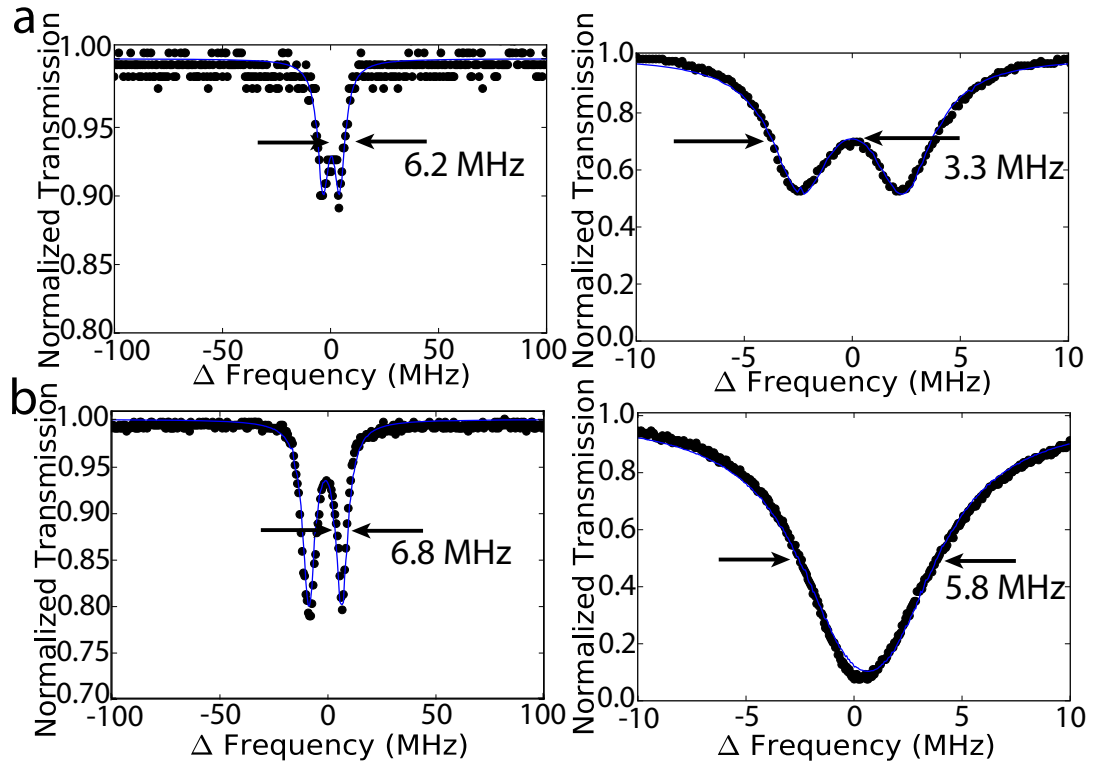


Figure 4.16: **Normalized transmission spectra for ring resonators with different interaction strength with the sidewalls.** a) Measured normalized TE transmission spectra for the ring resonator composed of the  $2.5 \mu\text{m}$  wide waveguide (left) with a measured full width half maximum (FWHM) of 6.2 MHz and the measured spectra for the ring resonator composed of the  $10 \mu\text{m}$  wide waveguide (right) with a measured FWHM of 3.3 MHz in TE polarization using the optimized fabrication process. b) TM transmission spectra for the rings with narrower (left) and wider (right) waveguide with FWHM of 6.8 MHz and 5.8 MHz, respectively.

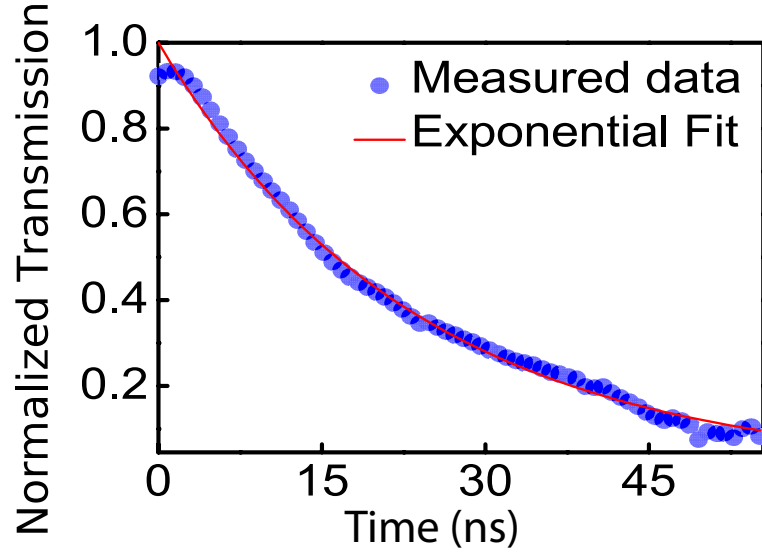


Figure 4.17: **Cavity ring-down measurement on TM mode.** The measured lifetime is extracted from the exponential fit to be  $25.6 \pm 1.3$  ns.

extracted from the transmission measurements ( $\alpha_{ring} \approx 0.79 \pm 0.14$  dB/m and  $\alpha_{widering} \approx 0.43 \pm 0.046$  dB/m) and considering the absorption of the rings with narrower and wider waveguides to be:

$$\alpha_{ring} = \alpha_{top\ absorption} + \alpha_{top\ scatter} + \alpha_{bottom\ scatter} + \alpha_{sidewalls\ scatter} \quad (4.2)$$

$$\alpha_{wide\ ring} = \eta_1 \alpha_{top\ absorption} + \eta_2 (\alpha_{top\ scatter} + \alpha_{bottom\ scatter}) + \eta_3 \alpha_{sidewalls\ scatter} \quad (4.3)$$

$\eta_1$ ,  $\eta_2$ ,  $\eta_3$  are the factors that account for the interaction of the field with the waveguide core, the top and bottom surfaces, and sidewalls respectively for the wider waveguides relative to the narrower waveguide [43] and are calculated using FEM simulations (performed with COMSOL) to be 1.010, 1.002 and 0.138 respectively.

We have chosen bending radius to be  $115 \mu\text{m}$  and  $367 \mu\text{m}$  which ensure the bending loss to be negligible in high confinement waveguide. So the total loss

can be written as:

$$\alpha = \alpha_{total\ scatter} + \alpha_{total\ absorption} \quad (4.4)$$

$$\alpha_{total\ scatter} = \alpha_{top\ scatter} + \alpha_{bottom\ scatter} + \alpha_{sidewalls\ scatter} \quad (4.5)$$

$$\alpha_{absorption} = \alpha_{top\ scatter} + \alpha_{bottom\ scatter} + \alpha_{sidewalls\ scatter} \quad (4.6)$$

$\alpha_{total\ scatter}$  is the total scatter loss,  $\alpha_{top\ scatter}$  is the scatter loss from top surface,  $\alpha_{bottom\ scatter}$  is the scatter loss from bottom surface,  $\alpha_{sidewalls\ scatter}$  is the scatter loss from sidewalls.

The surface scattering loss can be estimated from Payne-Lacey model [44]. Payne-Lacey model relates scattering loss to the surfaces RMS ( $\sigma$ ) roughness, correlation length ( $L_c$ ), waveguide geometry and spectral density function. The equation for Payne-Lacey model can be written as:

$$\alpha_{scatter} = \frac{\sigma^2}{\sqrt{2}k_0d^4n_{core}}g(V)f_e(x, \gamma) \quad (4.7)$$

$$g(V) = \frac{U^2V^2}{1+W} \quad (4.8)$$

$$f_e(x, \gamma) = \frac{x\{[(1+x^2)^2 + 2x^2\gamma^2]^{1/2} + 1 - x^2\}^{1/2}}{[(1+x^2)^2 + 2x^2\gamma^2]^{1/2}} \quad (4.9)$$

where  $\alpha_{scatter}$  is the surface scattering loss in dB per unit length,  $\sigma$  is the root mean squared (RMS) surface roughness,  $d$  is the waveguide half width,  $k_0$  is the free-space wavenumber, the function  $g(V)$  is determined purely by the waveguide geometry, the function  $f_e(x, \gamma)$  describes the integral over the spectral density function.  $U, V, W$  are normalized waveguide parameters.  $x$  represents a normalized correlation length,  $\gamma$  is related with confinement factor and index step of the waveguide.

$$\Delta = \frac{n_{core}^2 - n_{clad}^2}{2n_{core}^2} \quad (4.10)$$

$$x = W \frac{L_c}{d} \quad (4.11)$$

$$\gamma = \frac{n_{clad} V}{n_{core} W \sqrt{\Delta}} \quad (4.12)$$

$$U = d \sqrt{n_{core}^2 k_0^2 - \beta^2} \quad (4.13)$$

$$V = k_0 d \sqrt{n_{core}^2 - n_{clad}^2} \quad (4.14)$$

$$W = d \sqrt{\beta^2 - n_{clad}^2 k_0^2} \quad (4.15)$$

$n_{core}$  and  $n_{clad}$  are the refractive indices of the core and cladding materials,  $\beta$  is the modal propagation constant and  $L_c$  is the correlation length.

From the equations described above, we can estimate the  $\alpha_{top\ scatter} \approx 0.0066$  dB/m ( $\pm 0.001$  dB/m) and  $\alpha_{bottom\ scatter} \approx 0.2408$  dB/m ( $\pm 0.02$  dB/m). The scattering losses due to the sidewalls  $\alpha_{sidewalls\ scatter}$  and the bulk loss are then extracted using Equation 3.6 and Equation 3.7. The sidewalls  $\alpha_{sidewalls\ scatter}$  is  $0.41 \pm 0.05$  dB/m and the bulk loss  $0.13 \pm 0.05$  dB/m, which corresponds to an absorption-loss-limited Q of at least 170 million. Note that here we are assuming that both sidewalls have the same loss as they are experiencing the same Ebeam lithography and plasma etching conditions, and the loss in the oxide cladding is negligible when compared to the loss in the  $\text{Si}_3\text{N}_4$  due to the high degree of confinement. From the results, we clearly see that surface roughness, rather than absorption from the bulk material, plays a major role in the loss limitations of  $\text{Si}_3\text{N}_4$  therefore enabling a path for achieving ultra low-loss devices by addressing the surface quality.

## 4.7 Sub-Milliwatt Optical Parametric Oscillation

Simultaneous achieve high Q and high confinement in ring resonators is important for nonlinear processes. We have shown a overview of Q vs confinement in the past decade using  $\text{Si}_3\text{N}_4$  platform in Figure 4.18 [10,16,17,19,27,45–47].

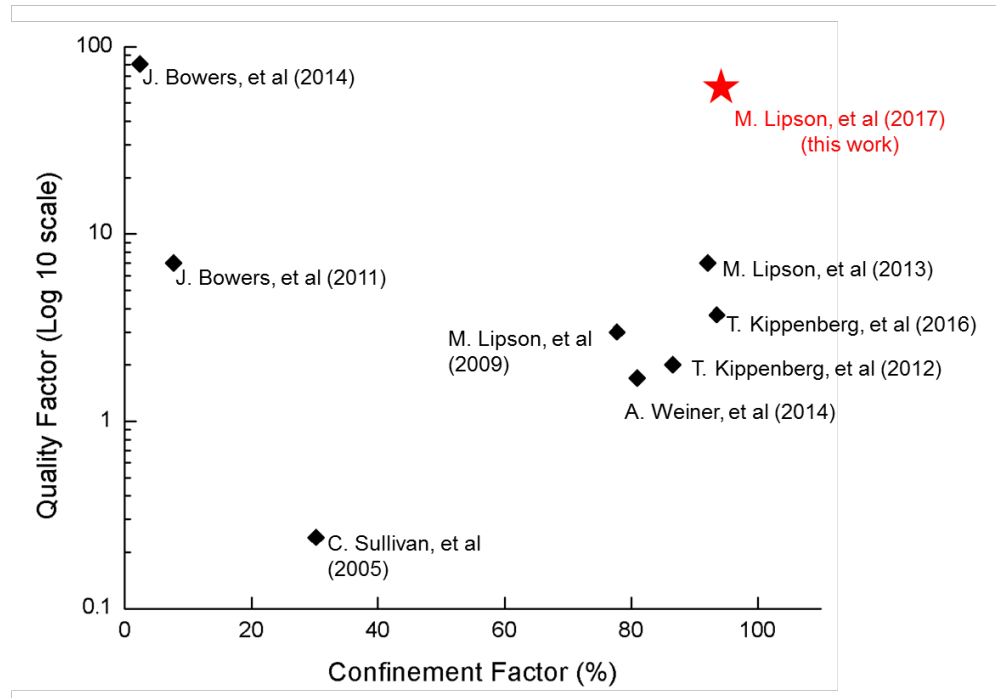


Figure 4.18: **Overview of Q vs confinement factor in the past decade using  $\text{Si}_3\text{N}_4$  platform.** The red star shows that we are able to simultaneous achieve high Q and high confinement in this work. We have achieved Q of  $67 \pm 7$  million with confinement factor more than 90%.

In order to illustrate the importance of simultaneous high Q and high confinement ring resonators we demonstrate a strong decrease in the threshold for optical parametric oscillation down to the sub-milliwatt-level with the decrease of optical losses. To determine the threshold for parametric oscillation, we measured the output power in the first generated four-wave-mixing (FWM) sideband for different pump powers. Figure 4.19a shows the data for a device

pumped at the resonance near 1557 nm with a loaded Q of 35 million. The average threshold power is  $330 \pm 70 \mu\text{W}$ , comparable to the theoretically estimated threshold power of  $206 \mu\text{W}$  using the expression [48, 49]:

$$P_{th} \approx 1.54 \left(\frac{\pi}{2}\right) \frac{Q_c}{2Q_L} \frac{n^2 V}{n_2 \lambda Q_L^2} \quad (4.16)$$

where  $\lambda$  is the pump wavelength,  $n$  is the linear refractive index,  $n_2$  is the nonlinear refractive index ( $n_2 = 2.4 \times 10^{-19} \text{m}^2/\text{W}$ ) [50],  $V$  is the resonator mode volume,  $Q_c$  and  $Q_L$  are the coupling and loaded quality factors of the resonators. This is the lowest and the first sub-milliwatt power threshold parametric oscillation in planar nonlinear platforms [51–55] reported to the best of our knowledge. In addition, this threshold power is close to the lowest threshold reported in ultra-high Q microresonators such as  $\text{CaF}_2$  [55] and silica microtoroids [56]. We also measure and plot the thresholds for rings with various loaded quality factors in Figure 4.19b. The threshold powers follow the theoretically predicted trend of being inversely proportional to  $Q_L^2$ .

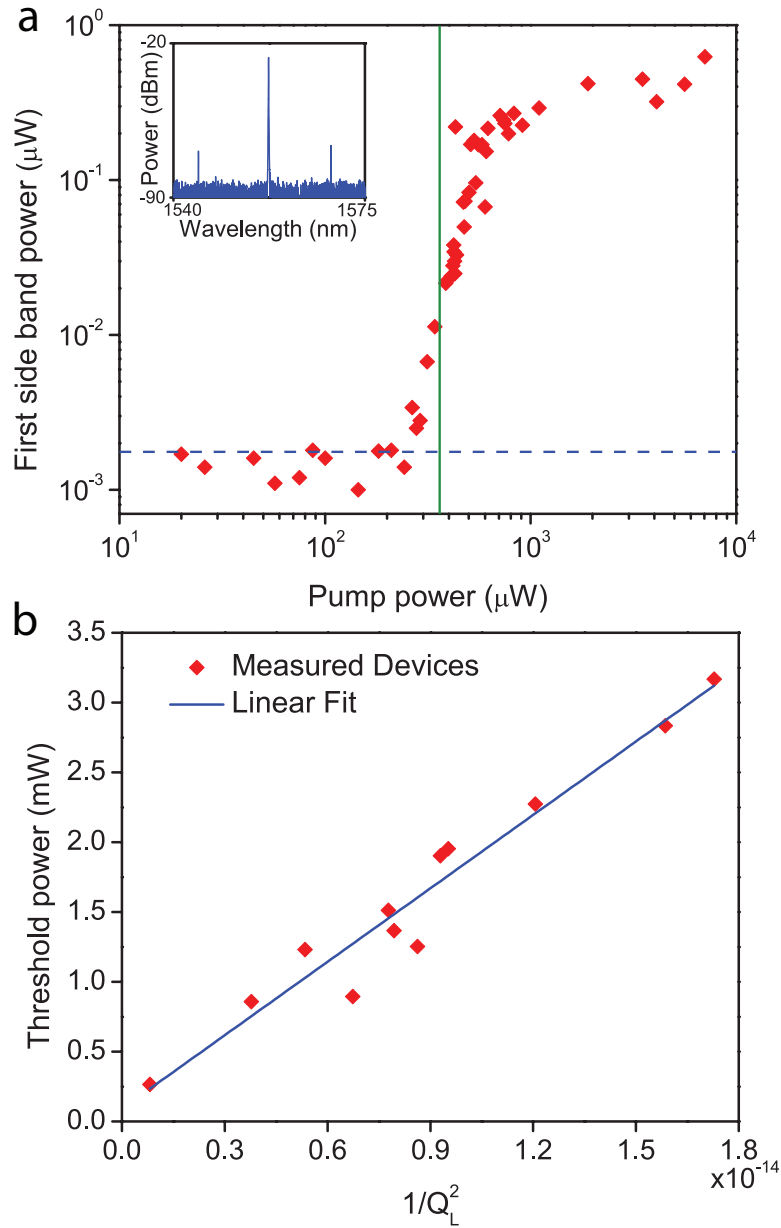


Figure 4.19: **Oscillation threshold decrease with decrease of losses.** a) The output power in the first generated mode as a function of the pump power. In this device, parametric oscillation occurs for a pump power of  $330 \pm 70 \mu\text{W}$  (indicated by the solid green vertical line). Note that the first band appears more than one free spectral range away from the pumped resonance. b) Measured threshold power for micro-resonators with different fabrication processes as a function of the loaded quality factor ( $Q_L$ ). Threshold powers approximately follow the theoretically predicted trend of being inversely proportional to  $Q_L^2$ .

## 4.8 Summary

We drastically and systematically reduced losses in high-confinement resonators by using methods for reducing roughness from waveguide interfaces. Moreover, we demonstrate optical parametric oscillation in an on-chip microresonator with sub-milliwatt pump powers. We extract the absorption-limited  $Q$  of the ring resonator to be at least 170 million, which indicates that we are still limited by the scattering loss, thereby providing a path for achieving ultra-low-loss resonators simply via addressing the scattering loss. Our work provides an on-chip platform for devices with performance that could be comparable to the performance achieved in discrete large devices.

CHAPTER 5  
CHIP-BASED FREQUENCY COMB SOURCES FOR OPTICAL  
COHERENCE TOMOGRAPHY

## 5.1 Introduction

### 5.1.1 Frequency Combs

An optical frequency comb is a light source whose spectrum consists of a series of discrete, equally spaced frequency lines. The 2005 Nobel Prize in Physics was awarded to Hall and Hansch in part for the development of frequency combs [57].

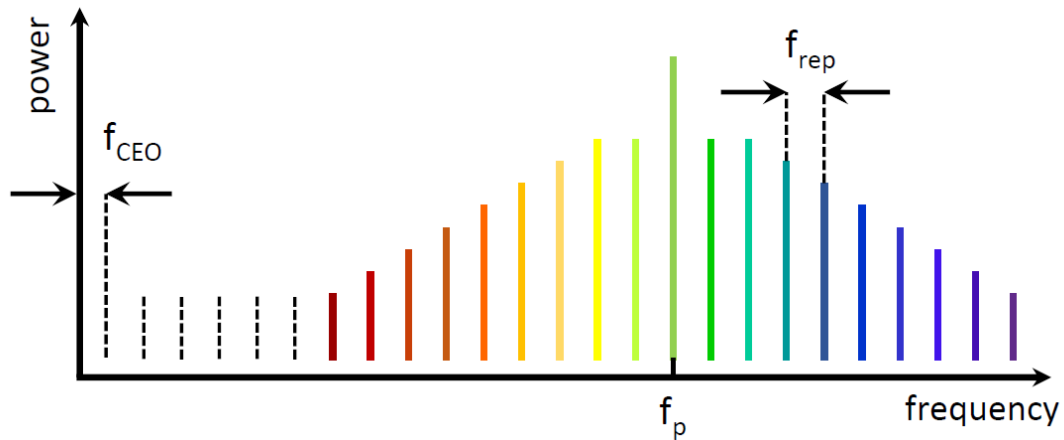


Figure 5.1: **General spectrum of a frequency comb.** Comb lines are separated by precise spacing  $f_{rep}$  and carrier envelope offset  $f_{CEO}$ .

The frequency domain representation of a perfect frequency comb (Figure

5.1) is a series of delta functions spaced according to

$$f_{comb} = f_{CEO} + n f_{rep} \quad (5.1)$$

where  $n$  is an integer,  $f_{rep}$  is the comb tooth spacing (equals to the repetition rate of the pluses), and  $f_{CEO}$  is the carrier offset frequency which is the frequency offset between the lowest order comb line and zero-frequency (DC). The frequencies of these lines are known to a very high degree of accuracy, which makes frequency combs an important tool in application such as optical metrology and high-resolution spectroscopy [58–60]. In other words, frequency combs can be used as a high precision frequency “ruler”.

The most popular way of generating a frequency comb is with a mode-locked laser. Such lasers produce a series of optical pulses separated in time by the round-trip time of the laser cavity. The spectrum of such pulse train consists of a series of comb lines separated by the repetition rate of the laser. The most common lasers used for frequency-comb generation are Ti:sapphire or Er:fiber lasers. However, in recent years, there has been progress in the development of frequency combs based on compact, chip-scale microresonators. These microresonators based combs leverages the third-order (Kerr) nonlinearity of dielectric or semiconductor materials inside an optical microcavity through four-wave mixing (FWM) process, in which two photons interact to generate light at new frequencies. Here, a single continuous wave (CW) laser is coupled into a microresonator and the FWM gain increases with cavity circulating power. At low powers, FWM gain is lower than round-trip loss, the system is below threshold, so only spontaneous FWM sidebands are transiently generated at the single-photon levels. We use an example of different generated frequency combs states from our device here (details can be found in [1]) to help explain.

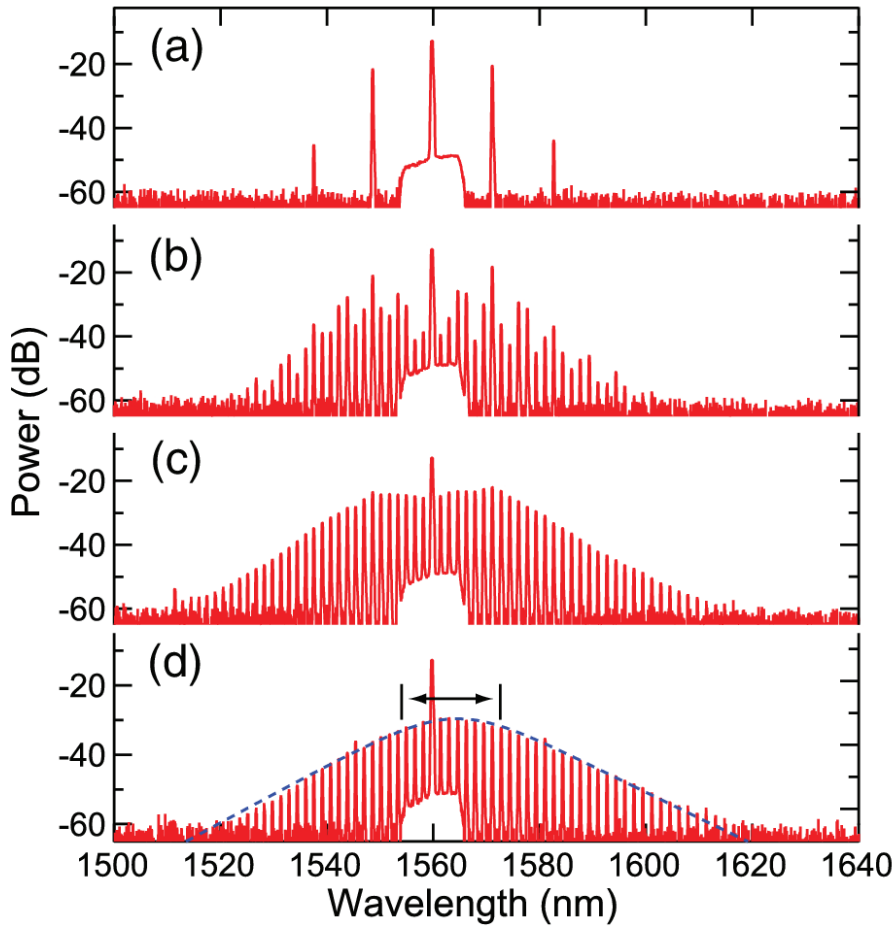


Figure 5.2: **Example of different frequency comb states.** Example of generated frequency comb spectra for different cavity resonance detunings produced by terminating the heater current scan at different values. a) the initial cascaded FWM. b) the mini-comb formation. c) chaotic-like states. d) single soliton state with a hyperbolic secant squared envelope (blue dashed curve). Details can be found in [1].

When the laser is tuned into a resonance toward the cavity resonance, the circulating power is increased. At the point where the FWM gain exceeds the round-trip loss, the oscillation threshold is reached, FWM sidebands are generated at an integer number of FSRs away from the laser frequency (Figure 5.2a). As the pump circulating power keeps increasing (tuning more into resonance), additional sidebands are generated through mutual interactions between comb

lines, to the point where each cavity FSR contains a frequency comb line. At this point, the comb lines generally have random or uncorrelated phases with respect to each other (Figure 5.2b). As the pump detunes farther into the resonance, the comb enters a chaotic-like state (Figure 5.2c). After further detuning, the nonlinear interactions form a phase-locked state, also known as soliton state where in the time domain, it emits a series of pulses. Prior to this state, several multi-soliton states can exist, in which multiple soliton pulses circulate in the cavity. These states transition by successively shedding solitons, until only a single soliton is left. A hyperbolic secant squared envelope in the frequency domain indicates the single soliton state (Figure 5.2d).

Microresonator frequency combs were first developed in the near-IR telecom range (1550 nm) [61, 62], but have since spread to both the visible [63–65] as well as mid-IR wavelengths [66, 67]. This spread is fueled by unique applications, such as biological imaging in the visible and optical spectroscopy in the mid-IR. Several challenges have slowed the progress of frequency combs at these wavelengths. In this chapter, we will focus on applying the chip-based microresonator frequency combs as light source, particularly for optical coherence tomography.

### **5.1.2 Optical Coherence Tomography Principle**

Optical coherence tomography (OCT) is a non-invasive imaging modality that provides depth-resolved, high-resolution images of tissue microstructures in real-time [68]. OCT enables imaging depths up to two millimeters in biological tissue with high spatial resolution. It can provide cross sectional and three

dimensional images of bio-tissue. These features have made OCT a powerful imaging technique for many medical fields such as ophthalmology, cardiology and dermatology. Time-domain (TD) OCT, spectral-domain (SD) OCT and swept-source (SS) OCT are the three widely used OCT imaging systems. Spectral-domain and the newer technology known as swept-source OCT are variations of Fourier-domain OCT, in which the interference patterns undergo a process known as Fourier transformation, which allows simultaneous measurement of all light echoes. SD-OCT is preferable over TD-OCT because it allows for high-speed OCT imaging with similar image quality due to its sensitivity advantages [69]. Although at longer imaging range, SD-OCT has sensitivity roll-off effect, it still has superior phase stability and able to provide higher resolution compared with SS-OCT. So In this dissertation, we will focus on SD-OCT. The basic configuration of SD-OCT system is shown in Figure 5.3.

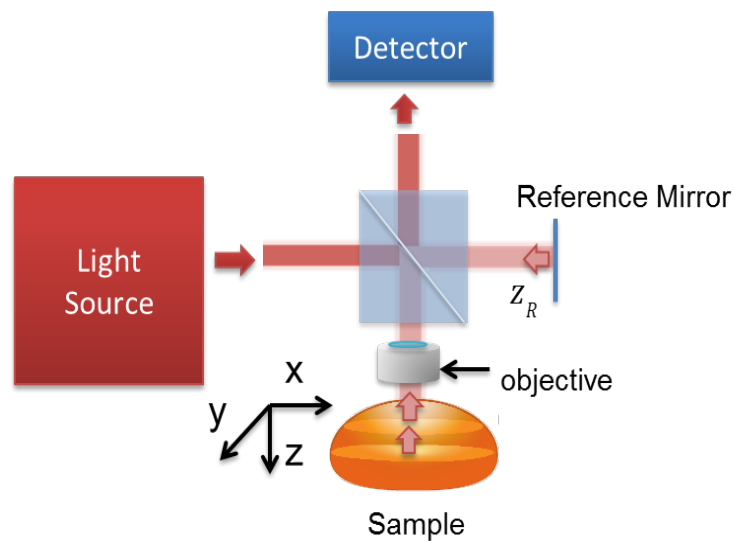


Figure 5.3: **SD-OCT configuration.** The light from the source is sent into a beam splitter, then split for the two OCT interferometer arms(reference arm and sample arm). In the sample arm, the beam reflects off a fast scanning mirror and is sent to the sample for imaging. The back-scattered light is collected and sent to the OCT spectrometer for image generation.

SD-OCT system consists of an interferometer (typically Michelson interferometer) and a broadband light source. It is based on the interferometry of the sample arm and the reference arm beam. The light coming out of the source is split by a beam splitter into two paths called the reference and sample arms. The light from reference arm is reflected back and combined with the back scatter light from the sample at the detector and we can get the interference images.

## 5.2 OCT Light Source Limitation

The performances of OCT, such as resolution, system sensitivity, light penetration, and speed, have a significant impact on medical imaging. Among all of these, axial resolution is a key factor contributing to imaging performance. The axial resolution in air is given as [70,71]:

$$\Delta z = \frac{2 \ln 2 \lambda_0^2}{\pi \Delta \lambda} \quad (5.2)$$

where  $\lambda_0$  is the central wavelength and  $\Delta \lambda$  is the full width at half-maximum (FWHM) bandwidth of the light source. As a result, light source is a crucial component in OCT systems. Superluminescent diodes (SLDs), widely used in OCT, with a central wavelength of 1300 nm have typical spectral bandwidths of up to 100 nm, corresponding to an axial resolution of 7.7  $\mu$ m (in air). SLDs with a central wavelength of 800 nm in principle can provide higher resolution, but they have limited signal penetration depth due to Rayleigh scattering and absorption in the biological tissue. Conventional SLDs suffer from the trade-off between the bandwidth and output power, mainly due to the limited gain bandwidth of the optical amplifier medium. While multiplexed SLDs mediate the tradeoff, the irregular shaped spectrum may arouse side lobes in the coherence function

and thus reduce the image contrast. A supercontinuum source could also be used to achieve high resolution OCT, but its generation relies on pulsed lasers with kW-range peak power [72], which limits its feasibility in a clinical setting. Moreover, as a result of the complex interplay of various nonlinear processes including dispersive wave generation, stimulated Raman scattering, self-phase modulation, four-wave mixing (FWM) [9, 73], supercontinuum sources suffer from high intensity noise that may deteriorate OCT imaging performance.

In addition, great efforts have been spent on the development of on-chip OCT components in order to enable OCT systems with small footprint and cost recently. These efforts have leveraged recent advances in photonic integration on-chip including the beam splitter, reference arm, sampling arm and spectrometer [74–77]. However, the degree of miniaturization of the OCT system based on the miniaturization of these components is limited, since these systems still rely on an external, tabletop light sources that cannot be easily integrated with current photonics on a silicon platform.

## **5.3 Chip-Based Frequency Comb Sources**

### **5.3.1 Device Design and Comb Generation**

We introduce a platform for a miniaturized OCT source based on chip-scale lithographically-defined microresonators. These microresonators are fabricated using traditional microelectronic processes. When optically pumped with a single continuous-wave laser source they can generate broadband frequency combs, consisting of discrete lines with a frequency spacing determined by the

geometry of the resonator. The parametric gain in these photonic structures enables ultra-broad optical bandwidths (up to an octave [78,79]) in contrast to traditional gain materials and is not limited by the gain bandwidth trade-off.

Our platform is enabled by the ultra low-loss  $\text{Si}_3\text{N}_4$  fabrication process described in Chapter 4. This resonator platform when integrated with semiconductor amplifiers, has recently been shown to enable highly efficient broadband frequency comb generation on-chip [80]. Figure 5.4 shows an artists view of a chip-scale OCT system consisting of lithographically defined components all on a single chip, where the  $\text{Si}_3\text{N}_4$  microresonator acts as a light source. Figure 5.4 inset shows the recently demonstrated hybrid approach for achieving chip-scale mm-size electrically pumped microresonator combs [80].

In order to enable a large imaging range using the optical comb as an OCT source of at least 2 mm (comparable with commercial OCT imaging range), we design the combs with a small spectral line spacing of 0.21 nm (corresponding to 38 GHz) using a large microresonator with a perimeter of 1.9 mm. This perimeter is at least an order of magnitude larger than traditional high confinement micro-resonators [81–83]. OCT imaging range is normally determined by the wavelength sampling interval of the spectrometer. However, since the frequency combs are challenging to achieve small line spacing, the imaging range, as a result of matching sampling interval and comb line spacing, is limited by free spectral range (FSR) of the frequency combs. For example, 1 THz resonator has an image range of 76  $\mu\text{m}$ . As comparison, 38 GHz resonator has an image range of more than 2 mm.

As the cavity length increase, it is challenging to achieve sufficient optical power build up and enable comb generation in such a large cavity (Equation

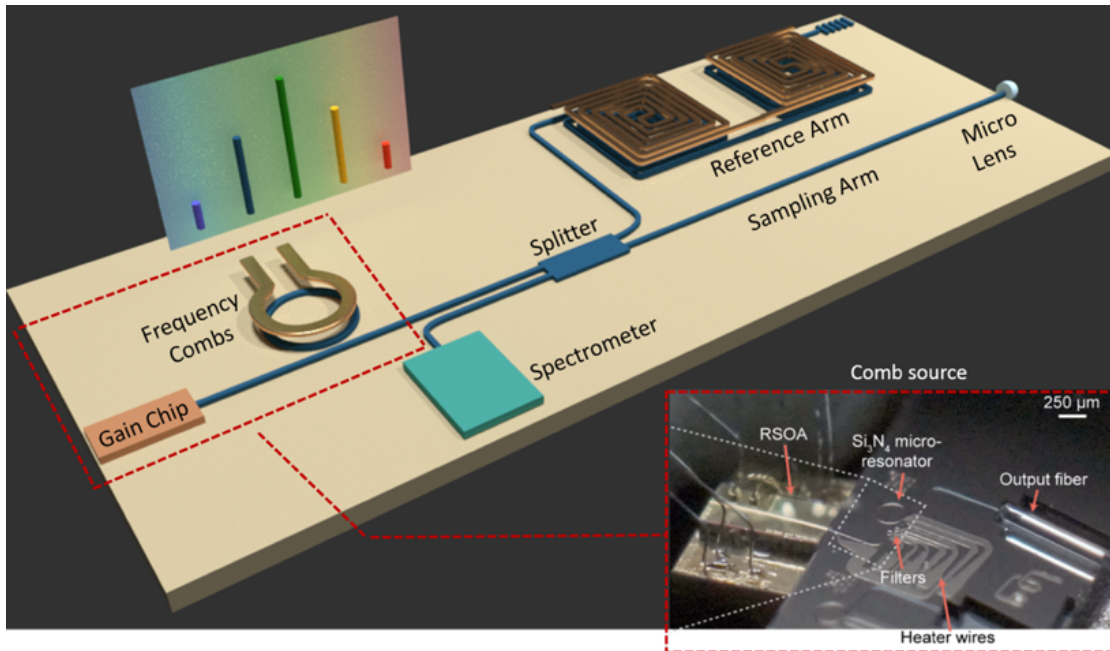


Figure 5.4: **Artist view of a fully integrated OCT systems with frequency combs light source.** The frequency combs light source is formed by a reflective semiconductor optical amplifier chip fully integrated with an ultra low-loss  $\text{Si}_3\text{N}_4$  microresonator (Inset). The interferometer, including beam splitter, reference arm, sampling arm and spectrometer is integrated on the same chip. A microlens and MEMS based scanning mirror can be attached to emit and collect and backscattered light from the sample.

3.20). We rely on ultra low-loss  $\text{Si}_3\text{N}_4$  fabrication process to compensate for the large mode volume and enables frequency combs generation with 120 nm bandwidth. In order to generate the combs with broad bandwidth and high conversion efficiency, ideal for OCT imaging, we ensure that the combs generation process does not induce soliton states with characteristic hyperbolic secant spectrum, by tuning of the cavity resonance relative to the pump frequency using a microheater co-fabricated with the resonator [84–86]. Figure 5.5a shows the fabricated on-chip resonator. Figure 5.5b shows the generated frequency

comb spectra using a ring resonator based on waveguides with  $730 \times 1500$  nm cross section. The measured power in these frequency combs lines is 42 mW with pump power of 142 mW corresponding to 30% conversion efficiency.

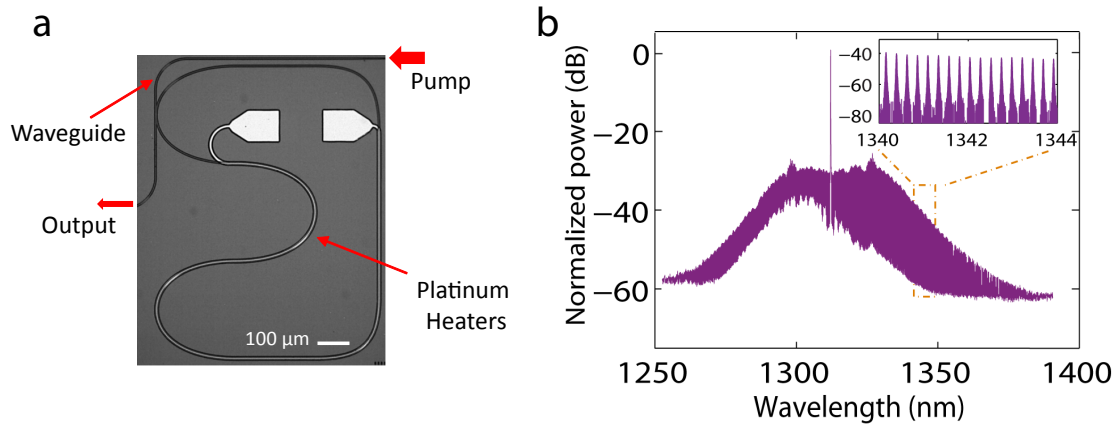


Figure 5.5: **Device image and measured spectrum.** a) Microscopy image of the silicon nitride on-chip microresonator. A platinum heater is fabricated over a large portion of the cavity and allows electric contact via the pads. b) Measured frequency comb spectrum generated using the silicon nitride microresonators. Inset shows line spacing of 0.21 nm.

### 5.3.2 Experimental Setup

Figure 5.6 shows the experimental setup for comb generation and pump filtering. A distributed feedback laser (DFB) is amplified and coupled to the  $\text{Si}_3\text{N}_4$  micro-chip. The amplifier is used to compensate coupling loss from the setup. A grating is used to filter out the pump laser before the comb is sent to the OCT system. This filtering setup can be replaced by a customized fiber-based filter to miniaturize the size of the setup in the future.

Figure 5.7 shows the schematic of the comb-based OCT setup. Note that we

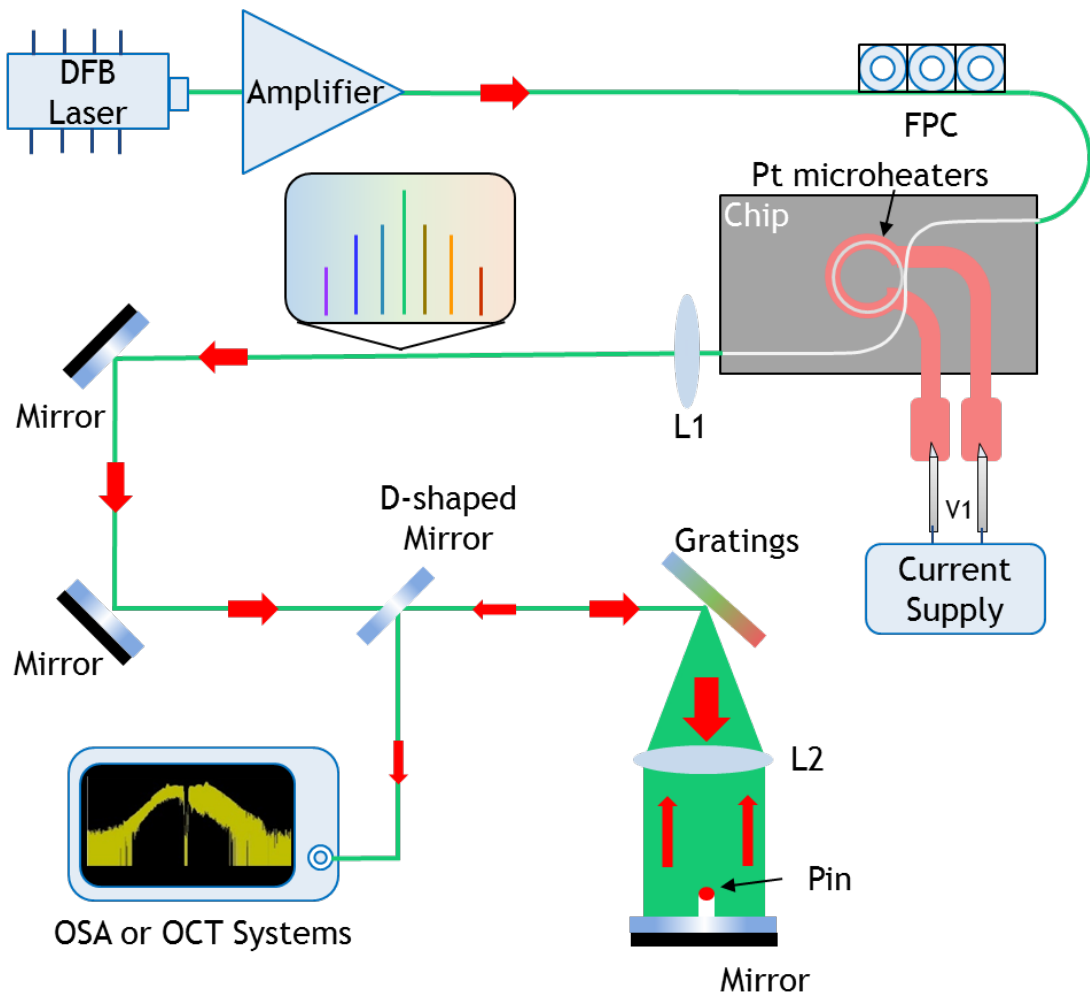


Figure 5.6: **Experimental setup for comb generation and pump filtering.** A DFB laser is amplified and coupled to the  $\text{Si}_3\text{N}_4$  micro-chip. On-chip heater allows thermal control of the cavity to ensure comb generation with low coherence. A grating is used to filter out the pump laser before the comb is sent to the OCT system.

directly plugged the comb source into the commercial system (Thorlabs Telesto I) to acquire images. The optical circulator is added to protect the commercial console. It shows that our platform is compatible with a standard commercial SD-OCT system.

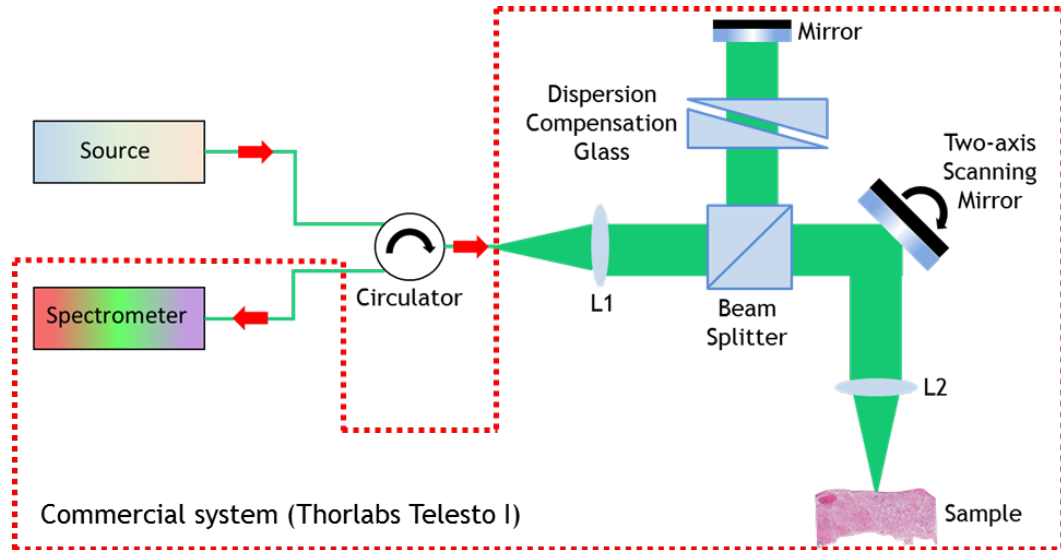


Figure 5.7: **Schematic of the comb-based OCT setup.** The fiber coupled light source is sent into a circulator, from which the beam is first collimated in free space and then split for the two OCT interferometer arms. The reference arm includes glass prisms to control dispersion. In the sample arm the beam reflects off a fast scanning mirror and is sent to the sample for imaging. The back-scattered light is collected and sent to the OCT spectrometer for image generation.

### 5.3.3 OCT Images Acquisition

Using the microresonator platform, we acquire OCT images of human tissue with chip-based frequency combs and show that the platform is compatible with a standard commercial SD-OCT system [87]. These images were achieved using a standard SD-OCT system (Thorlabs Telesto I), where the SLD was sim-

ply replaced by the chip-based frequency combs. Since the system is not optimized for our combs, the imaging capability is a lower bound limit. Figure 5.8, Figure 5.11 and Figure 5.12 show ex vivo OCT images of human breast and coronary artery samples imaged with our microresonator frequency comb source using a commercial SD-OCT system [87].

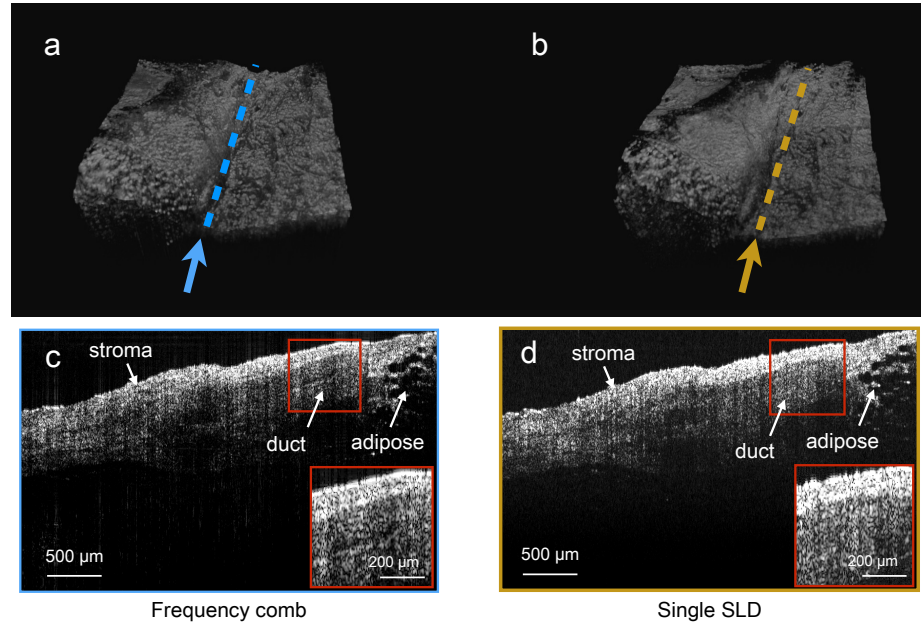


Figure 5.8: **OCT images comparison.** OCT C-scans of human breast tissue taken with a) the frequency comb source, b) a single SLD source, and OCT B-scans of the same tissue taken with c) the frequency comb source (marked by the blue arrow) and d) a single SLD source (marked by the yellow arrow), respectively. Different features and tissue types, such as stromal tissue, adipose tissue and milk duct, are delineated in both B-scans.

The human breast tissue was obtained from Columbia University Tissue Bank [88], and the human heart was obtained via the national disease research interchange [89]. Figure 5.8 compares images recorded using our microresonator frequency comb and a commercial SLD which has similar performance to the generated combs (Figure 5.9).

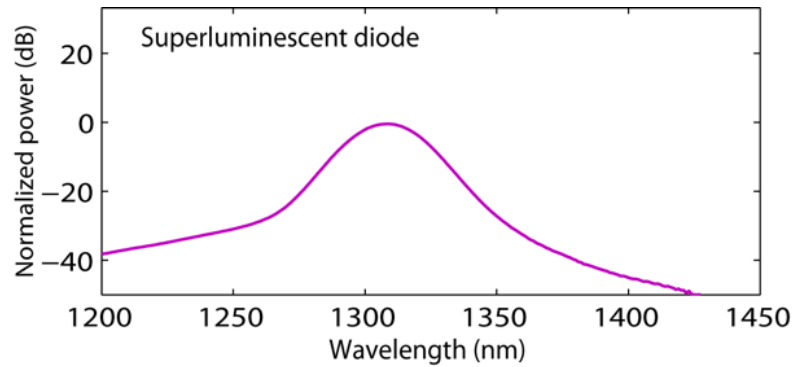


Figure 5.9: **Measured SLD spectrum.** Superluminescent diode spectrum measured with optical spectrum analyzer.

The Hematoxylin and Eosin (H&E) stained histology is provided as the reference for both the breast (Figure 5.10) and two arteries in cardiovascular system, coronary artery and aorta.

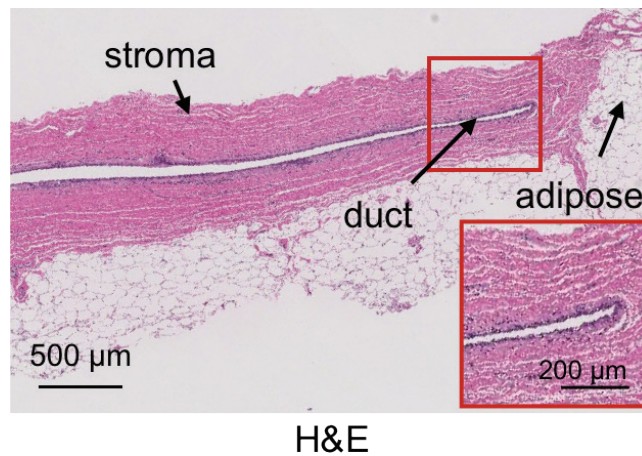


Figure 5.10: **The Hematoxylin and Eosin (H&E) stained histology of the human breast tissue.**

Different tissue types, including stromal tissue, adipose tissue and milk duct are delineated in both B-scans by comparing with the corresponding histology analysis. Figure 5.11a shows a stitched frequency-comb-based OCT image of a human left anterior descending artery (LAD) in comparison with the H&E histology in Figure 5.11b.

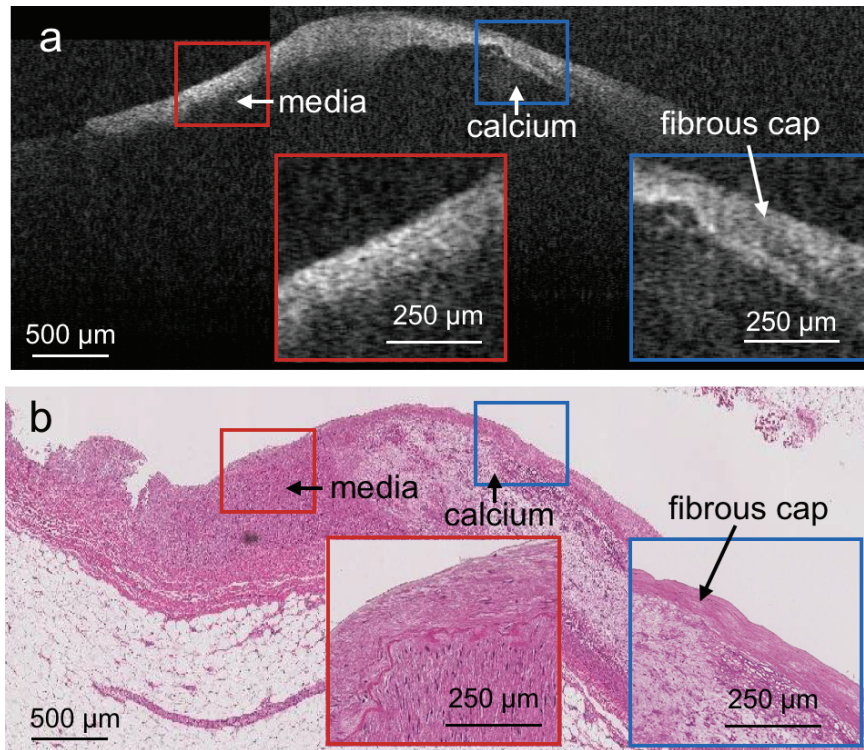


Figure 5.11: **Frequency-comb-based OCT image of human coronary artery.** a) Stitched frequency-comb-based OCT B-scans of human coronary artery with corresponding b) H&E histology of coronary artery. Note that critical features are observed, including delineation of the fibrous cap, calcium, and layered structure of intima and media are depicted within OCT images.

Figure 5.12a shows a stitched frequency-comb-based OCT image of a human aorta in comparison with the H&E histology in Figure 5.12b. OCT B-scans were stitched using the method previously used in cervical imaging [87]. In the red inset, a gradually decreasing trend of backscattering can be visualized within the transition region from a fibrous region to the media. The blue inset in Figure 5.11 reveals a typical pattern of a fibrocalcific plaque [75], where a layer of signal-rich fibrous cap is on the top of calcium, a signal-poor region with a sharply delineated border. Importantly, overlying the fibrocalcific plaque

region, we can see a transition from dense fibrous cap a region with a thinner fibrous cap for unstable plaque structure. The green inset in Figure 5.12 shows the visualization of large calcification region, the deposit of calcium. These figures show the potential to visualize critical features within human breast and cardiovascular samples by integrating the chip-based frequency combs into an OCT system.

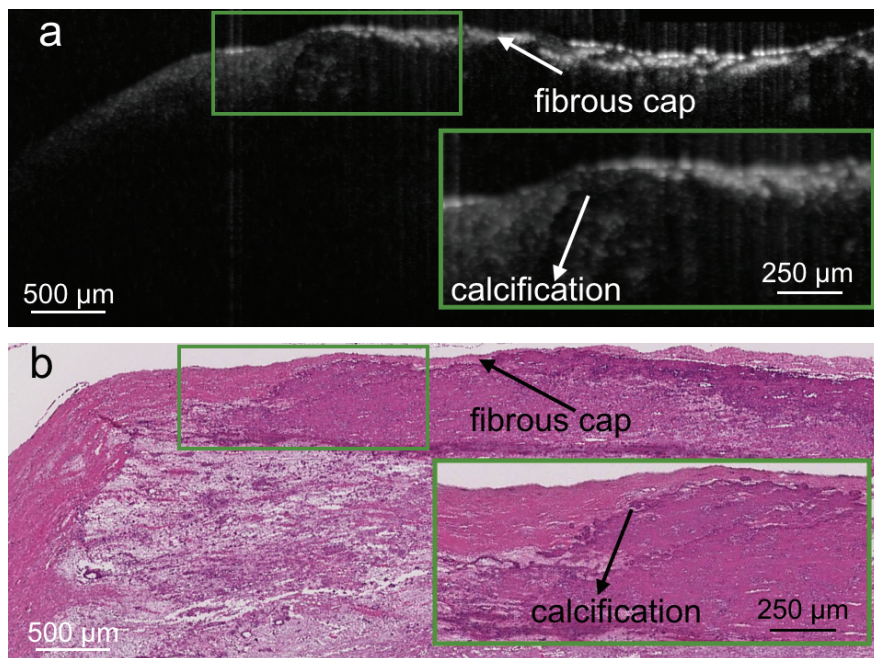


Figure 5.12: **Frequency-comb-based OCT image of human aorta.** a) Stitched frequency-comb-based OCT B-scans of human aorta with corresponding b) H&E histology of aorta. Note that the visualization of large calcification region, the deposit of calcium.

Using the frequency combs combined with the commercialized SD-OCT system, we are able to acquire OCT images. The images are reconstructed in real-time from the raw spectral data generated by the system, following standard OCT signal processing steps, including background subtraction, linear-k interpolation, apodization, and dispersion compensation. The acquisition rate is 28

kHz currently limited by the CCD line rate. The total acquisition time of an image for the SLD and the chip comb images is the same (35 msec). The sensitivity of the OCT system is defined by the minimal sample reflectivity at which the signal to noise ratio reaches unity [90]. It is measured to be 100 dB at an A-line rate of 28 kHz for the frequency comb source. The sensitivity can be further increased by suppressing the noise due to the laser-chip coupling via packaging [91]. We have shown a typical interferogram of the comb source obtained after background subtraction and spectral shaping in Figure 5.13a, where the interferogram is free of spurious features. Figure 5.13b shows the A-line signals extracted from OCT B-scan images of a mirror surface taken with the comb source. From the figures, one can see that the discrete nature of combs does not deteriorate the OCT images quality.

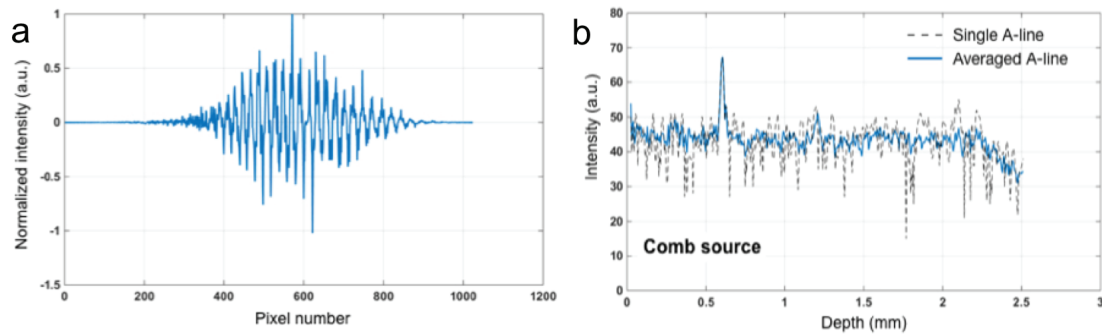


Figure 5.13: **Interferogram and noise measurement** a) A typical interferogram of the comb source obtained after background subtraction and spectral shaping. b) A-line profiles of a mirror surface measured with comb source. Single A lines are shown in gray and A lines obtained by 10× averaging (corresponding to a total of 357  $\mu$ s acquisition time in current setting) are shown in blue.

## 5.4 Summary and Discussion

We have demonstrated the chip-based frequency comb platform as light sources for OCT systems for the first time. This is a key step toward fully integrated chip-scale OCT systems. The platform has the potential to be cost-effective. In order to generate these frequency combs, we use a pump source based on a low-cost distributed feedback (DFB) laser in contrast to the high power and high stability wavelength-tunable sources usually required for generating phase-locked frequency combs. The integration of such laser with our microresonator platform could enable inexpensive sources for OCT and allow for miniaturization of OCT systems. In addition to enabling highly integrated sources,  $\text{Si}_3\text{N}_4$  microresonator combs exhibit a bandwidth that is determined by the waveguide geometry alone and not limited by the optical power [92,93], in contrast to traditional OCT sources based on SLD sources with limited bandwidth at high optical powers due to gain narrowing. The axial resolution measured with frequency comb source is  $18 \mu\text{m}$  (in air) using axial point spread function which is in good agreement with the theoretical axial resolution of  $16.3 \mu\text{m}$  using Equation 4.2. The measured axial resolution using a commercial SLD with similar performance is  $24 \mu\text{m}$  (in air). Although the axial resolution we achieved with frequency comb source is not as good as state-of-art SLD, with waveguide dispersion engineering and a spectrometer designed for the combs, this platform could enable high axial resolution and high penetration depth.

## CHAPTER 6

### ON-CHIP TUNABLE DELAY LINE

#### 6.1 Introduction

On-chip tunable photonic delay lines are one of the key building blocks for realizing optical systems-on-chip [94, 95]. Photonic delay lines can be used for many applications such as optical communication [96], microwave signal processing [97, 98], optical gyroscopes [99], and optical coherence tomography [75]. Different approaches such as photonic crystals [100, 101], Bragg gratings [102], stimulated Brillouin scattering [103, 104], and resonators [105–108] have been used to provide delay. However, these devices are based on resonant which have limited delay capacities [31, 94]. On the other hand, devices based on physically delay have been demonstrated with boarder bandwidth and longer delay [95, 109]. However, none of these devices are not tunable, they can only provide a fixed delay. In addition, they all rely on large devices with bending radius more than a millimeter. The bending losses increase almost exponentially when the bending radius reduces to sub-millimeter region. As a result, achieving tunable long delay lines with low propagation loss and board bandwidth within a small footprint remains challenging.

#### 6.2 Device Design

Here we demonstrate an on-chip tunable photonic delay line using ultra low-loss high confinement waveguides with integrated mircoheaters. Schematic of

the designed device is shown in Figure 6.1a.

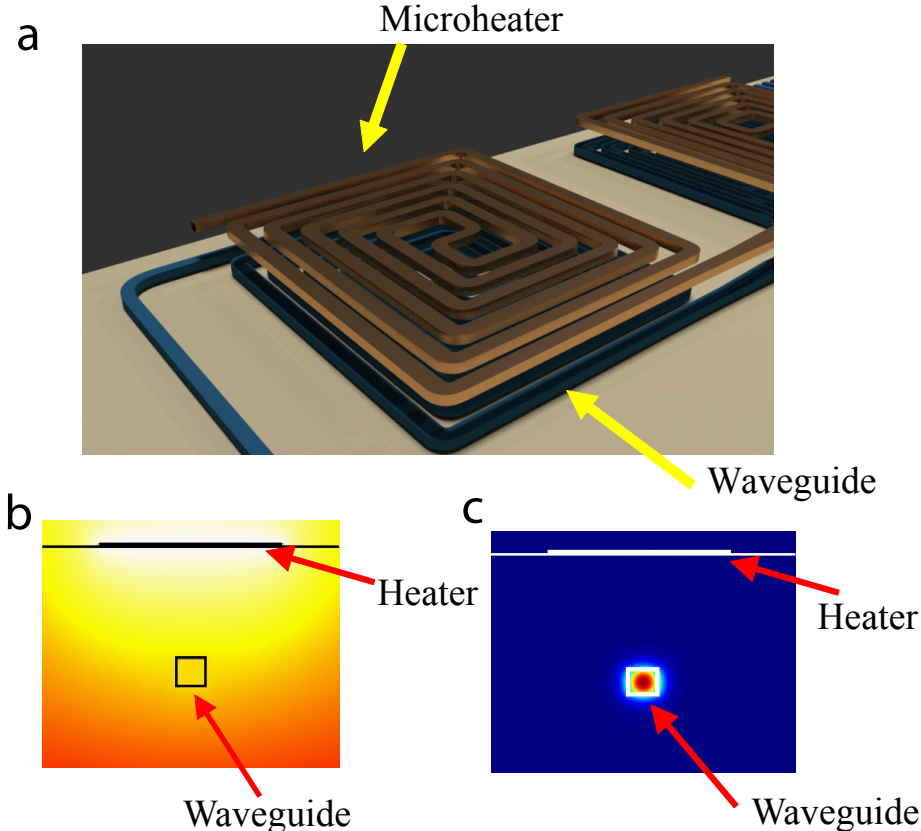


Figure 6.1: **Schematic of devices and simulation** a) Heat dissipation profile simulation for the integrated microheater. b) Schematic of on-chip photonic delay line crossing different field boundaries (shown as a dashed red line). Inset shows the mode simulation in the high confinement waveguide. One can see that the optical mode remains unaffected by the heater.

In order to enable tunability, we utilize the thermo-optic effect of  $\text{Si}_3\text{N}_4$  and design the waveguides to ensure high thermal overlap with the optical mode using microheater while ensuring minimum losses from the metal. We show the heat distribution profile simulation for the integrated microheater in Figure 6.1b, one can see that the heat from the heaters can still effectively change the temperature of the waveguide. We show the mode simulation in Figure 6.1c, one can see that the optical mode is not effected by the heater which will ensure

minimum losses. Thermo-optic effect is the change in refractive index with response to temperature. As a result, it provides optical path length change due to the index change. The relative change in the optical path length of a  $\text{Si}_3\text{N}_4$  waveguide,  $\Delta L_{opt}$ , after a temperature tuning of  $\Delta T$ , can be calculated as

$$\Delta L_{opt} = \varepsilon \cdot \Delta T \cdot l_0 \quad (6.1)$$

where  $\varepsilon = 2.45 \pm 0.09 \times 10^{-5}$  RIU/ °C [110] is the thermo-optic coefficient of  $\text{Si}_3\text{N}_4$  and  $l_0$  is the length of the  $\text{Si}_3\text{N}_4$  waveguide.

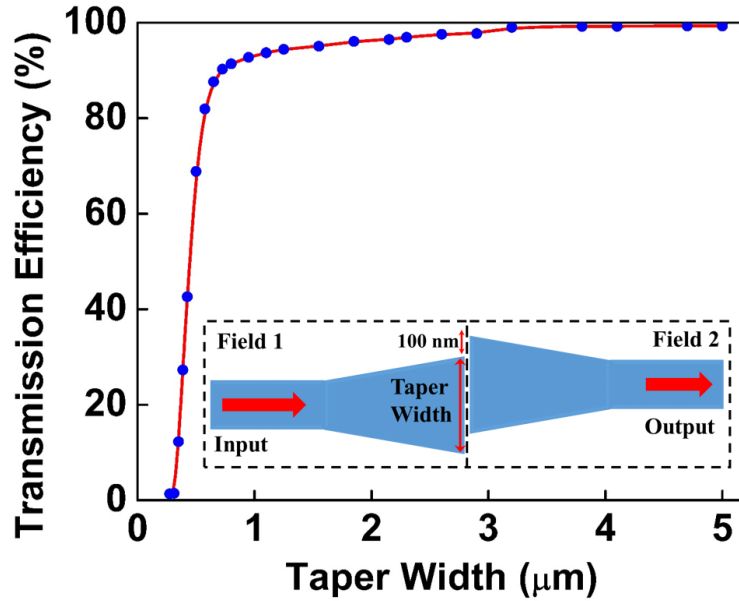


Figure 6.2: **Transmission efficiency simulation.** Simulation results of transmission efficiency with different taper widths, inset shows the schematic of adiabatically tapering at the field boundaries to reduce the propagation loss caused by misalignment.

We design the waveguides to be fundamentally robust to misalignments between different lithography fields in order to achieve low optical loss of tens of centimeter delay line with an area of several millimeter square. This robustness to misalignment is crucial since misalignments at the field boundary would dramatically increase propagation loss in the waveguide due to field shifts and

stage instability. This is not only related to mask-free lithography such as E-beam lithography, but also relevant to lithography which required masks such as deep ultraviolet lithography, since most of the high end masks are written using E-beam lithography. We use an adiabatic design to taper the size of the waveguide to a wider width at the lithographic field boundaries to increase robustness to misalignment shown in the inset of Figure 6.2. We show simulations of the light transmission efficiency with different taper widths for a misalignment of a hundred-nanometers in Figure 6.2. We choose a  $5\ \mu\text{m}$  adiabatic taper width to ensure that transmission is not effected by the misalignment.

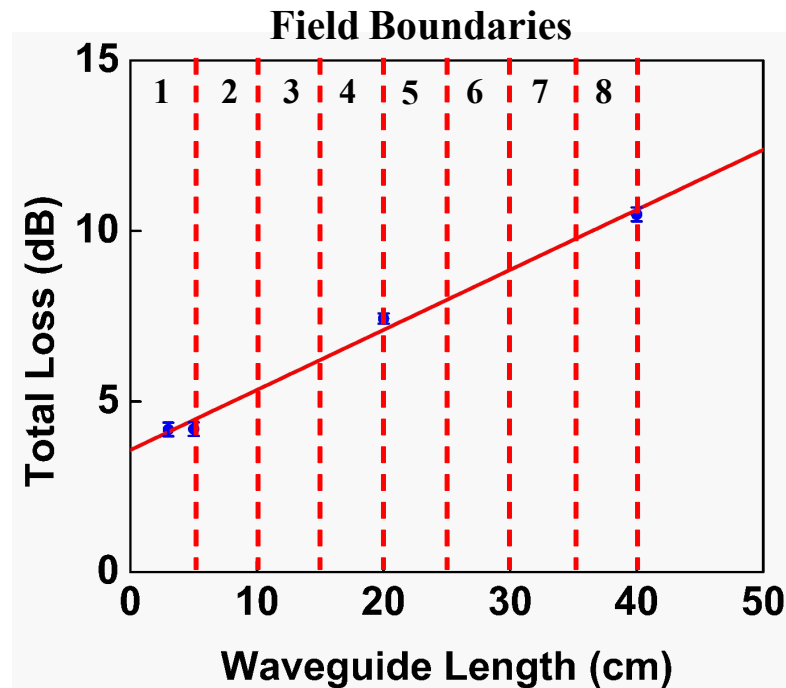


Figure 6.3: **Propagation loss measurements.** Propagation loss of waveguides which cross different fields still maintain linear fit (Note that in our case each field is 5 cm long. With a total distance of 40 cm, we cross 8 field boundaries.). It proves there is no additional loss due to misalignment in the field boundaries.

In order to confirm that our novel adiabatic taper design helps reduce the stitching loss, we measured the propagation loss of waveguides across different

number of fields (see Figure 6.3). One can see that the propagation loss has a linear dependence with the waveguide length, which indicates that there is no additional loss due to the misalignment. We do not have resonator structures in these waveguide, so we can not use the Q measurement method to measure the propagation loss. As we have different lengths of waveguides, we use the cut-back method which we describe in section 4.5 to measure the propagation loss. The propagation loss is as low as  $0.17 \pm 0.01$  dB/cm. The propagation loss can be further reduced by applying CMP and multipass lithography processes described in section 4.4.2 and 4.4.3.

### 6.3 Experimental Setup

Optical coherence tomography (OCT) is an example of a technique that can significantly benefit from such an on-chip tunable delay line. OCT is an interferometric imaging technique capable of providing high-resolution, cross-sectional and three-dimensional images with micrometer-scale axial resolution at high speed [68]. Recently, great efforts have been made towards integrating and miniaturizing OCT components, including beam splitter [74], reference arm [75], and sample arm [77] for miniature and inexpensive OCT systems printed on a wafer scale. However, the demonstrated components, to date have been passive. It is necessary to tune the path length difference to achieve high contrast images for samples with high surface topology. This is due to the fact these high contrast OCT signals rely on zero-order interference, where the interferogram features lowest possible spatial frequencies and its visibility can be maximized under quantized detection [111]. It is possible to shift the OCT image from the low signal-to-noise ratio (SNR) region to the high SNR region

using image processing. But this is a sophisticated method with limited mobility of up to  $66 \mu\text{m}$  [112]. We illustrate the capability of the photonic delay line to compensate the path length difference with a small footprint by replace the reference arm in an OCT system with this photonic delay line.

In order to illustrate the capability of the photonic delay line, we replace the reference arm in an optical coherence tomography system with the photonic delay line and show the ability to compensate the path length difference in the measurement arm within a small footprint. The total length of the waveguide is 0.4 m with a platinum microheater integrated on top of the waveguides and the total chip size is  $8 \text{ mm}^2$ , as shown in Figure 6.4. Note that the smallest bending radius here is as small as  $80 \mu\text{m}$ .

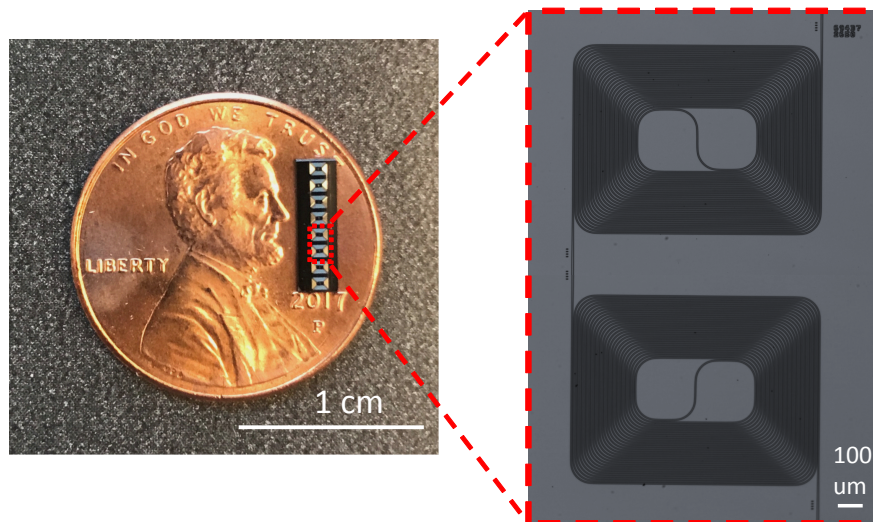


Figure 6.4: **Fabricated device with a microheater integrated on top.** A fabricated 0.4 m long high confinement  $\text{Si}_3\text{N}_4$  waveguide. These waveguides can be made tens of centimeters long with losses as low as  $0.17 \pm 0.01 \text{ dB/cm}$  with an integrated platinum heater on top of the waveguide.

We use a commercial spectral-domain (SD) OCT system (Thorlabs Telesto I) at 1325 nm to generate OCT images with the on-chip tunable delay line. Figure

6.5 shows schematic of the experimental setup to test the tunable photonic delay line. A broadband fiber coupler with 75:25 splitting ratio is used to divide the input power into the sample and reference arm. We add two circulators in the reference arm to create a single path via the on-chip tunable delay line to reduce the insertion loss of the  $\text{Si}_3\text{N}_4$  chip. We tune and monitor the temperature of the platinum heater by applying a current to the heater and measuring the resistance. In the sample arm, a low-NA objective (NA = 0.014) is used to ensure a long depth of focus ( $\sim 6$  mm in air) that is necessary for high-topology imaging. In addition, an optical delay line is inserted into the sample arm to match the fiber length differences in the two arms. Polarization controllers (PCs) are used to optimize the OCT image quality. We acquire the OCT raw data with the commercial software and the dispersion mismatch between the two arms can be fully compensated numerically during post processing. The cross-sectional OCT images as well as three-dimensional volumes are reconstructed by following standard OCT data processing steps, including background subtraction, linear-k interpolation, dispersion compensation, and apodization in MATLAB.

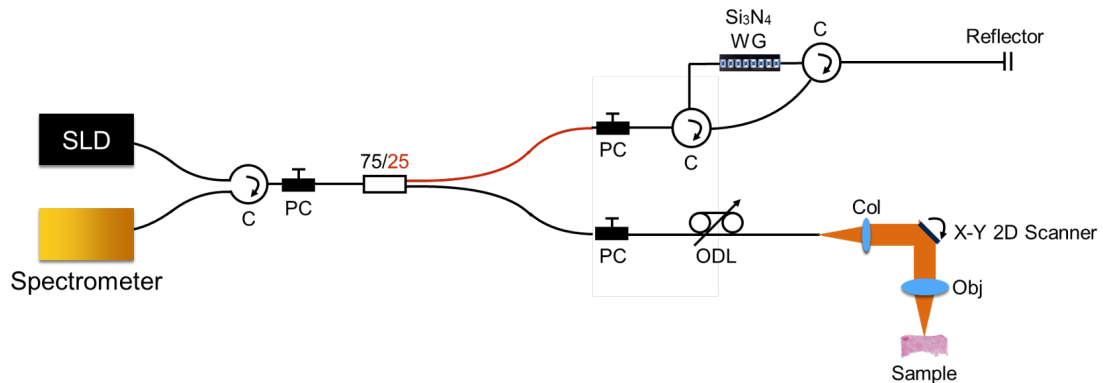


Figure 6.5: **Schematic of the experimental setup.** Schematic of the experimental setup for testing the tunable photonic delay line. C: circulator, PC: polarization controller, ODL: optical delay line, Col: collimation lens, WG: waveguide.

## 6.4 Experimental Results

In order to illustrate the capability of the photonic delay line, we start with a 5 cm long waveguide first. Onion sample is the commonly used samples in OCT. We did cross-sectional image of an onion. The OCT B-scans of onion sample are taken with and without our chip (Figure 6.6). One can see that contrast and resolution do not change which demonstrate the principle that our chip does not distortion the image.

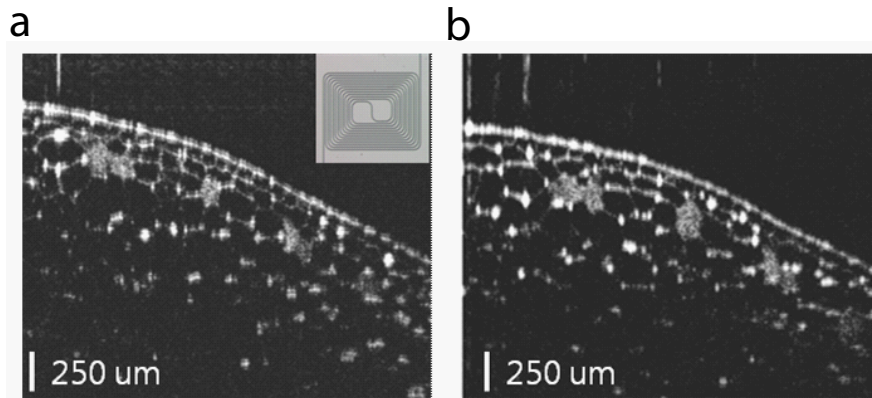


Figure 6.6: **OCT images comparison.** a) OCT B-scans of onion sample taken with fiber only without our chip. b) OCT B-scans of onion skin sample taken with our chip.

Moreover, we used the microheater to tune the effective length of the reference arm which corresponding to the  $z$  change in the image. We moved 280  $\mu\text{m}$  without any mechanical moving parts shown in Figure 6.7. This is done by simply using the integrated microheater on top of the waveguide.

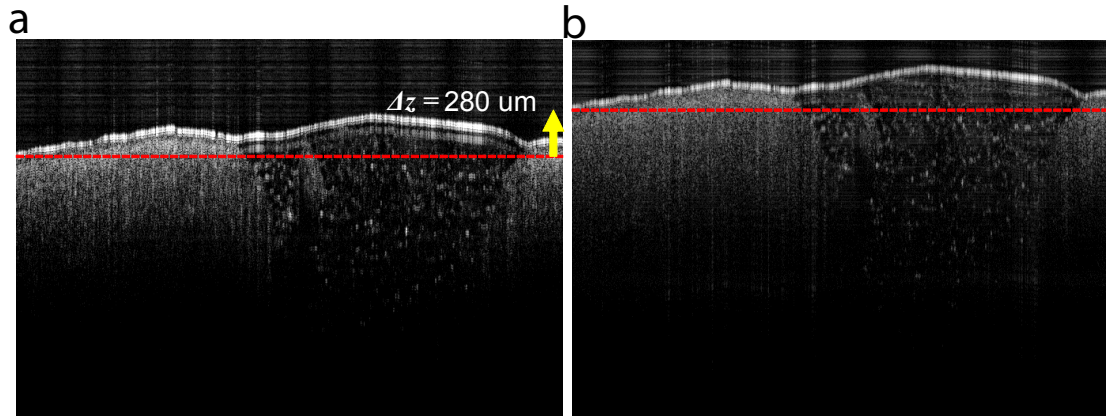


Figure 6.7: **Photonic delay line tunability test.** The microheater is used to tune the effective length of the reference arm of  $280 \mu\text{m}$ .

We then switched to 0.4 m long waveguide to show large large tunability range. We demonstrate that the tunable delay line can enhance the image contrast in the axial direction by translational shifting the images from the low SNR region to the high SNR region. The SNR of SD-OCT decreases with imaging depth due to the finite sampling area of the spectrometer pixel [113].

In Figure 6.8, we show a tissue wedge from the right ventricle of a fresh human heart before and after tuning the on-chip delay line. The OCT B-scans were taken from the endocardium side of the tissue before and after turning on the heaters. One can see that the surface at the lower part of the OCT B-scan suffers from a reduced SNR (shown in Figure 6.8a with zoom-in views shown in the red box), due to the fall-off of SD-OCT system despite the use of low-NA objective that ensure the surface remaining within the depth of focus. After turning on the heaters, we achieve and the surface area with lower profile is brought up into the high SNR regime (shown in Figure 6.8b).

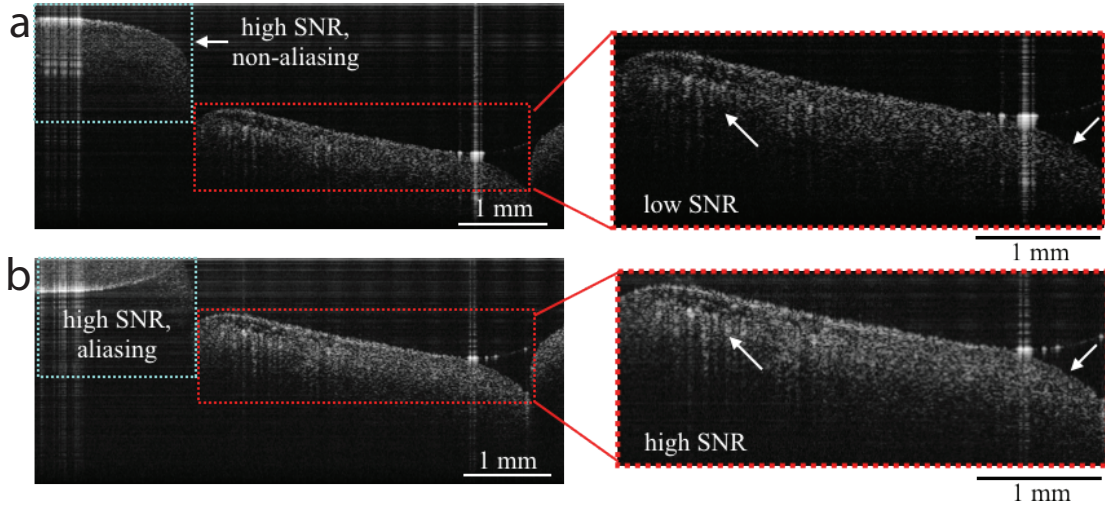


Figure 6.8: **High-topology, high-SNR OCT imaging of right ventricle sample from the endocardium side.** Two images a) and b), taken before and after turning on the heaters. Insets show the surface area is brought up to the high SNR region from low SNR region.

We show that the delay line can extend the imaging range of the OCT for a variety of applications such as blade detection, wound detection under the gauze, and structure detection of aorta. We demonstrate three examples of 3D visualization of high-topology, high-SNR imaging with the on-chip tunable delay line in Figure 6.9 using the same setup.

These images are processed using standard techniques such as multiband blending and gain compensation [87, 114]. In Figure 6.9a, we show images of a metal razor blade covered by a piece of lens tissue measured with the delay line (The experimental arrangement is illustrated by the camera image shown in the inset of Figure 6.9). One can see that only the lens tissue is resolved by the SD-OCT system before tuning the delay line and the razor blade underneath the lens tissue is clearly observed after tuning the delay line. In Figure 6.9b, we

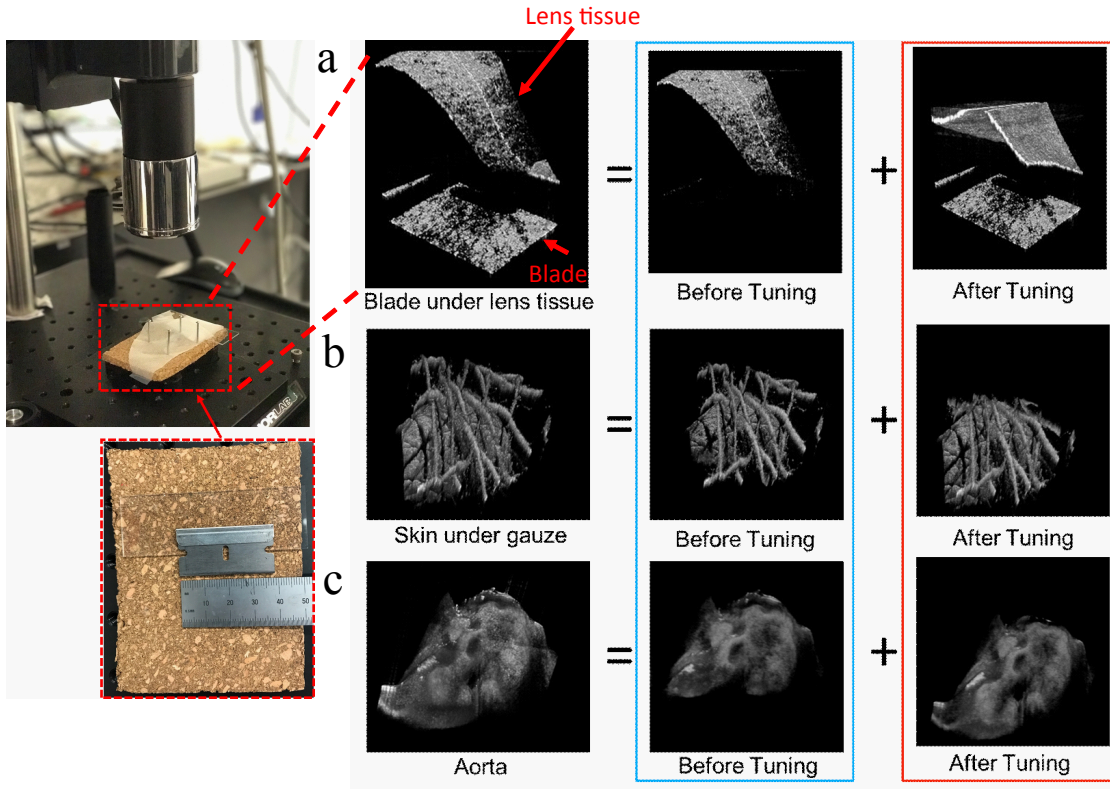


Figure 6.9: **Demonstrations of 3D high-topology, high-SNR imaging.** a) A metal razor blade is covered by the lens tissue. Inset: A camera image of the experimental arrangement. b) A skin sample is covered by the gauze. c) A human aorta sample with high surface elevation. Note that the final 3D OCT volumes are all reconstructed from stitching two volumes taken before and after tuning the delay line.

show images of a skin sample covered by a piece of gauze measured with the delay line. One can see that the gauze and top part of the tissue is resolved by the SD-OCT system before tuning the delay line and bottom part of the tissue is clearly observed after tuning the delay line. In Figure 6.9c, we show images of a human aorta sample with high surface elevation measured with the delay line. One can see that only part of the aorta is observed before tuning the delay line and the full surface topology of the aorta sample can be reconstructed after tuning the delay line.

## 6.5 Summary

We present a tunable ultra low-loss  $\text{Si}_3\text{N}_4$  on-chip tunable photonic delay line. Our on-chip tunable photonic delay line can be used to enable fully integrated OCT systems and could be beneficial for other applications such as sensing and communication as well. In order to illustrate the capability of the photonic delay line, we replace the reference arm in a commercial SD-OCT system. It empowers an on-chip reference arm with a linear translational range of 0.6 mm in the axial direction compared with the  $66 \mu\text{m}$  using sophisticated image processing methods. This on-chip tunable photonic delay line can be also used for sampling arm offers more tunability. The maximum tunable range is mainly constrained by the current heater design which can be optimized to enable an even larger tunable range. In addition, the photonic delay line also effectively extends the SD-OCT high sensitivity range as well as the imaging range. Although not demonstrated here, it should be noted that it is not only compatible with SD-OCT, but also with swept source OCT systems.

## CHAPTER 7

### FUTURE WORK

This dissertation summarized steps towards achieving ultra low-loss in high confinement  $\text{Si}_3\text{N}_4$  platform. We demonstrate optical parametric oscillation in an on-chip microresonator with record-low pump powers requirements. We have demonstrated the chip-based frequency comb platform as light sources for OCT systems for the first time. Integrated photonics is a rapidly evolving field, and several improvements to the demonstrations in the present work as well as new research directions can be identified.

#### 7.1 Higher Q

We have developed processes which drastically increased the Q by addressing the surface roughness. From our AFM measurements, one possible path for further decreasing these scattering losses is by addressing the roughness at the bottom cladding-core interface generated by the thermal oxidation process. In addition, methods such as chemical treatment and multiple annealing techniques could potentially help to further increase the Q.

In Chapter 4, we have developed the process steps such as CMP and multipass to increase the Q. We have exclusively dealt with  $\text{Si}_3\text{N}_4$  as the platform in our work. Other material platforms such as AlN, AlGaAs, Hydex, SiON, lithium niobate and even silicon can also benefit from these steps or part of the steps to achieve higher Q. As an example, multipass step has already been used in silicon platform to improve the Q [115].

## 7.2 Visible Comb and Mid-IR Combs

Due to applications demands, such as biological imaging and optical spectroscopy. Frequency combs have been pushed into visible and mid-IR regime in  $\text{Si}_3\text{N}_4$  platform.

$\text{Si}_3\text{N}_4$  has a broad transparency window covers the whole visible range even down to about 250 nm wavelength which makes it ideal for visible wavelength range. There have been several studies trying to achieve frequency combs in visible range with higher modes. However, these devices suffer from losses which limits the number of comb lines generated. In addition, a concentric or a double-layer stacked configuration could help with broadband dispersion engineering instead of local modification. With higher Q and dispersion engineering, frequency combs truly in the visible range or near visible range can be very promising.

In mid-IR wavelength range, comb generation up to  $3.5 \mu\text{m}$  has been demonstrated [67], but soliton state has not been achieved. A higher Q could alleviate the power constraint and enable transitions to soliton state. Additionally,  $\text{SiO}_2$  starts to absorb the light around  $3.7 \mu\text{m}$ , so in order to extend the wavelength to even longer regime, air clad structures need to be used.

## 7.3 Ultra High Resolution OCT

We presented the chip-based frequency comb platform as light sources for OCT systems for the first time and acquired OCT images of bio tissues in Chapter 5. The achievable resolution of the images can be greatly improved. OCT based

on these microresonator frequency combs even has the capability of achieving resolution below  $1\ \mu\text{m}$  by engineering the waveguide dimensions forming the resonator and multiplexing different combs. Waveguide dimensions can be designed to generate combs at different wavelengths using the same material platform (Combs generated around  $1600\ \text{nm}$  with FWHM of  $154\ \text{nm}$  is shown in Figure 7.3). Therefore, by multiplexing different combs, it is possible to cover visible to near-infrared wavelength window. Also, the output power of frequency combs is determined by conversion efficiency and pump power. In contrast to the traditional SLD sources which suffer from power-bandwidth trade-off, these resonators can simultaneously achieve high output power and broad bandwidth.

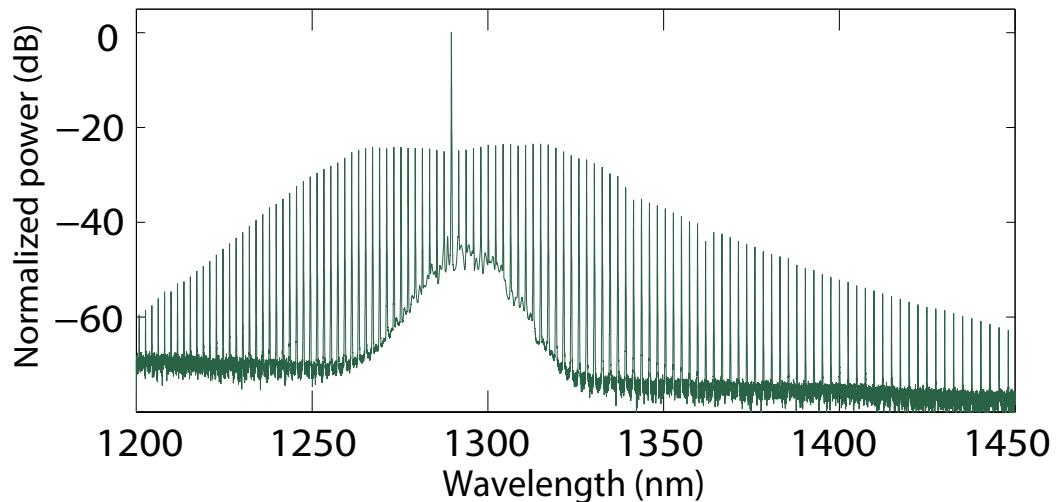


Figure 7.1: **Measured frequency comb spectrum with broader bandwidth achieved by engineering the waveguide dispersion.** Measured frequency comb spectrum generated using a designed  $\text{Si}_3\text{N}_4$  microresonator with FWHM of  $92\ \text{nm}$ . This FWHM corresponds to a predicted axial resolution of  $7.9\ \mu\text{m}$  (in air) which is comparable with the achievable resolution using a single state of art SLD.

A flat spectrum over several hundred nanometers from a single frequency comb could be also possible by higher-order waveguide dispersion engineering. We show the simulation of a flat uniform spectrum with even broader spectrum of several hundred nanometers could be generated from a single frequency comb in Figure 7.2. And a frequency comb generated with FWHM of 92 nm achieved using dispersion engineering is shown in Figure 7.3.

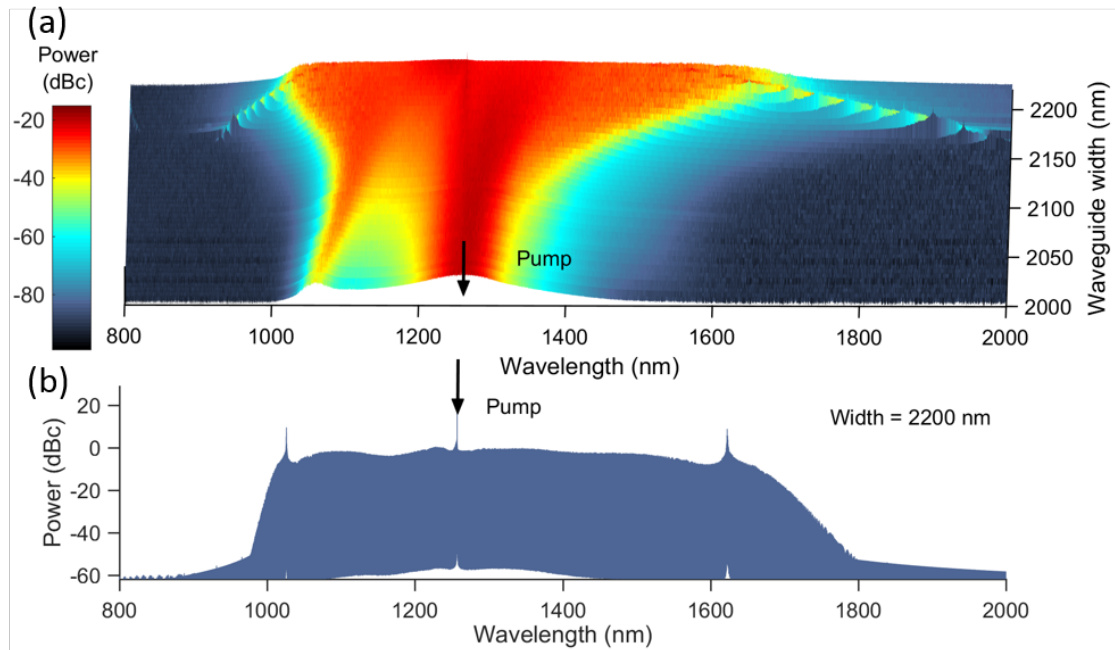


Figure 7.2: **Simulated comb spectrum with different waveguide widths.**

a) Simulated comb spectrum generated from silicon nitride microresonators based on waveguide with a fixed height (710 nm) and varying widths between 2000 nm and 2200 nm. These simulations assume a pump laser wavelength of 1258 nm. b) Simulated ultra-broad flat spectrum generated from a microresonator based on a 2200 nm waveguide width.

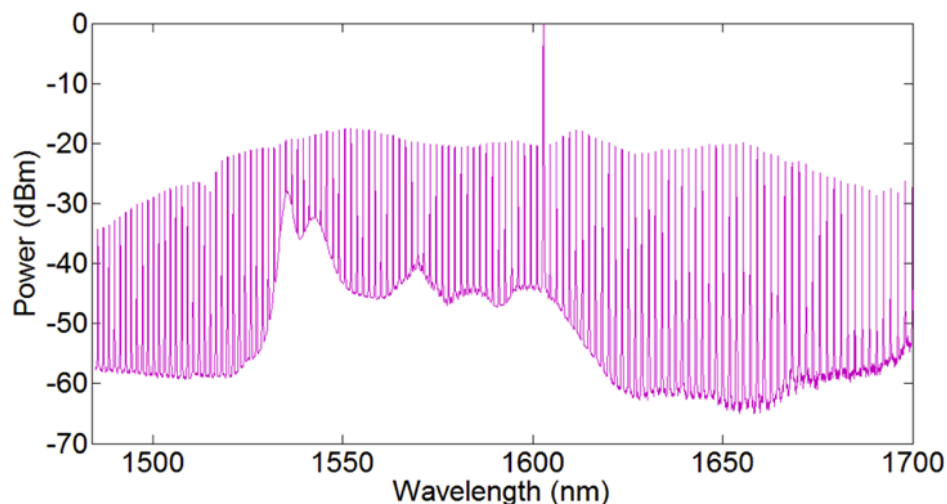


Figure 7.3: **Measured frequency comb spectrum with different wavelengths achieved by engineering the waveguide dispersion.** Measured frequency comb spectrum generated using same  $\text{Si}_3\text{N}_4$  platform centered around 1600 nm with FWHM of 154 nm (corresponding to resolution of  $7.3 \mu\text{m}$  in air).

## 7.4 Fully Integrated Systems

We have demonstrated the viability of chip-based frequency comb platform as light sources for OCT systems a key step toward fully integrated chip-scale OCT systems. As we have shown in Chapter 5, the different building blocks including a chip-scale beam splitter, reference arm (we have shown it in Chapter 6), sampling arm and spectrometer can be integrated on the same chip as the microresonator to realize a compact and low cost integrated OCT system.

With the help of ultra low-loss  $\text{Si}_3\text{N}_4$  fabrication process and sub-milliwatts nonlinear oscillation threshold, demonstrations of other systems such as fully integrated dual comb spectrometer with microfluidics channels, compact narrow linewidth laser [116] for telecommunication, low power consumption LIDAR (similar to the one demonstrated in Si [117]), and even on-chip quantum

systems can be very promising.

I believe that the work presented in this dissertation has opened up new possibilities and research directions for  $\text{Si}_3\text{N}_4$  platform. With further development of the techniques reported here, integrated photonics is poised to have a major contribution in bringing novel, compact and low cost systems to real-world applications.

## BIBLIOGRAPHY

- [1] C. Joshi, J. K. Jang, K. Luke, X. Ji, S. A. Miller, A. Klenner, Y. Okawachi, M. Lipson, and A. L. Gaeta, "Thermally controlled comb generation and soliton modelocking in microresonators," *Optics Letters* **41**, 2565 (2016).
- [2] P. A. Franken, A. E. Hill, C. W. Peters, and G. Weinreich, "Generation of Optical Harmonics," *Physical Review Letters* **7**, 118–119 (1961).
- [3] T. H. Maiman, "Optical and Microwave-Optical Experiments in Ruby," *Physical Review Letters* **4**, 564–566 (1960).
- [4] J. T. Robinson, K. Preston, O. Painter, and M. Lipson, "First-principle derivation of gain in high-index-contrast waveguides," *Optics Express* **16**, 16659 (2008).
- [5] A. Yariv, "Critical coupling and its control in optical waveguide-ring resonator systems," *IEEE Photonics Technology Letters* **14**, 483–485 (2002).
- [6] A. Yariv, "Universal relations for coupling of optical power between microresonators and dielectric waveguides," *Electronics Letters* **36**, 321 (2000).
- [7] M. A. Foster, A. C. Turner, J. E. Sharping, B. S. Schmidt, M. Lipson, and A. L. Gaeta, "Broad-band optical parametric gain on a silicon photonic chip," *Nature* **441**, 960–963 (2006).
- [8] A. C. Turner-Foster, M. A. Foster, R. Salem, A. L. Gaeta, and M. Lipson, "Frequency conversion over two-thirds of an octave in silicon nanowaveguides," *Optics Express* **18**, 1904 (2010).
- [9] Y. Okawachi, M. Yu, J. Cardenas, X. Ji, M. Lipson, and A. L. Gaeta, "Coherent, directional supercontinuum generation," *Optics Letters* **42**, 4466 (2017).
- [10] K. Luke, A. Dutt, C. B. Poitras, and M. Lipson, "Overcoming Si<sub>3</sub>N<sub>4</sub> film stress limitations for high quality factor ring resonators," *Optics Express* **21**, 22829–22833 (2013).
- [11] V. S. Ilchenko, A. A. Savchenkov, A. B. Matsko, and L. Maleki, "Nonlinear Optics and Crystalline Whispering Gallery Mode Cavities," *Physical Review Letters* **92** (2004).

- [12] H. Lee, T. Chen, J. Li, K. Y. Yang, S. Jeon, O. Painter, and K. J. Vahala, "Chemically etched ultrahigh-Q wedge-resonator on a silicon chip," *Nature Photonics* **6**, 369–373 (2012).
- [13] I. S. Grudinin, V. S. Ilchenko, and L. Maleki, "Ultrahigh optical Q factors of crystalline resonators in the linear regime," *Physical Review A* **74** (2006).
- [14] D. K. Armani, T. J. Kippenberg, S. M. Spillane, and K. J. Vahala, "Ultrahigh-Q toroid microcavity on a chip," *Nature* **421**, 925–928 (2003).
- [15] J. Hofer, A. Schliesser, and T. J. Kippenberg, "Cavity optomechanics with ultrahigh-Q crystalline microresonators," *Physical Review A* **82** (2010).
- [16] D. T. Spencer, J. F. Bauters, M. J. R. Heck, and J. E. Bowers, "Integrated waveguide coupled Si<sub>3</sub>N<sub>4</sub> resonators in the ultrahigh-Q regime," *Optica* **1**, 153 (2014).
- [17] M. J. Shaw, J. Guo, G. A. Vawter, S. Habermehl, and C. T. Sullivan, "Fabrication techniques for low-loss silicon nitride waveguides," in "Proc.SPIE," , vol. 5720, E. G. Johnson, G. P. Nordin, and T. J. Suleski, eds. (Proc.SPIE, San Jose, CA, 2005), vol. 5720.
- [18] N. Zen, T. A. Puurtinen, T. J. Isotalo, S. Chaudhuri, and I. J. Maasilta, "Engineering thermal conductance using a two-dimensional phononic crystal," *Nature Communications* **5** (2014).
- [19] Y. Liu, Y. Xuan, X. Xue, P.-H. Wang, S. Chen, A. J. Metcalf, J. Wang, D. E. Leaird, M. Qi, and A. M. Weiner, "Investigation of mode coupling in normal-dispersion silicon nitride microresonators for Kerr frequency comb generation," *Optica* **1**, 137 (2014).
- [20] J. W. Coburn and H. F. Winters, "Plasma etching A discussion of mechanisms," *Journal of Vacuum Science and Technology* **16**, 391–403 (1979).
- [21] R. Putri, P. Brault, O. Vatel, D. Henry, E. Andr, P. Dumas, and F. Salvan, "Silicon roughness induced by plasma etching," *Journal of Applied Physics* **75**, 7498–7506 (1994).
- [22] K. K. Lee, D. R. Lim, H.-C. Luan, A. Agarwal, J. Foresi, and L. C. Kimerling, "Effect of size and roughness on light transmission in a Si/SiO<sub>2</sub> waveguide: Experiments and model," *Applied Physics Letters* **77**, 1617 (2000).

- [23] M. Schaepkens, T. E. F. M. Standaert, N. R. Rueger, P. G. M. Sebel, G. S. Oehrlein, and J. M. Cook, "Study of the SiO<sub>2</sub>-to-Si<sub>3</sub>N<sub>4</sub> etch selectivity mechanism in inductively coupled fluorocarbon plasmas and a comparison with the SiO<sub>2</sub>-to-Si mechanism," *Journal of Vacuum Science & Technology A: Vacuum, Surfaces, and Films* **17**, 26 (1999).
- [24] D. Beery, K. Reinhardt, P. B. Smith, J. Kelley, and A. Sivasothy, "Post etch residue removal: novel dry clean technology using densified fluid cleaning (DFC)," in "Interconnect Technology, 1999. IEEE International Conference," (IEEE, 1999), pp. 140–142.
- [25] M. G. Blain, T. L. Meisenheimer, and J. E. Stevens, "Role of nitrogen in the downstream etching of silicon nitride," *Journal of Vacuum Science & Technology A: Vacuum, Surfaces, and Films* **14**, 2151–2157 (1996).
- [26] Y. Wang and L. Luo, "Ultrahigh-selectivity silicon nitride etch process using an inductively coupled plasma source," *Journal of Vacuum Science & Technology A: Vacuum, Surfaces, and Films* **16**, 1582–1587 (1998).
- [27] A. Gondarenko, J. S. Levy, and M. Lipson, "High confinement micron-scale silicon nitride high Q ring resonator," *Optics Express* **17**, 11366 (2009).
- [28] M. Shearn, K. Diest, X. Sun, A. Zadok, H. Atwater, A. Yariv, and A. Scherer, "Advanced silicon processing for active planar photonic devices," *Journal of Vacuum Science & Technology B: Microelectronics and Nanometer Structures* **27**, 3180 (2009).
- [29] S. P. Roberts, X. Ji, J. Cardenas, A. Bryant, and M. Lipson, "Sidewall Roughness in Si<sub>3</sub>N<sub>4</sub> Waveguides Directly Measured by Atomic Force Microscopy," in "Conference on Lasers and Electro-Optics," (OSA, San Jose, California, 2017), p. SM3K.6.
- [30] B. E. Little and S. T. Chu, "Estimating surface-roughness loss and output coupling in microdisk resonators," *Optics letters* **21**, 1390–1392 (1996).
- [31] F. Xia, L. Sekaric, and Y. Vlasov, "Ultracompact optical buffers on a silicon chip," *Nature Photonics* **1**, 65–71 (2007).
- [32] T. Tsuchizawa, K. Yamada, H. Fukuda, T. Watanabe, J.-i. Takahashi, M. Takahashi, T. Shoji, E. Tamechika, S. Itabashi, and H. Morita, "Microphotonic devices based on silicon microfabrication technology," *IEEE Journal of Selected Topics in Quantum Electronics* **11**, 232–240 (2005).

- [33] G. W. Reynolds and J. W. Taylor, "Factors contributing to sidewall roughness in a positive-tone, chemically amplified resist exposed by x-ray lithography," *Journal of Vacuum Science & Technology B: Microelectronics and Nanometer Structures* **17**, 334 (1999).
- [34] R. J. Bojko, J. Li, L. He, T. Baehr-Jones, M. Hochberg, and Y. Aida, "Electron beam lithography writing strategies for low loss, high confinement silicon optical waveguides," *Journal of Vacuum Science & Technology B: Microelectronics and Nanometer Structures* **29**, 06F309 (2011).
- [35] D. M. Tennant, R. Fullowan, H. Takemura, M. Isobe, and Y. Nakagawa, "Evaluation of a 100 kV thermal field emission electron-beam nanolithography system," *Journal of Vacuum Science & Technology B: Microelectronics and Nanometer Structures* **18**, 3089 (2000).
- [36] P. Rabiei, W. Steier, Cheng Zhang, and L. Dalton, "Polymer micro-ring filters and modulators," *Journal of Lightwave Technology* **20**, 1968–1975 (2002).
- [37] X. Yi, Y.-F. Xiao, Y.-C. Liu, B.-B. Li, Y.-L. Chen, Y. Li, and Q. Gong, "Multiple-Rayleigh-scatterer-induced mode splitting in a high- $Q$  whispering-gallery-mode microresonator," *Physical Review A* **83** (2011).
- [38] M. L. Gorodetsky, A. D. Pryamikov, and V. S. Ilchenko, "Rayleigh scattering in high- $Q$  microspheres," *JOSA B* **17**, 1051–1057 (2000).
- [39] D. S. Weiss, V. Sandoghdar, J. Hare, V. Lefevre-Seguin, J.-M. Raimond, and S. Haroche, "Splitting of high- $Q$  Mie modes induced by light backscattering in silica microspheres," *Optics letters* **20**, 1835–1837 (1995).
- [40] A. O'Keefe and D. A. G. Deacon, "Cavity ringdown optical spectrometer for absorption measurements using pulsed laser sources," *Review of Scientific Instruments* **59**, 2544–2551 (1988).
- [41] D. Romanini, A. Kachanov, N. Sadeghi, and F. Stoeckel, "CW cavity ring down spectroscopy," *Chemical Physics Letters* **264**, 316–322 (1997).
- [42] I. S. Grudinin, N. Yu, and L. Maleki, "Generation of optical frequency combs with a CaF<sub>2</sub> resonator," *Optics letters* **34**, 878–880 (2009).
- [43] T. Barwicz and H. Haus, "Three-dimensional analysis of scattering losses

- due to sidewall roughness in microphotonic waveguides," *Journal of Lightwave Technology* **23**, 2719–2732 (2005).
- [44] F. P. Payne and J. P. R. Lacey, "A theoretical analysis of scattering loss from planar optical waveguides," *Optical and Quantum Electronics* **26**, 977–986 (1994).
- [45] J. F. Bauters, M. J. R. Heck, D. D. John, J. S. Barton, C. M. Bruinink, A. Leinse, R. G. Heideman, D. J. Blumenthal, and J. E. Bowers, "Planar waveguides with less than 01 dB/m propagation loss fabricated with wafer bonding," *Optics Express* **19**, 24090 (2011).
- [46] M. H. P. Pfeiffer, A. Kordts, V. Brasch, M. Zervas, M. Geiselmann, J. D. Jost, and T. J. Kippenberg, "Photonic Damascene process for integrated high-Q microresonator based nonlinear photonics," *Optica* **3**, 20 (2016).
- [47] X. Ji, F. A. S. Barbosa, S. P. Roberts, A. Dutt, J. Cardenas, Y. Okawachi, A. Bryant, A. L. Gaeta, and M. Lipson, "Ultra-low-loss on-chip resonators with sub-milliwatt parametric oscillation threshold," *Optica* **4**, 619 (2017).
- [48] T. J. Kippenberg, S. M. Spillane, and K. J. Vahala, "Kerr-Nonlinearity Optical Parametric Oscillation in an Ultrahigh- Q Toroid Microcavity," *Physical Review Letters* **93** (2004).
- [49] A. B. Matsko, A. A. Savchenkov, D. Strekalov, V. S. Ilchenko, and L. Maleki, "Optical hyperparametric oscillations in a whispering-gallery-mode resonator: Threshold and phase diffusion," *Physical Review A* **71** (2005).
- [50] K. Ikeda, R. E. Saperstein, N. Alic, and Y. Fainman, "Thermal and Kerr nonlinear properties of plasma-deposited silicon nitride/ silicon dioxide waveguides," *Optics Express* **16**, 12987 (2008).
- [51] L. Razzari, D. Duchesne, M. Ferrera, R. Morandotti, S. Chu, B. E. Little, and D. J. Moss, "CMOS-compatible integrated optical hyper-parametric oscillator," *Nature Photonics* **4**, 41–45 (2010).
- [52] H. Jung and H. X. Tang, "Aluminum nitride as nonlinear optical material for on-chip frequency comb generation and frequency conversion," *Nanophotonics* **5** (2016).

- [53] M. Pu, L. Ottaviano, E. Semenova, and K. Yvind, "Efficient frequency comb generation in AlGaAs-on-insulator," *Optica* **3**, 823 (2016).
- [54] B. J. M. Hausmann, I. Bulu, V. Venkataraman, P. Deotare, and M. Lonar, "Diamond nonlinear photonics," *Nature Photonics* **8**, 369–374 (2014).
- [55] A. A. Savchenkov, A. B. Matsko, D. Strekalov, M. Mohageg, V. S. Ilchenko, and L. Maleki, "Low Threshold Optical Oscillations in a Whispering Gallery Mode C a F 2 Resonator," *Physical Review Letters* **93** (2004).
- [56] P. DelHaye, A. Schliesser, O. Arcizet, T. Wilken, R. Holzwarth, and T. J. Kippenberg, "Optical frequency comb generation from a monolithic microresonator," *Nature* **450**, 1214–1217 (2007).
- [57] S. A. Diddams, D. J. Jones, J. Ye, S. T. Cundiff, J. L. Hall, J. K. Ranka, R. S. Windeler, R. Holzwarth, T. Udem, and T. W. Hensch, "Direct link between microwave and optical frequencies with a 300 THz femtosecond laser comb," *Physical Review Letters* **84**, 5102 (2000).
- [58] T. Udem, R. Holzwarth, and T. W. Hensch, "Optical frequency metrology," *Nature* **416**, 233–237 (2002).
- [59] T. Steinmetz, T. Wilken, C. Araujo-Hauck, R. Holzwarth, T. W. Hansch, L. Pasquini, A. Manescau, S. D'Odorico, M. T. Murphy, T. Kentischer, W. Schmidt, and T. Udem, "Laser Frequency Combs for Astronomical Observations," *Science* **321**, 1335–1337 (2008).
- [60] A. Dutt, C. Joshi, X. Ji, J. Cardenas, Y. Okawachi, K. Luke, A. L. Gaeta, and M. Lipson, "On-chip dual-comb source for spectroscopy," *Science Advances* **4**, e1701858 (2018).
- [61] T. J. Kippenberg, R. Holzwarth, and S. A. Diddams, "Microresonator-based optical frequency combs," *Science* **332**, 555–559 (2011).
- [62] J. S. Levy, A. Gondarenko, M. A. Foster, A. C. Turner-Foster, A. L. Gaeta, and M. Lipson, "CMOS-compatible multiple-wavelength oscillator for on-chip optical interconnects," *Nature Photonics* **4**, 37–40 (2010).
- [63] J. Wang, Z. Yao, and A. W. Poon, "Silicon-nitride-based integrated optofluidic biochemical sensors using a coupled-resonator optical waveguide," *Frontiers in Materials* **2**, 34 (2015).

- [64] S. Miller, K. Luke, Y. Okawachi, J. Cardenas, A. L. Gaeta, and M. Lipson, "On-chip frequency comb generation at visible wavelengths via simultaneous second- and third-order optical nonlinearities," *Optics Express* **22**, 26517 (2014).
- [65] P. S. Donvalkar, F. A. S. Barbosa, X. Ji, Y. Okawachi, R. McNally, A. Farsi, A. Klenner, M. Lipson, and A. L. Gaeta, "Broadband Frequency Comb Generation in the Near-Visible using Higher-Order Modes in Silicon Nitride Microresonators," in "Conference on Lasers and Electro-Optics," (OSA, San Jose, California, 2017), p. STu4J.5.
- [66] A. G. Griffith, R. K. Lau, J. Cardenas, Y. Okawachi, A. Mohanty, R. Fain, Y. H. D. Lee, M. Yu, C. T. Phare, C. B. Poitras, A. L. Gaeta, and M. Lipson, "Silicon-chip mid-infrared frequency comb generation," *Nature Communications* **6** (2015).
- [67] K. Luke, Y. Okawachi, M. R. E. Lamont, A. L. Gaeta, and M. Lipson, "Broadband mid-infrared frequency comb generation in a Si<sub>3</sub>N<sub>4</sub> microresonator," *Optics Letters* **40**, 4823 (2015).
- [68] D. Huang, E. A. Swanson, C. P. Lin, J. S. Schuman, W. G. Stinson, W. Chang, M. R. Hee, T. Flotte, K. Gregory, C. A. Puliafito, and others, "Optical coherence tomography," *Science (New York, NY)* **254**, 1178 (1991).
- [69] J. F. d. Boer, B. Cense, B. H. Park, M. C. Pierce, G. J. Tearney, and B. E. Bouma, "Improved signal-to-noise ratio in spectral-domain compared with time-domain optical coherence tomography," *Optics Letters* **28**, 2067–2069 (2003).
- [70] A. F. Fercher, "Optical coherence tomography development, principles, applications," *Zeitschrift fr Medizinische Physik* **20**, 251–276 (2010).
- [71] S.-W. Lee, H.-W. Jeong, Y.-C. Ahn, W. Jung, Z. Chen, and B.-M. Kim, "Optimization for Axial Resolution, Depth Range, and Sensitivity of Spectral Domain Optical Coherence Tomography at 1.3  $\mu\text{m}$ ," *Journal of the Korean Physical Society* **55**, 2354–2360 (2009).
- [72] G. Genty, S. Coen, and J. M. Dudley, "Fiber supercontinuum sources (Invited)," *JOSA B* **24**, 1771–1785 (2007).
- [73] K. L. Corwin, N. R. Newbury, J. M. Dudley, S. Coen, S. A. Diddams, B. R. Washburn, K. Weber, and R. S. Windeler, "Fundamental amplitude

noise limitations to supercontinuum spectra generated in a microstructured fiber," *Applied Physics B* **77**, 269–277 (2003).

- [74] B. I. Akca, B. Povaay, A. Alex, K. Wrhoff, R. M. de Ridder, W. Drexler, and M. Pollnau, "Miniature spectrometer and beam splitter for an optical coherence tomography on a silicon chip," *Optics Express* **21**, 16648 (2013).
- [75] G. Yurtsever, B. Povaay, A. Alex, B. Zabihian, W. Drexler, and R. Baets, "Photonic integrated Mach-Zehnder interferometer with an on-chip reference arm for optical coherence tomography," *Biomedical Optics Express* **5**, 1050 (2014).
- [76] L. Chang, N. Weiss, T. G. van Leeuwen, M. Pollnau, R. M. de Ridder, K. Wrhoff, V. Subramaniam, and J. S. Kanger, "Chip based common-path optical coherence tomography system with an on-chip microlens and multi-reference suppression algorithm," *Optics Express* **24**, 12635 (2016).
- [77] S. Schneider, M. Lauermann, P.-I. Dietrich, C. Weimann, W. Freude, and C. Koos, "Optical coherence tomography system mass-producible on a silicon photonic chip," *Optics Express* **24**, 1573 (2016).
- [78] Y. Okawachi, K. Saha, J. S. Levy, Y. H. Wen, M. Lipson, and A. L. Gaeta, "Octave-spanning frequency comb generation in a silicon nitride chip," *Optics Letters* **36**, 3398–3400 (2011).
- [79] P. DelHaye, T. Herr, E. Gavartin, M. L. Gorodetsky, R. Holzwarth, and T. J. Kippenberg, "Octave Spanning Tunable Frequency Comb from a Microresonator," *Physical Review Letters* **107** (2011).
- [80] B. Stern, X. Ji, Y. Okawachi, A. L. Gaeta, and M. Lipson, "Fully integrated ultra-low power Kerr comb generation," arXiv preprint arXiv:1804.00357 (2018).
- [81] M. H. P. Pfeiffer, C. Herkommer, J. Liu, H. Guo, M. Karpov, E. Lucas, M. Zervas, and T. J. Kippenberg, "Octave-spanning dissipative Kerr soliton frequency combs in Si<sub>3</sub>N<sub>4</sub> microresonators," *Optica* **4**, 684 (2017).
- [82] M. Karpov, M. H. P. Pfeiffer, J. Liu, A. Lukashchuk, and T. J. Kippenberg, "Photonic chip-based soliton frequency combs covering the biological imaging window," *Nature Communications* **9** (2018).
- [83] P. Trocha, M. Karpov, D. Ganin, M. H. P. Pfeiffer, A. Kordts, S. Wolf,

- J. Krockenberger, P. Marin-Palomo, C. Weimann, S. Randel, W. Freude, T. J. Kippenberg, and C. Koos, "Ultrafast optical ranging using microresonator soliton frequency combs," *Science* **359**, 887–891 (2018).
- [84] T. Herr, K. Hartinger, J. Riemensberger, C. Y. Wang, E. Gavartin, R. Holzwarth, M. L. Gorodetsky, and T. J. Kippenberg, "Universal formation dynamics and noise of Kerr-frequency combs in microresonators," *Nature Photonics* **6**, 480–487 (2012).
- [85] S. Coen, H. G. Randle, T. Sylvestre, and M. Erkintalo, "Modeling of octave-spanning Kerr frequency combs using a generalized mean-field Lugiato-Lefever model," *Optics Letters* **38**, 37–39 (2013).
- [86] F. Ferdous, H. Miao, D. E. Leaird, K. Srinivasan, J. Wang, L. Chen, L. T. Varghese, and A. M. Weiner, "Spectral line-by-line pulse shaping of on-chip microresonator frequency combs," *Nature Photonics* **5**, 770–776 (2011).
- [87] Y. Gan, W. Yao, K. M. Myers, J. Y. Vink, R. J. Wapner, and C. P. Hendon, "Analyzing three-dimensional ultrastructure of human cervical tissue using optical coherence tomography," *Biomedical Optics Express* **6**, 1090–1108 (2015).
- [88] X. Yao, Y. Gan, E. Chang, H. Hibshoosh, S. Feldman, and C. Hendon, "Visualization and tissue classification of human breast cancer images using ultrahigh-resolution OCT," *Lasers in Surgery and Medicine* **49**, 258–269 (2017).
- [89] Y. Gan, D. Tsay, S. B. Amir, C. C. Marboe, and C. P. Hendon, "Automated classification of optical coherence tomography images of human atrial tissue," *Journal of Biomedical Optics* **21**, 101407–101407 (2016).
- [90] R. Leitgeb, C. K. Hitzenberger, and A. F. Fercher, "Performance of fourier domain vs. time domain optical coherence tomography," *Optics Express* **11**, 889–894 (2003).
- [91] T. Komljenovic, M. Davenport, J. Hulme, A. Y. Liu, C. T. Santis, A. Spott, S. Srinivasan, E. J. Stanton, C. Zhang, and J. E. Bowers, "Heterogeneous Silicon Photonic Integrated Circuits," *Journal of Lightwave Technology* **34**, 20–35 (2016).
- [92] H. Jung, C. Xiong, K. Y. Fong, X. Zhang, and H. X. Tang, "Optical fre-

- quency comb generation from aluminum nitride microring resonator," *Optics Letters* **38**, 2810 (2013).
- [93] X. Xue, P.-H. Wang, Y. Xuan, M. Qi, and A. M. Weiner, "Microresonator Kerr frequency combs with high conversion efficiency," *Laser & Photonics Reviews* **11**, 1600276 (2017).
- [94] X. Wang, L. Zhou, R. Li, J. Xie, L. Lu, K. Wu, and J. Chen, "Continuously tunable ultra-thin silicon waveguide optical delay line," *Optica* **4**, 507 (2017).
- [95] H. Lee, T. Chen, J. Li, O. Painter, and K. J. Vahala, "Ultra-low-loss optical delay line on a silicon chip," *Nature Communications* **3**, 867 (2012).
- [96] R. W. Boyd, D. J. Gauthier, and A. L. Gaeta, "Applications of Slow Light in Telecommunications," *Optics and Photonics News* **17**, 18–23 (2006).
- [97] A. E. Willner, B. Zhang, L. Zhang, L. Yan, and I. Fazal, "Optical Signal Processing Using Tunable Delay Elements Based on Slow Light," *IEEE Journal of Selected Topics in Quantum Electronics* **14**, 691–705 (2008).
- [98] J. Capmany, B. Ortega, and D. Pastor, "A tutorial on microwave photonic filters," *Journal of Lightwave Technology* **24**, 201–229 (2006).
- [99] C. Ciminelli, C. E. Campanella, F. Dell'Olio, M. N. Armenise, E. Armandillo, and I. McKenzie, "Study of photonic resonant angular velocity sensors as alternative gyro technology," in "Proc.SPIE," , vol. 10564, E. Armandillo, N. Karafolas, and B. Cugny, eds. (SPIE, 2017), vol. 10564, pp. 10564 – 10564 – 6.
- [100] Y. A. Vlasov, M. O'Boyle, H. F. Hamann, and S. J. McNab, "Active control of slow light on a chip with photonic crystal waveguides," *Nature* **438**, 65–69 (2005).
- [101] D. O'Brien, A. Gomez-Iglesias, M. D. Settle, A. Michaeli, M. Salib, and T. F. Krauss, "Tunable optical delay using photonic crystal heterostructure nanocavities," *Physical Review B* **76** (2007).
- [102] I. Giuntoni, D. Stolarek, D. I. Kroushkov, J. Bruns, L. Zimmermann, B. Tillack, and K. Petermann, "Continuously tunable delay line based on SOI tapered Bragg gratings," *Optics Express* **20**, 11241 (2012).

- [103] Z. Shi and R. W. Boyd, "Discretely tunable optical packet delays using channelized slow light," *Physical Review A* **79** (2009).
- [104] D. Marpaung, B. Morrison, M. Pagani, R. Pant, D.-Y. Choi, B. Luther-Davies, S. J. Madden, and B. J. Eggleton, "Low-power, chip-based stimulated Brillouin scattering microwave photonic filter with ultrahigh selectivity," *Optica* **2**, 76 (2015).
- [105] J. Cardenas, M. A. Foster, N. Sherwood-Droz, C. B. Poitras, H. L. R. Lira, B. Zhang, A. L. Gaeta, J. B. Khurgin, P. Morton, and M. Lipson, "Wide-bandwidth continuously tunable optical delay line using silicon microring resonators," *Optics Express* **18**, 26525 (2010).
- [106] F. Morichetti, A. Melloni, C. Ferrari, and M. Martinelli, "Error-free continuously-tunable delay at 10 Gbit/s in a reconfigurable on-chip delay-line," *Optics Express* **16**, 8395–8405 (2008).
- [107] N. K. Fontaine, J. Yang, Z. Pan, S. Chu, W. Chen, B. E. Little, and S. J. Ben Yoo, "Continuously Tunable Optical Buffering at 40 Gb/s for Optical Packet Switching Networks," *Journal of Lightwave Technology* **26**, 3776–3783 (2008).
- [108] C. Xiang, M. L. Davenport, J. B. Khurgin, P. A. Morton, and J. E. Bowers, "Low-Loss Continuously Tunable Optical True Time Delay Based on Si<sub>3</sub>N<sub>4</sub> Ring Resonators," *IEEE Journal of Selected Topics in Quantum Electronics* **24**, 1–9 (2018).
- [109] J. F. Bauters, M. L. Davenport, M. J. R. Heck, J. K. Doylend, A. Chen, A. W. Fang, and J. E. Bowers, "Silicon on ultra-low-loss waveguide photonic integration platform," *Optics Express* **21**, 544–555 (2013).
- [110] A. Arbabi and L. L. Goddard, "Measurements of the refractive indices and thermo-optic coefficients of Si<sub>3</sub>N<sub>4</sub> and SiO<sub>x</sub> using microring resonances," *Optics Letters* **38**, 3878 (2013).
- [111] W. Drexler and J. G. Fujimoto, eds., *Optical Coherence Tomography: Technology and Applications* (Springer International Publishing, 2015), 2nd ed.
- [112] L. Fang, S. Li, Q. Nie, J. A. Izatt, C. A. Toth, and S. Farsiu, "Sparsity based denoising of spectral domain optical coherence tomography images," *Biomedical Optics Express* **3**, 927–942 (2012).

- [113] S. H. Yun, G. J. Tearney, B. E. Bouma, B. H. Park, and J. F. d. Boer, "High-speed spectral-domain optical coherence tomography at 1.3  $\mu\text{m}$  wavelength," *Optics Express* **11**, 3598–3604 (2003).
- [114] M. Brown and D. G. Lowe, "Automatic Panoramic Image Stitching using Invariant Features," *International Journal of Computer Vision* **74**, 59–73 (2007).
- [115] S. A. Miller, M. Yu, X. Ji, A. G. Griffith, J. Cardenas, A. L. Gaeta, and M. Lipson, "Low-loss silicon platform for broadband mid-infrared photonics," *Optica* **4**, 707 (2017).
- [116] B. Stern, X. Ji, A. Dutt, and M. Lipson, "Compact narrow-linewidth integrated laser based on a low-loss silicon nitride ring resonator," *Optics Letters* **42**, 4541 (2017).
- [117] S. A. Miller, C. T. Phare, Y.-C. Chang, X. Ji, O. Jimenez, A. Mohanty, S. Roberts, M. C. Shin, B. Stern, m. zadka, and M. Lipson, "512-Element Actively Steered Silicon Phased Array for Low-Power LIDAR," in "Conference on Lasers and Electro-Optics," (OSA, San Jose, California, 2018), p. JTh5C.2.